Design of a Blast Resistant Armour Plate

AALBORG UNIVERSITET

Søren Barrett

Rasmus V.L.R. Christiansen

Ahmad Othman

M.Sc. Thesis
June 2017

Aalborg University
Department of Materials and Production

AALBORG UNIVERSITY

Department of Materials and Production
Fibigerstræde 16
DK 9220 Aalborg Øst
www.ses.aau.dk

Title:
Design of a blast resistant armour plate

Project period:
DMS4, Spring semester 2017

Project group:
1.123c

Group members:

Søren Barrett

Rasmus V. L. R. Christiansen

Ahmad Othman

Supervisors:
Jørgen Asbøll Kepler

ECTS:
30

Number of pages:
106 + (46)

Annex:
ZIP-archive

Submission date:
2016-06-02

Synopsis:

This thesis treats blast effects on a generic armour floor panel with prioritised focus on the military applications more specifically the Humvee. The purpose of this thesis is to determine the blast load from an explosive placed below the vehicle, investigate the material parameters of an aluminium foam for implementation in an armour solution, and suggest a generic armour panel maximising energy absorption for protection of the personnel in the vehicle. Initially, the case of the thesis is presented along with the thesis scope and outline. This is followed by general theory as a basis for the remainder of the thesis. The blast load, peak pressure and impulse, from a DM51 hand grenade exploding beneath a floor panel of the vehicle is determined using two different methods. Both methods are based on empirically obtained data in grand test schemes, and are therefore validated for a large variety of cases. The investigation of the energy absorbing properties of the aluminium foam shows that the available foam is highly inhomogeneous and inconvenient for design tasks requiring great tolerances. An alternative is therefore investigated using a highly modifiable structure of lattices for designs requiring great material control. However, the cost of the aluminium foam makes it highly desirable for structures covering a large area, and analytical as well as numerical models are developed for determining effective designs utilising the foam. Different design concepts are investigated, morphed and rejected until a single design is optimised for energy absorption and use in the armour floor panel of the vehicle. Finally, plans for experimental validation of both the analytical methods and the final design are described.

Preface

This thesis has been submitted to the Department of Materials and Production at Aalborg University in partial fulfilment of the requirements for the M.Sc. degree on the study; Design of Mechanical Systems. The thesis period was from the 1st of February to the 2nd of June 2017. The work has been supervised by Associate Professor, Ph.D. Jørgen Asbøll Kepler to whom we would like to extent our thanks for guidance, discussions and feedback throughout the period. Furthermore, we would like to thank the cooperating partner Composhield A/S for the project, materials, guidance and discussions and especially a thank you to the company representative Herluf Montes Schütte.

The studies have made use of the commercial softwares MATLAB and ANSYS Autodyn and ANSYS explicit dynamics. The report is typeset in LaTeX, and figures are made in MATLAB or Microsoft Visio. Furthermore, the terminal ballistics laboratory in the basement of Fibigerstræde 14, Aalborg University has been used for experiments.

Appended to the thesis is an appendix in which additional information or explanations can be found. References to theses appendices exist throughout the report, when necessary. An electronic annex containing ANSYS simulation files, MATLAB files, material tests etc. are likewise appended, and can be found in the project database.

References in the report are made using the Harvard method, meaning the authors of the reference along with the year the material is published are stated in the report as [Author, year]. Additional information on the material is listed in the bibliography sorted by the last name of the first author.

The report is intended for supervisor, censor and Composhield. The content of the report and project is non-classified, but subjected to a Non-Disclosure Agreement between the authors and Composhield.

Søren Barrett
Rasmus V.L.R. Christiansen
Ahmad Othman
Aalborg, June 2017.

Abstract

The objective of the present M.Sc thesis is to propose a design for a blast resistant armour floor panel for vehicles in military applications. The project is conducted in cooperation with Composhield A/S, a military armour manufacturer, who aim to enhance their already extensive product portfolio within lightweight protection panels supplying greater protection of their clients in theatres of operation around the world. The proposed design is an amour floor panel with specifications offering protection against a blast load from an explosive placed directly beneath the vehicle of equivalent 0,12 kg TNT at a distance of 0,5 m, i.e. the case-load. The panel does resist greater blast loads with slight modifications.

A three-way approach to the problem is taken consisting of an analytical, a numerical and an experimental approach. Only the analytical and numerical approach are finished in the following report, while the experimental approach is planned for the near future. The analytical approach is utilised for obtaining a solid understanding of the governing blast parameters and an initial guess of different design parameters. This approach is mainly academical. The actual design of the armour panel is conducted purely numerically.

One of the significant problems in the thesis is to determine or quantify the blast load acting on the floor of the vehicle originating from an exploding DM51 hand grenade of 0,12 kg TNT at a distance of 0,5 m. An extensive study of blast effects is therefore conducted in order to determine the design load on the structure acting as a load case for the remaining of the project. This is followed by a study of the material parameters of foamed aluminium in order to determine the energy absorbing properties and ultimately the applicability in armour panels. Analytical studies in determining the deformation and the optimum distribution of front panel and foam mass for maximum energy absorption are conducted. However, the manufacturing methods of aluminium foams are very difficult to control while remaining cheap resulting in a, at times, highly inhomogeneous material which is unacceptable in some applications. An alternative using a lattice structure is therefore investigated, resulting in a highly modifiable structure which can be re-engineered for specific needs.

A numerical design procedure using hydrocode is utilised in search of a capable design concept for blast loads which is the main focus of the thesis. The capable design is reached through a parametric study of multiple iterations minimising the residual load in the structure following the deformation of the armour panel.

The experimental approach has not been conducted, but a plan for near future experimental work is described in the report. This includes verification of discrepancies between the analytical and numerical approach, and a full-scale test of the armour panel for validation of the ability of the panel to withstand the specified blast threat.

Abstract

Formålet med det foreliggende speciale er at foreslå et design for en sprængningsresistent panser gulvplade for køretøjer i militære applikationer. Projektet er udført i samarbejde med Composhield A/S, en panserproducent for militære applikationer, som søger at udvide deres allerede omfattende produktkatalog indenfor letvægtsbeskyttelsespaneler til beskyttelse af deres klienter i verdensomspændende militære brændpunkter. Det foreslåede design er et panser gulvpanel med specifikationer, der tilbyder beskyttelse imod en sprængningslast fra en eksplosiv placeret direkte under køretøjet bestående af en ækvivalent TNT-vægt på 0,12 kg i en afstand af 0,5 m, m.a.o. case-lasten. Panelet modstår større sprængningslaster med få modifikationer.

En tredelt fremgangsmåde i forhold til problemet er taget, og består af en analytisk, en numerisk og en eksperimentel del. Kun den analytiske og numeriske del er færdiggjort, men den eksperimentelle del er planlagt for den nære fremtid. Den analytiske del er udført for at opnå en solid forståelse af de bestemmende sprængningsparameter og et indledende gæt på designparametrene. Denne del er hovedsagelig medtaget grundet akademiske overvejelser. Den faktiske designproces er udført rent numerisk.

Et af de signifikante problemer i specialet er at bestemme eller kvantificere sprængningslasten virkende på køretøjets gulvpanel fra en eksploderende DM51 håndgranat, hvilket producerer case-lasten. Et udførligt studie af sprængningseffekter er derfor udført for at bestemme designlasten virkende på køretøjet, som bruges igennem hele projektet. Dette er efterfulgt af et materialestudie i et tilgængeliggjort aluminiumsskum med det formål at bestemme de energiabsorberende egenskaber og ultimativt dettes anvendelighed i et panserpanel. Analytiske studier er anvendt for at bestemme deformationen i dette skum under last, og den optimale fordeling af masse i henholdsvis frontpladen og skummet for maksimal energioptag er ligeledes bestemt. Fremstillingsparametrene er dog meget krævende at kontrollere mens omkostningerne stadig holdes nede, og dette resulterer i et skum, der til tider er meget uhomogent, hvilket i en række designapplikationer er uacceptabelt. Et alternativ, der gør brug af en gitterkonstruktion, er derfor undersøgt resulterende i et design, der er yderst modificerbar til specifikke behov.

En numerisk designproces, ved hydrocodes, er anvendt i forsøget på at finde et kompetent sprængningsresistent design, hvilket også er hovedfokusset for dette speciale. Det kompetente design er fundet igennem et parameterstudie over en række iterationer med optimeringskriteriet at minimere restlasten i strukturen efter deformation af panserpanelet.

Det eksperimentelle arbejde er ikke udført, men en plan for den nære fremtid er beskrevet i rapporten. Dette inkluderer en verifikation af de observerede afvigelser imellem de analytiske og numeriske modeller samt en fuldskala test af panserpanelet for validering af hvorvidt panelet er i stand til at modstå sprængningstruslen.

Contents

1 Introduction

Dynamic events such as a detonation of an explosive create non-linear shock waves in solids in immediate vicinity, and it is therefore necessary to study, and develop methods, for predicting the effects of such an explosion, such as fracture, failure, but also energy absorption properties of these solids, [Davison, 2008].

In a historical context, the studies of non-linear wave propagation have been conducted since the late 1800s. At first, the investigations were mainly theoretical and limited to gases. In the early 1900s, experimental research of shock compression in solids slowly began and the interest in this field greatly increased during the 1940s and 1950s due to the military value of the research and the modern scientific work is based on the preliminary work of researchers in the US and the USSR, [Davison, 2008].

This thesis is conducted in collaboration with Composhield A/S, a company that develops and manufactures armour for mobile, semi-mobile and non-mobile applications. The mobile application is the focus of this project.

This means, that the following master thesis investigates the effect of an explosive on a composite armour designed for use on military personnel vehicles such as, but not limited to, the Humvee [HMMWV: High Mobility Multi-purpose Wheeled Vehicle], figure 1.1, and develops a composite armour capable of withstanding an explosion of 0,098 kg of equivalent TNT in a distance of 0,5 m. This demand great energy absorbing and impulse resistant properties of the armour, which is achievable through use of metallic foams, a specific designed 'crash'-structure fixture for the chassis to protect the vehicle structure from the energy in the blast wave and a capable and correct design of the armour panel.

Figure 1.1: *HMMWV M1165 military vehicle. Design of a composite armour for the floor is the focus of the thesis. [AM General, 2017]*

An attempt of keeping the project generic is made, as energy absorbing structures can be used in a variety of fields e.g. crash-structures in the automotive industry for civil use.

1.1 The Humvee

It is decided to use the Humvee as the case vehicle as well defined drawings and descriptions of this vehicle exists. As it is desired to obtain a somewhat generic armour configuration, it is not inconceivable that the plate can be used on the danish APCs (armoured personnel carriers) M113 as well.

The Humvee is the preferred light tactical vehicle of more than 60 nations worldwide for either military or homeland security applications. This amount to a number of 230.000 HMMWV vehicles currently operational worldwide, [AM General, 2017]. The Humvee is built on a multi-purpose platform permitting a variety of different configurations, and as the Humvee has been in production since 1983, it amounts to approximately 60 different officially recognised configurations of the platform, [Global Security, 2017].

In 2011 the US army facilitated a program to phase out the use of the HMMWV vehicle branches for a new and more modern light tactical vehicle, but the program was abandoned as the requirements and available technology of such a vehicle would simply put too much strain on the treasury. Instead, it was decided to modernise the HMMWV program by increasing the automotive performance, regain mobility, extend the service life and ***improve blast protection***. Thereby extending the service life of the HMMWV program for at least 15 years, [Global Security, 2017].

As mentioned the different configurations of the different HMMWV are based on the same platform, as shown in figure 1.2.

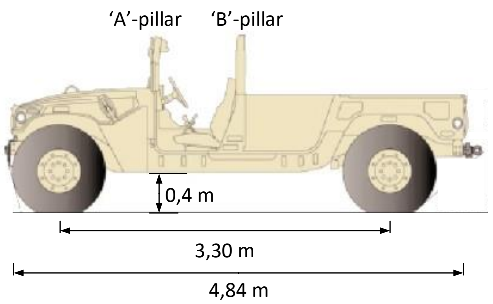

(a) The HMMWV M1165 platform. The curb weight is 2.971 kg. Two armour configurations exists, increasing the weight to 3.279 kg and 4.477 kg respectively. [Global Security, 2017].

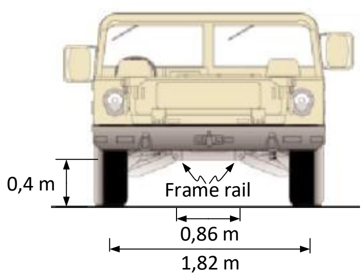

(b) Distance between frame rail, i.e. suitable mounting point for the armour panel. [Global Security, 2017].

Figure 1.2

As the Humvee operates in regions of both IEDs (Improvised Explosive Devices), RPGs (Rocket-Propelled-Grenade) and ballistics attacks from regular assault and marksman rifles, the armour panel has to be able to withstand both blast waves and ballistic impacts without major compromises. This is especially critical for the side panels of the vehicle. As mentioned earlier, the main concern of this thesis is to treat the floor of the Humvee, and in this case the vulnerability against the ballistic threats is not as great, hence the main area of study is the energy absorption of the floor.

A variety of injuries can be sustained by the vehicle personnel during and in the aftermath of an IED or mine explosion below the vehicle, as seen in figure 1.3. An excerpt of the injuries are cuts and perforation by flying debris/fragments following the impulse of the explosion or rupture of the floor or windows in the vehicle, leg injuries due to the rapid deformation of the floor and the following loading of the legs, trauma to body or head following the acceleration of the vehicle due to the kinetic energy in the impulse or soil, rocks etc., and finally external/internal burns due to the thermal effect of the explosion or ignition of combustibles in the vehicle.

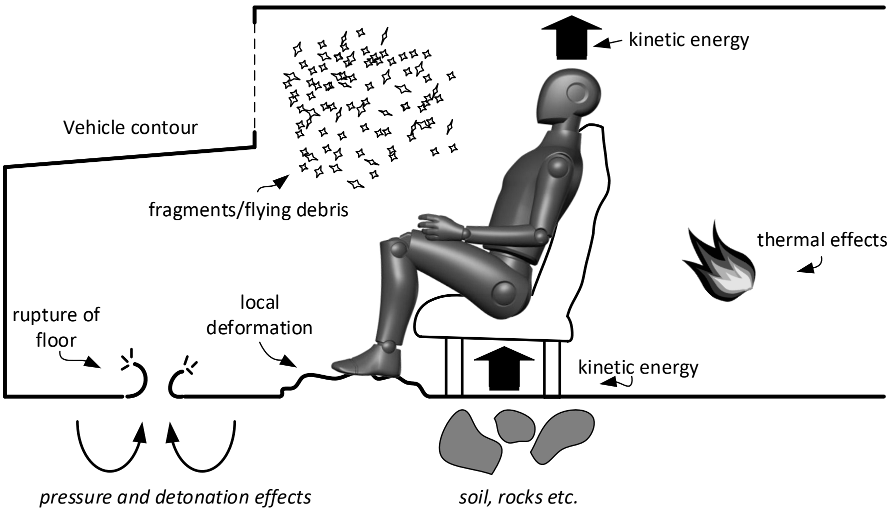

Figure 1.3: *An excerpt of the consequences of an IED or mine explosion below the Humvee. Based on Stankiewicz et al. [2015].*

1.2 Human tolerance against injuries

The human tolerance against the blast output of an explosion is relatively high [Unified Facilities Criteria, 2008]. However, the stance of a person (standing, sitting, prone, face-on or side-on), relative to the blast front, as well as the shape of the pressure front (fast or slow rise, stepped loading), are significant factors in determining the amount of injury sustained.

The threshold and severe lung-damage pressure levels for short duration load are 200 to 275 kPa and above 550 kPa, respectively, while the threshold for lethality due to lung damage is approximately 690 to 827 kPa. On the other hand, the threshold pressure level for tissue haemorrhage resulting from long-duration loads may be as low as 69 to 103 kPa, which is approximately a third of the sustainable pressure in a short duration blast. [Unified Facilities Criteria, 2008].

A hemispherical surface blast, and the resulting range vs. pressure for the case explosive (defined in sec. 2.2) in free air is shown in figure 1.4. This shows that the hand grenade generates a pressure causing serious lung damage in a radius of 1,5 m. An explosion of this case explosive directly beneath the Humvee do cause some vehicular damage, while remaining fairly safe to conduct experiments with, in case this becomes an option. If fragments are added to the grenade, the lethality range is 35 m, [Jane's Information Group, 1996]. However, fragments are not considered and used.

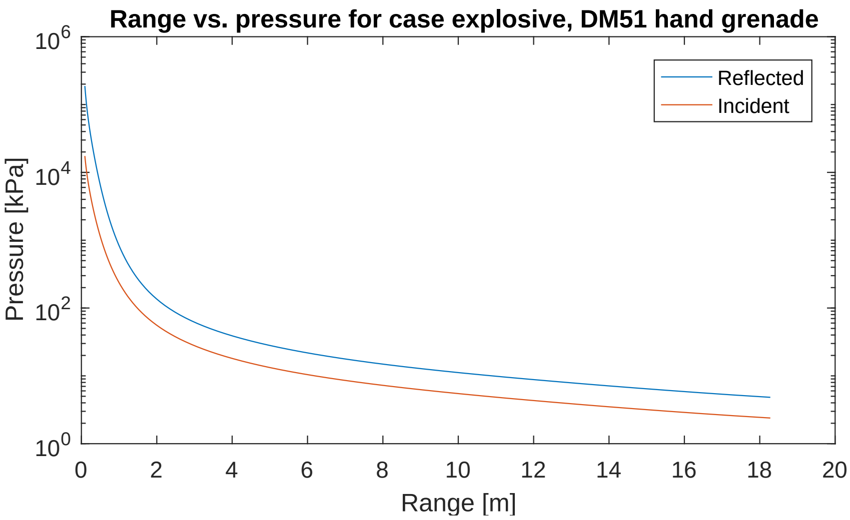

Figure 1.4: *Range vs. pressure for case explosive DM51. Lethal due to pressure in a range of 1,5 m.*

Structural motion

Besides the pressure tolerance, it is necessary to consider the human tolerance of two types of shock exposure;

- Impacts causing body acceleration/deceleration.
- Body vibration as a result of the vibratory motion of the structure.

Studies have indicated that a probable safe impact (of a head against a hard, flat surface) tolerance velocity is 3 m/s. At 5,5 m/s there is a 50 percent probability of skull fracture and, at 7 m/s, the probability is nearly 100 percent. An impact velocity of 3 m/s is considered to be generally safe for persons who are in a fairly rigid status; therefore, greater impact velocities can be tolerated if the body is in a more flexible position or if the area of impact is large. [Unified Facilities Criteria, 2008].

Fragments

Overall, human tolerance to fragment impact is very low; however, certain protection can be provided with shelter type structures. Fragments can be classified based on their size, velocity, material and source, as [Unified Facilities Criteria, 2008];

- *Primary fragments,* which are small, high-speed missiles usually formed from casing and/or material located immediately adjacent to the explosion.

- *Secondary fragments,* which are generated from the breakup of the structure or material contained within the structure.

The design must secure the human inside the vehicle from both fragment types mentioned above. However the design of the plate in this project accounts only for the blast effects where the vehicle is assumed to be already armoured against the ballistic effects of the explosion.

1.3 Structural response

The dynamic response of a structure and its elements depends on, [Unified Facilities Criteria, 2008];

1. the properties (type, weight, shape, casing, etc.) and location of the explosive charge.
2. the sensitivity (tolerance) of the structure.
3. the physical properties and configuration of the protective structure.

The structural response is defined by the load transferred to the structure by the protective plate in which a high energy absorbing plate results in a smaller residual load transferred to the structure. A good design may direct the residual load to certain points (well supported points) which leads to a better overall response of the structure. In this project, a specific case for a set amount of explosive is studied where the design aims to provide as great a blast protection as possible.

1.3.1 Pressure design ranges

In the following, the response of the structure due to the pressure is presented. The response can be divided into design ranges, defined by the pressure intensity as, (1) high pressure, and (2) low pressure which defines whether the loading is impulsive or dynamic. For a definition of the blast parameters and use of these, see chapter 2 and chapter 4.

High-Pressure design range

At the high-pressure design range, the initial pressures acting on the protective structure are extremely high and furthermore amplified by their reflections on the structure. Also the durations of the applied loads are short, particularly in cases where complete venting of the explosion products are possible, [Unified Facilities Criteria, 2008]. These durations are also short in comparison to the response time (time to reach maximum deflection) of the individual elements of the structure, i.e the positive phase is short compared with the natural period. In this case the load has finished acting before the structure has had time to respond significantly where most deformation occurs at times greater than t_0, see figure 1.5.

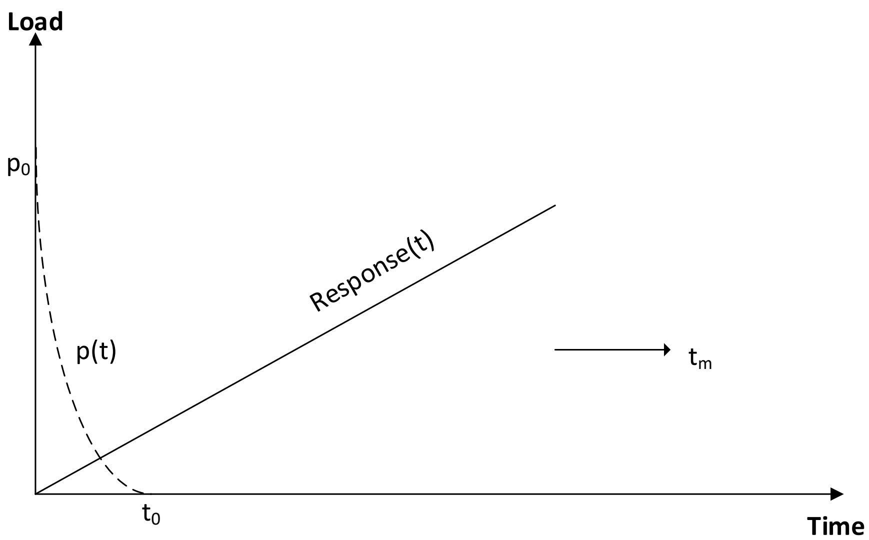

Figure 1.5: *Impulsive loading: response time compared with load duration. The response is assumed linear with respect to time which is not the real case as seen subsequently. [Smith and Hetherington, 1994].*

The graph indicates that the blast load pulse has fallen to zero before any significant displacement occurs. Therefore, structures subjected to blast effects in the high-pressure range can, in certain cases, be designed for the impulse (area under the pressure-time curve) rather than the peak pressure associated with longer duration blast pressures, [Unified Facilities Criteria, 2008].

Low-Pressure design range

Structures subjected to blast pressures associated with the low-pressure range sustain peak pressures of smaller intensity than those associated with the high-pressure range. However, the duration of the load can even exceed the response time of the structure. In this case where the positive time t_0 and the time of maximum deformation t_m of the structure are approximately the same, the assessment of response in this regime is more complex, possibly requiring complete solution of the equation of motion of the structure [Smith and Hetherington, 1994]. This dynamic or pressure-time regime is represented graphically in figure 1.6.

Structural elements designed for the low-pressure range depend on both pressure and impulse, [Unified Facilities Criteria, 2008].

A very low-pressure range can be added as a third level which is related to relatively low peak pressure and large explosive charges (several hundred tons). The duration t_0 is extremely long in comparison to those of smaller explosive charges as indicated in figure 1.7. The graph indicates that the structure reached its maximum displacement before the blast load has undergone any significant decay. Such a loading is referred to as quasi-static or pressure loading.

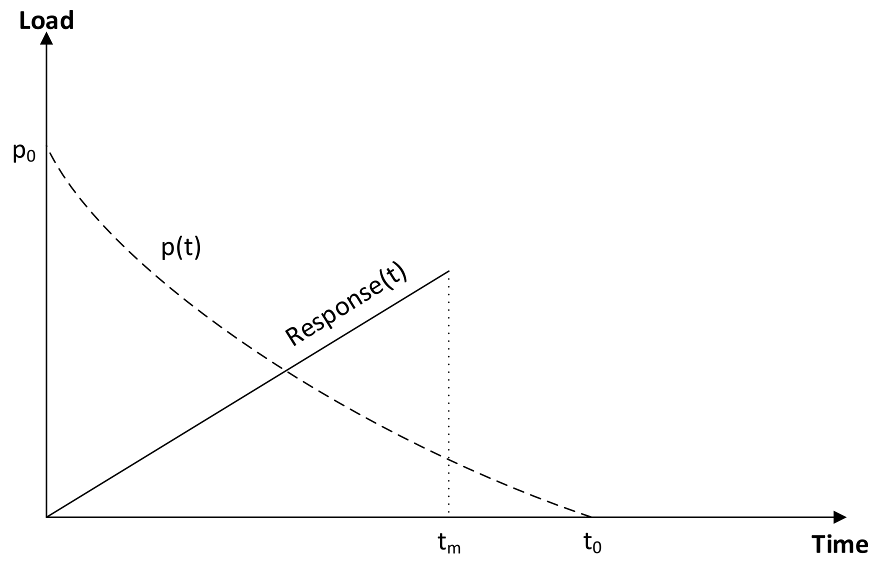

Figure 1.6: *Dynamic loading: response time compared with load duration. Again, the response is assumed linear with respect to time which is not the real case. [Smith and Hetherington, 1994].*

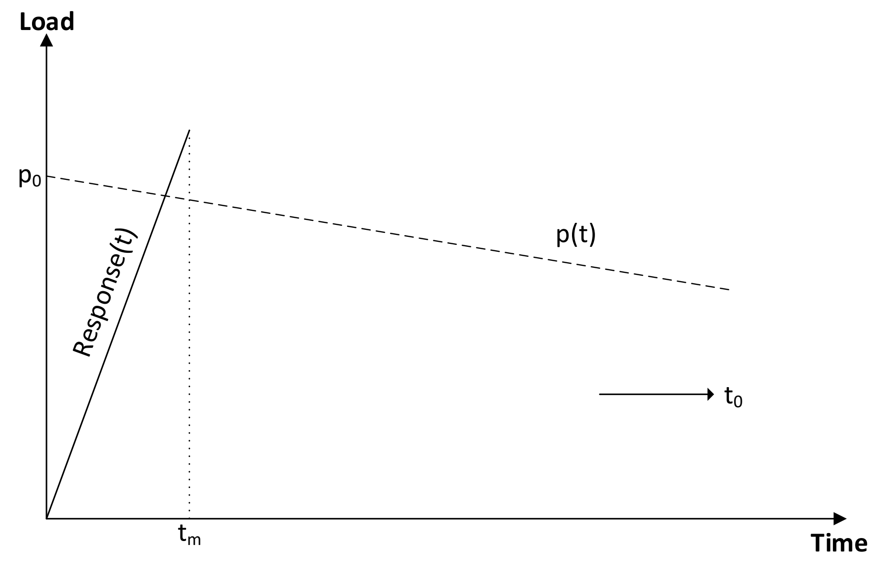

Figure 1.7: *Quasi-static loading: response time compared with load duration, modified from [Smith and Hetherington, 1994].*

1.3.2 Analysing blast environment

Although each design pressure range is distinct, no clear-cut divisions between the ranges exist; therefore, each protective structure must be analysed to determine its response. Figure 1.8 indicates semi-quantitatively the parameters which define the design ranges (including the very low range) of an element, along with the approximate relationship between the time to reach maximum deflection t_m and the load duration t_0.

It was described earlier that the design range of an element is related to the location of the element relative to the explosion, see section 2.3. For the quantity of explosives considered in this study, an element (the plate) designed for the high-pressure range which is situated immediately next-to the explosion, and its exposed surface facing the explosion is oriented normal or nearly normal to the propagation of the initial pressure wave to account for the most severe case as figure 2.5 shows. On the other hand the explosive detonates on the surface, i.e. ground, as depicted in case c in figure 2.4. This is a very common case when attacking a mobile vehicle using an explosive weapon.

The actual pressure-time relationship resulting from a pressure distribution on the element is highly irregular because of the multiple reflections from different surfaces such as the ground, rocks, other structures etc.. For these cases, the pressure-time relationship may be approximated by a fictitious right triangular pressure pulse as shown subsequently in chapter 4.

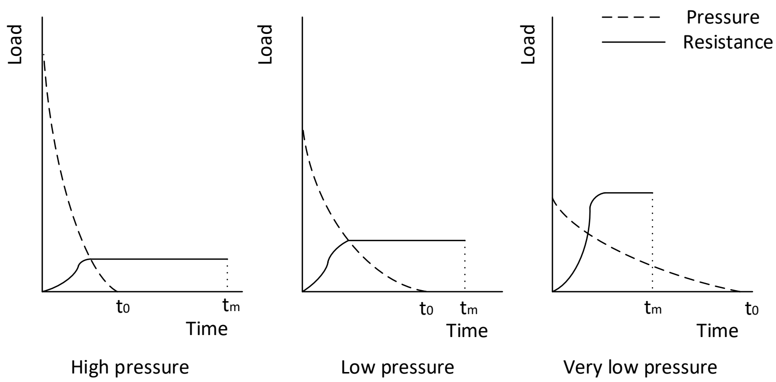

Pressure design range	High	Low	Very low
Design load	Impulse	Pressure-Time	Pressure
Incident pressure	>> 690 kPa	< 690 kPa	< 69 kPa
Pressure duration	Short	Intermediate	Long
Response time	Long	Intermediate	Short
t_m/t_0	$t_m/t_0 > 3$	$3 > t_m/t_0 > 0,1$	$0,1 > t_m/t_0$

Figure 1.8: *Parameters defining pressure design ranges [Unified Facilities Criteria, 2008]. Units in the table are transferred from US units into SI units.*

1.4 Pressure history at a point

At any point away from the burst, the pressure distribution has the general shape shown in figure 1.9 with regard to time. The shock front arrives at a given location at time t_a and, after the rise to the peak value, p_{so} the incident pressure decays to the ambient value in time t_0 which is the positive phase duration. This is followed by a negative phase with a duration t_0^- that is usually much longer than the positive phase and characterized by a negative pressure (below ambient pressure) having a maximum value of p_{so}^-, as well as a reversal of the particle flow. The negative phase is usually less important in design than the positive phase, and its amplitude p_s^- must, in all cases, be less than the ambient atmosphere pressure p_0. The incident impulse associated with the blast wave is the integrated area under the pressure-time curve and is denoted as i_s for the positive phase and i_s^- for the negative phase.

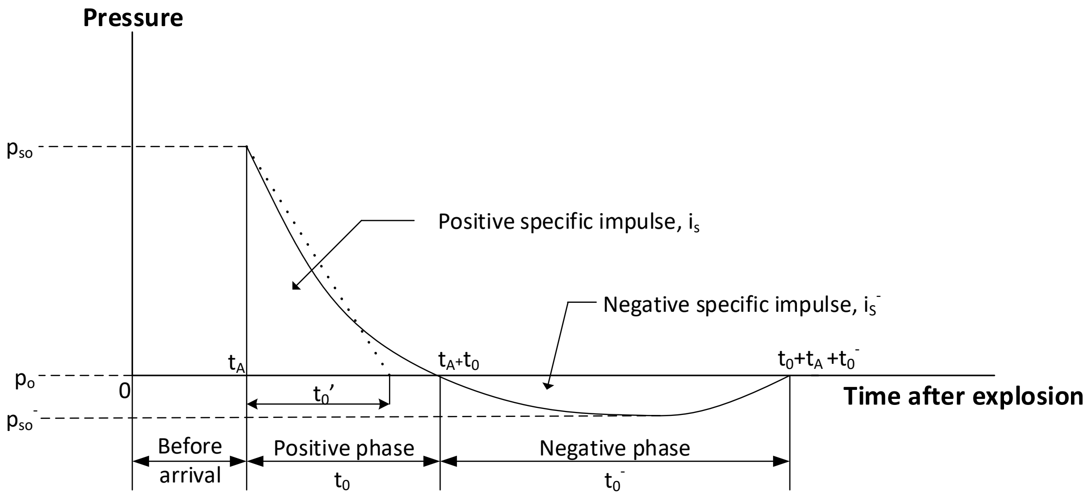

Figure 1.9: *Free field pressure-time variation, modified from [Unified Facilities Criteria, 2008].*

The above treatment of the blast wave phenomena is general. The magnitude of the various parameters must be defined depending upon the category of the detonation as described in chapter 2. The pressure history at a point located at 0,5 m distance from the explosive centre, which represents the case of exploding a hand grenade DM51 under the Humvee floor, can be categorized as a surface burst, [Unified Facilities Criteria, 2008].

At a stationary point in space, the effects of positive pressure air blasts have frequently been modelled with a modified Friedlander's equation [Guzas and Earls, 2010] as

$$p(t) = \begin{Bmatrix} 0, & t < t_A \\ p_{max}\left(1 - \frac{t-t_A}{t_0}\right) e^{-b\left(\frac{t-t_A}{t_0}\right)}, & t_A \le t \le t_A + t_0 \\ 0, & t > t_A + t_0 \end{Bmatrix} \tag{1.1}$$

where $p(t)$ is the overpressure at time t after detonation, p_{max} is the peak overpressure, t_A is the arrival time of the shock wave, t_0 is the positive duration of the shock wave, and b is the decay-constant. Depending on whether or not the point of interest is located on the surface of an object, p_{max} is either equal to p_{so}, the peak side-on overpressure (in free air) or p_r, the maximum reflected overpressure (upon shock wave reflection at a rigid surface). All these parameters are shown in figure 1.9.

The impulse per unit area of projected surface, also called the specific impulse i, can be obtained by integrating the pressure function from eq. 1.1

$$i = \int_{t_A}^{t_A+t_0} p(t)\,dt = p_{max}\,(t_0)\left[\frac{1}{b} - \frac{1}{b^2}\left(1 - e^{-b}\right)\right] \tag{1.2}$$

where i is either the reflected or side-on impulse based on what p_{max} is used in eq. 1.1.

1.5 Thesis scope and limitations

The scope of the thesis is to design a composite armour plate capable of withstanding the blast threat from explosives. Furthermore, the plate has to be able to withstand incoming fragments due to the explosive. This is not the main concern of this thesis, but some degree of protection against fragments is incorporated due to the design of the blast panel. Specific ballistic protection may be ensured by using a disruptive layer of ceramics and fibre-polymer designed by Composhield at a later stage. Additionally, it is desired to determine a novel structure capable of absorbing a great amount of energy while still maintaining structural rigidity to be used as discrete fixation points in-between the composite armour plate and the vehicle structure/chassis.

Additive manufacturing methods (3D-printing) of metallic structures are gaining significant acceptance in different industries as the use/possibilities of components manufactured using these methods can be specifically engineered and the cost of the components likewise decrease as the technology matures. A design of the discrete fixation points is therefore not limited to geometries which are manufacturable using conventional methods. As the methods and techniques are further developed and the cost decreases the structure may be used in larger scale for relevant specifications.

The tasks of the thesis are the following;

1) Determine the temporal and spatial distribution of the load in both the armour plate, and discrete fixation/mounting points.

A blast wave creates an impulse of the surrounding air particles and thereby a time dependent, often high, load on the armour panel and mounting points. The distribution and magnitude of this impulse is necessary to determine for design purposes.
Methods: Two methods are used in determining the load on the structure. The impulse is determined from models developed on empirical data obtained in extensive test programs conducted in the US army. The residual load, i.e. the load transferred to the structure/chassis, is determined by analytical models.

2) Investigate the metallic foam presently used in the composite armour plate for determining the energy absorbing properties and ability to withstand multiple blast waves.

This includes investigation of the effect of cell size, foam density, thickness of skin and foam etc. The foam has to be relatively cheap as it is used for a large percentage of the surface area of the vehicle. The ballistic protection is assumed to be covered by Composhield and their already extensive knowledge of ceramic/fibre-polymer compositions.
Methods: Quasi-static compression tests are performed on the foams using a test machine. Dynamic tests can be performed in the terminal ballistic lab impacting the foam with a blast wave representative projectile. Numerical simulations in ANSYS Autodyn are likewise performed. The multi-hit ability needs in all probability to be live-blast tested.

3) Investigate the effect of geometry and/or composition of the armour plate for the Humvee floor on energy absorption, structural integrity etc.

This is an investigation of the effect of thickness, mass of the front plate, energy absorber, back plate and to determine the composition of components for the plate. It also includes an investigation of different concepts, e.g. wave deflection mechanism, and how these enhance the armour capabilities of the protective panel. It is all to be conducted with focus on the reaction force on the backside of the armour plate. This can be used to calculate the deflection in the chassis. However, this has to be achieved without sacrificing the very important ground clearance of the vehicle, i.e. significant gains are necessary before forsaking ground clearance, and without increasing the weight of the vehicle uncontrollable to maintain the tactical ability of the military application. To not permanently damage the chassis of the vehicle, the collapse load of the foam/sacrificial layer has to be kept below the elastic capacity of the chassis.
Methods: Analytical methods using energy conservation and numerical methods using hydrocode are utilised for this part of the thesis. Experiments in the terminal ballistics laboratory are performed using a blast wave replicating projectile, and a live-blast test may be an option.

4) Design the discrete energy absorption points for the assembly of the armour plate and the chassis.

This includes a structural design capable of high energy absorption and structural rigidity for protection of the vehicle structure, i.e. chassis. A novel design may be an option along with unconventional manufacturing methods.
Methods: Numerical tools and parametrisation is used in determining a suitable structure. The proposed structure is produced by additive manufacturing on available 3D-printers, and experimentally validated afterwards.

5) Parametric study of the armour panel.

Different design concepts and combinations are investigated and a single design is chosen. The parametrisation is performed on a local scale during the design of the individual components of the armour solution, but mainly focused on a single design just before the final design is chosen, as a method of saving time.
Methods: A literature study of possible design concepts followed by a numerical study in ANSYS Autodyn and Explicit dynamics.

6) Experimental validation.

This includes creating a representative blast wave in the terminal ballistics lab and conducting experiments that are sufficiently realistic. A pendulum for the dynamic testing of the foam is designed and manufactured, appendix H. The tests are performed for verification of the comparisons made, and of the designs. The difficulty is replicating a blast load in the laboratory without using explosives. It is therefore desired, to also perform a live-blast test.

1.6 Thesis summary and outline

The following section presents the outline of this thesis, and serve as a quick overview of the report along with some of the incentives of the different chapters.

Chapter 1, the present chapter presents the project by a short outline of the effects of a dynamic event such as an explosive along with a brief discussion of the historical context of research in blast waves. This is followed by a presentation of the collaborative partner of the project Composhield A/S and the objective of the project. A vehicle, the HMMWV M1165, is presented as the case vehicle for which an armour plate to be mounted in the floor of the vehicle is desired. A brief discussion on the blast effects influencing both personnel and the structural response of the vehicle follows as a short introduction to the problems in protecting a mechanical structure against explosive threats. The chapter is concluded by the scope and limitations of the thesis and the thesis outline.

Chapter 2, the problem definition presents the mechanics of blast waves, equivalent TNT, scaling laws, shock propagation and energy absorption which all are the basic theory utilised throughout the project. The case explosive, a hand grenade DM51, consisting of 0,0979 kg TNT equivalent explosive is determined in the chapter using the relative energy between the actual explosive in the hand grenade, PETN, and TNT.

Chapter 3, the problem formulation presents the requirements for the armour plate based on the information from the preceding chapter and defines the basis of evaluation for the design concepts throughout the design iterations.

Chapter 4, the prediction of the blast load using two different methods are presented in this chapter. Both methods are based on a great quantity of empirical data obtained throughout extensive test programs conducted by e.g. the US army resulting in i.e. the blast prediction software ConWep (Conventional Weapons). The purpose of the chapter is to investigate the methods most suitable for use in the remainder of the project, which conclusively is the ConWep software. Initially, the chapter presents the most important blast parameters in determining the blast effects which finally are calculated for the earlier mentioned case explosive, the DM51 hand grenade.

Chapter 5, the investigation of the aluminium foam for use in blast resistant armour. In this chapter, a study of the material properties of an aluminium foam is conducted in anticipation of using it in the blast resistant armour. The studies show a very inhomogeneous material, due to difficult manufacturing control. Therefore, an alternative for designs requiring strict tolerances is investigated and a lattice structure, i.e. micro-truss structure, is determined as a highly modifiable alternative. However, the aluminium foam is still desired for large areal applications due to the favourable price, why analytical models are considered in the following chapter.

Chapter 6, the analytical models investigate the deformation in the foam using energy conservation. The models are used in determining the optimum mass distribution between the front buffer plate, and the metallic foam. An analysis of minimising the mass, and an analysis in minimising the thickness of the panel is conducted. The profile of the bulge is determined, along with the effects of membrane and bending deformation modes. Finally, the analytical models of deformation and energy analyses are compared with the numerical equivalent models.

Chapter 7, the numerical simulations present the methods, models and considerations when using hydrocodes in ANSYS Autodyn and ANSYS explicit dynamics.

Chapter 8, the design chapter presents different concepts utilising different methods of energy dissipation or absorbing in reducing the residual load transferred to the structure. The concepts are studied in the first iteration and the best compromise is picked and further enhanced in the second iteration of the design. Here, a parametric study is conducted for getting closer to the utopia point, i.e the optimum design. This probably has to be combined with some sort of ballistic protection in Composhield's possession for fragments and bullets in case of ambushes. A final design is hereby determined.

Chapter 9, the experimental work describes the experiments to be conducted in the terminal ballistics laboratory in near future for verification of some of the problems and discrepancies experienced between the analytical and numerical models. Furthermore, a live blast test is outlined including the use of strain gauges if the opportunity to conduct a live test turn up. This also includes some basic strain gauge theory. Finally, the assembly of the armour panel is described including some weak points in need of some consideration.

The interconnection of report and project is shown in figure 1.10.

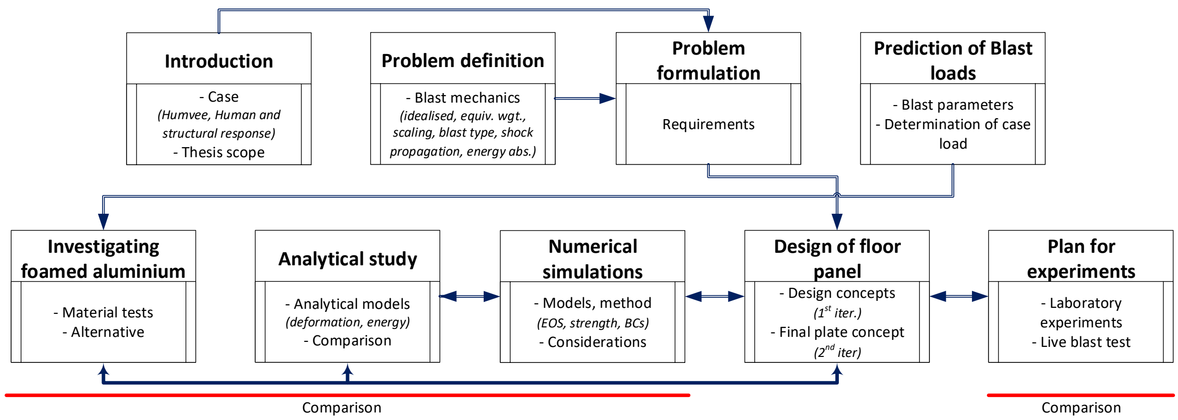

Figure 1.10: *Interconnection of the project and report.*

2 | Problem definition

The following chapter serves as an introduction to the mechanics of blast wave propagation and energy absorption. Theory of terminal ballistics, i.e. the study of projectile/-target interaction is omitted, as it is not the main focus of this project.

An explosion is a fast chemical reaction, in this case involving a solid, during which release of energy and hot gases take place rapidly, [Karlos and Solomos, 2013]. The phenomenon, usually, lasts for a few milliseconds only, and generates high pressures and temperatures. The wave propagation, spherically in an unbounded medium, is due to the expansion of the hot gases and the surrounding air. The resulting pile-up of the molecules in a layer of compressed air is the blast wave and shock front, in which the majority of the energy released in the detonation is contained, [Karlos and Solomos, 2013]. As the wave expands, it experiences a decay in strength and a decrease in velocity but lengthens the duration.

2.1 Idealised blast wave

A blast wave is; *"a shock wave which decays* [drastically] *immediately after the peak is reached"*, [Needham, 2010]. A shock is a discontinuity of density, stress, pressure (displacements are continuous) that propagates in a material continuum, [Davison, 2008]. Conservation of mass, momentum and energy are satisfied at this discontinuity as is the case for steady smooth wave propagation. A steady wave is therefore interpreted as a shock, if the thickness of this, compared to the other dimensions, is small, [Davison, 2008].

Figure 2.1 represents a blast wave parameter at a finite time following a shock. At the front of the shock, the parameter reaches a peak value in an infinitesimal time-step, and immediately starts decaying towards a negative phase, [Needham, 2010].

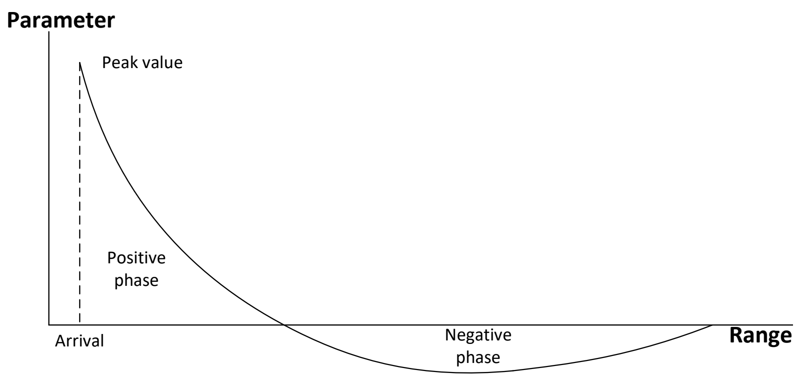

Figure 2.1: *A fully developed representation of a general blast wave parameter. The parameter may represent the pressure, density or velocity at a given time, as a function of range (time, distance). [Needham, 2010].*

For an ideal case representing the pressure/time-history, i.e the blast wave parameter is the pressure as a function of time, see figure 2.2. The figure represents a pressure in relation to time for a free-air blast wave, reaching a target a distance from the detonation point, [Karlos and Solomos, 2013]. The initial pressure at the target is equal to the ambient pressure, p_o. When the front of the shock reaches the target at the arrival time, t_A, the pressure instantaneously increases from the ambient pressure, p_0, to the peak pressure, p_{so}, (or peak overpressure). The time of increase in pressure is usually neglected and set to zero, i.e. a discontinuity. An increase in the distance to the detonation point from the target means a decrease in peak overpressure, along with the propagation velocity of the wave, figure 2.3. Following the peak pressure, the value decays as a power law – *the inverse of the cube of the distance due to the volume of the sphere and that pressure times volume remain constant* – until it reaches the ambient pressure at the time t_A+t_o, where t_o defines the time of the positive phase. The negative phase represents the duration the pressure is lower than the ambient pressure, and the duration of this phase is longer than the duration of the positive phase, [Karlos and Solomos, 2013]. Duration and lowest pressure is designated as t_o^- and p_{so}^- respectively. In the negative phase, the target is subjected to suction forces why fragments etc. might be found on the exterior of the target. The negative phase is often disregarded in design purposes, as the main structural damage in a target occurs in the positive phase, as is seen by the magnitude of the pressure, [Karlos and Solomos, 2013]. The impulse, I_s, of the blast wave is determined as the shaded area in figure 2.2 and describes the total force applied on the target structure due to the blast wave. For the positive phase,

$$I_s = \int_{t_A}^{t_A+t_o} p_s(t)\ dt \tag{2.1}$$

The distance between the detonation point and the target is one of the primary parameters when determining the peak overpressure and velocity of the blast wave. As mentioned above, the magnitude of both decreases rapidly when the distance increases. The effect of the distance on the peak overpressure for the positive phase alone is seen in figure 2.3.

2.2 Equivalent explosive weight in TNT and appropriate scaling law

The explosives used in experiments, analyses etc. are according to the universal procedure recalculated to equivalent TNT (tri-nitro-toluene) in kilograms. This is done even though the physical properties, such as geometry, of the explosive affects the initial characteristics of the blast wave it is found that at a reasonable distance from the detonation centre all blast waves share the same common configuration, wrt. geometry it converges towards a spherical blast front. The effect of the explosion is therefore comparable by calculating equivalency and using scaling factors. TNT is chosen as the norm quantity, as the blast characteristics resemble most of the known solid type explosives often used in IEDs (improvised-explosive-devices) and controlled explosions for demolitions.

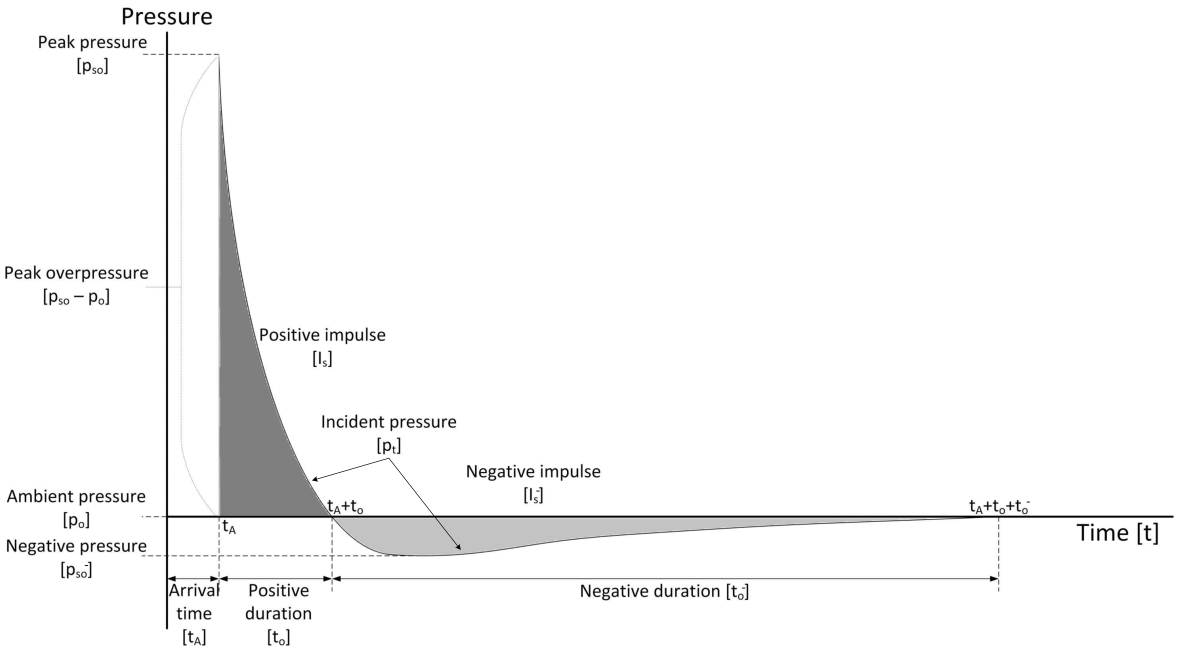

Figure 2.2: *Pressure history of an ideal blast wave. [Karlos and Solomos, 2013]*

.

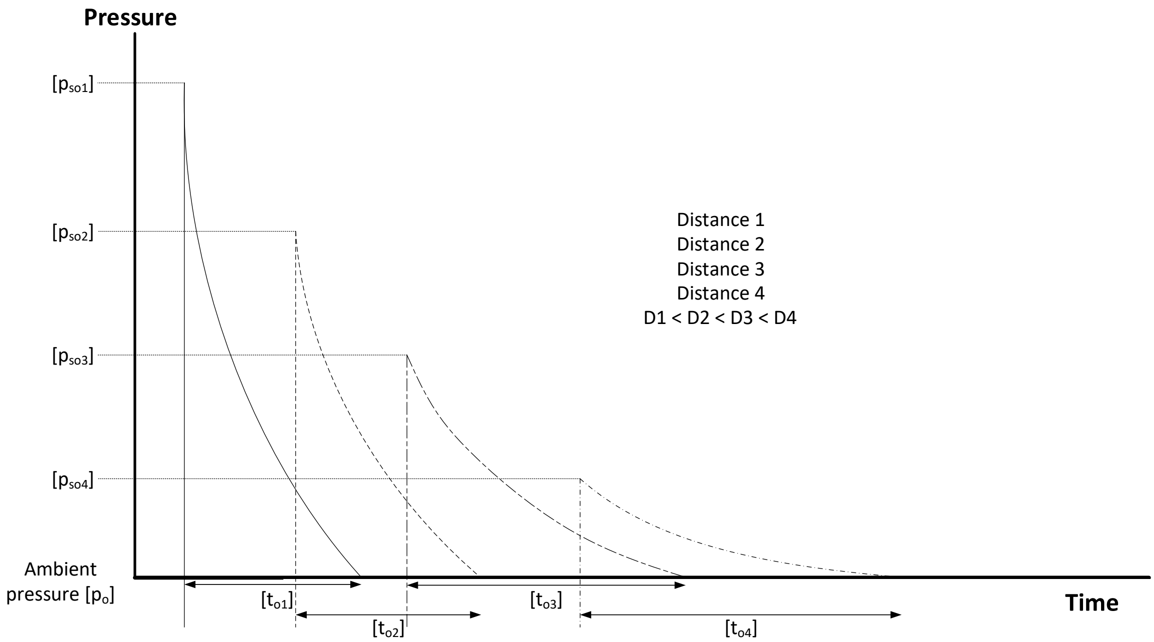

Figure 2.3: *Peak overpressure at the positive phase for different distances from target to detonation point. The duration of the positive phase increases with increasing distance. [Karlos and Solomos, 2013].*

The equivalent amount of TNT, in kg, for a given explosive is defined by chemical energy equivalence [MJ/kg] generated in the detonation as,

$$W_e = W_{exp} \frac{H^d_{exp}}{H^d_{TNT}} \tag{2.2}$$

where W_e is the TNT equivalent weight, W_{exp} is the weight of the actual explosive, H^d_{exp} is the heat of detonation of the actual explosive and H^d_{TNT} is the heat of detonation of TNT, [Karlos and Solomos, 2013].

As a case for the project, one can assume that the explosive targeting the floor of the Humvee is generated by a standard hand grenade DM51. This grenade contains 60 g of PETN (Penta-erythritol-tetra-nitrate) which approximately generates H^d_{exp} = 6,69 MJ/kg of heat in the detonation. TNT approximately generates H^d_{TNT} = 4,10 MJ/kg of heat during detonation, [Karlos and Solomos, 2013]. This, using eq. 2.2, yields,

$$W_e = 0{,}0979 \text{ kg}$$

of equivalent TNT.

By use of scaling laws, it is possible to obtain blast wave parameters at varying distances for any size of explosive. The most used scaling law is the one introduced by Hopkinson-Cranz and known as the cube root scaling law. The idea is, that for detonation of two explosives of similar geometry and located at the same scaled distance to the target, but different in weight, similar blast waves are created if the explosion is conducted in the same atmosphere, [Karlos and Solomos, 2013]. The scaled distance is then,

$$Z = \frac{R}{\sqrt[3]{W_e}} \tag{2.3}$$

where R is the distance from the detonation centre to the target (point of interest), and W_e is the TNT-equivalent weight of the explosive meaning Z has a unit of m/kg$^{1/3}$.

Hereby, it is possible to scale an experiment using a controlled amount of explosive to any given actual case.

2.3 Relative position of explosive and the resulting blast-loading type

The blast wave interacting with the target is greatly dependent on the relative position of the explosive compared to the target. Only external, free and non-contact explosions are treated in this project. Three basic types of cases exist dependent on the height, H^*, of the explosive above ground and the horizontal distance, R_G, between the detonation point, W, and the target, [Karlos and Solomos, 2013]. These are seen in figure 2.4.

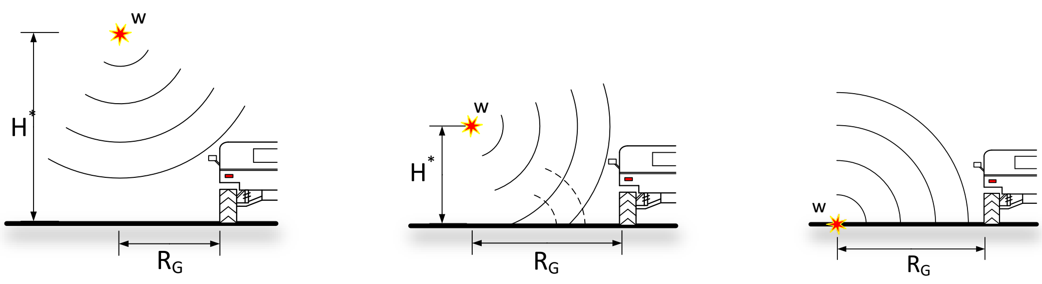

(a) Free-air blast. (b) Air blast. (c) Surface blast.

Figure 2.4: *The definition of the three basic cases dependent on the height above ground, and the horizontal distance to the target.*

Case a): **Free-air blast.** The explosive is detonated in free air, and the waves propagates spherically, dependent on the geometry of the explosive, outwards from the detonation centre. The waves do not interact with any obstacle, i.e. surface/ground, before impinging the target. [Karlos and Solomos, 2013].

Case b): **Air blast.** As in case a), the explosive detonates in the air, but the spherical propagation of the blast waves impinge the target after interaction with an obstacle, i.e. the ground. This results in the creation of a reflective wave, and a mach stem/mach wave front. [Karlos and Solomos, 2013].

Case c): **Surface blast.** The explosive detonates on the surface, i.e. ground. The blast waves immediately interact with the ground and is amplified, and hemi-spherically propagates outwards and impinging the target. [Karlos and Solomos, 2013]. This is the primary case of this thesis.

The effect of the interaction with the ground results in a reflected wave, which has a very different (often higher!) intensity and thereby effect on the pressure applied on the structure.

2.3.1 Reflection wave (mach stem)

The pressure pattern of the blast wave is different from the idealised case in figure 2.2 after interaction with an object, i.e. a reflected wave. The reflected pressure on a rigid surface is larger than the peak incident pressure, p_{so}, [Karlos and Solomos, 2013]. *"For an ideal linear-elastic solid the air-particles rebound freely from the surface as a reflected pressure equal to the incident pressure equalling a doubling of the acting pressure. In a strong non-linear blast wave, the reflection of the air-particles is hindered by the continuing quantity of particles arriving at the surface from the remainder of the wave, thus leading to a much higher acting pressure as the particles build up"*, [Karlos and Solomos, 2013], and figure 2.5. The ratio of which the reflected pressure is larger than the incident pressure is dependent on geometry, angle of reflection, type of blast, size, weight and distance to/of explosive and the interference of reflected waves from other objects.

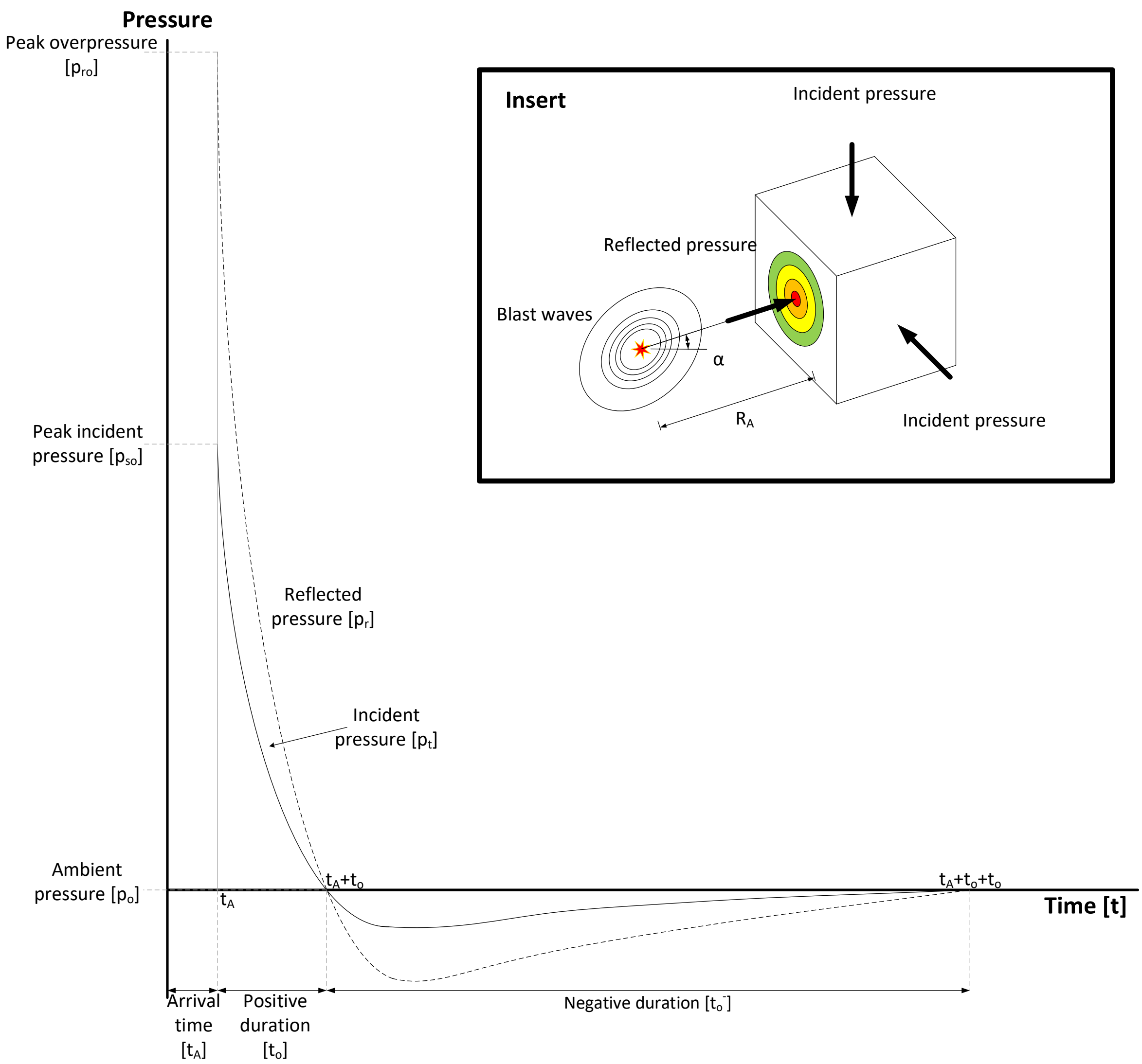

Figure 2.5: *Pressure history of the reflected and the incident pressure. The insert image shows the most severe case, i.e. the reflected pressure is largest on surfaces perpendicular to the blast waves, and the peak incident pressure is the equal to the reflected pressure on surfaces parallel to the blast waves, i.e. the mildest case. This means, that the reflected pressure is always greater than the incident pressure, by a factor of 2 - 8 times in ideal cases, experimental findings show it to be even larger for very close explosion due to dissociation effects in the gases. The reflected pressure is greatest at a normal to the detonation source,* R_A*, and decreases with the incidence angle,* α*. [Karlos and Solomos, 2013].*

The effect of the angle of incidence α (fig. 2.5 insert) is negligible while one still achieves a conservative design, as the pressure only decays with increasing angle of incidence. For angles of incident between $40° - 55°$ (fig. B.4), the reflected wave behaves a bit different due to the creation of a mach stem, also called irregular reflection. The mach stem is created due to coalescence of the incident wave, and the reflection wave, [Karlos and

Solomos, 2013]. The intersection of the incident, reflected and mach waves is known as the triple point (fig. 2.6). The mach stem is assumed to have a constant value throughout the height, the creation of a mach stem is shown in figure 2.6.

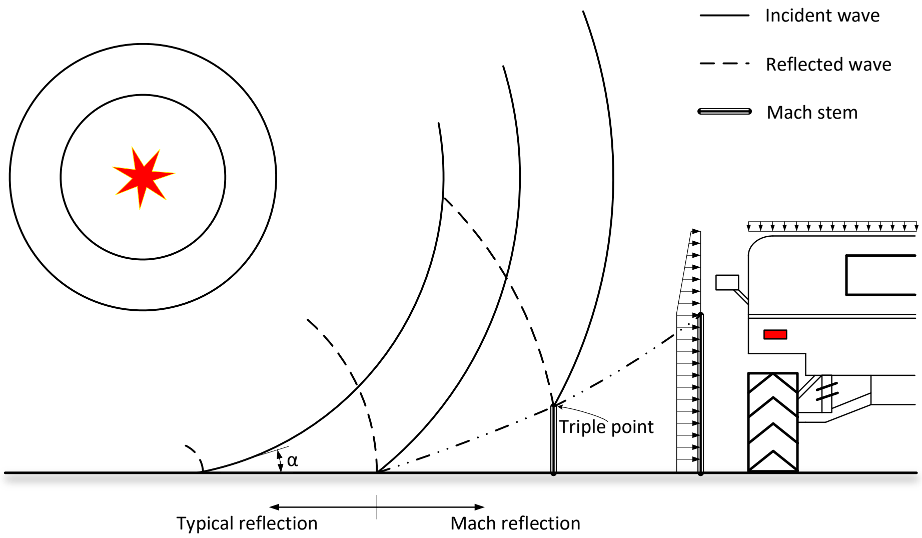

Figure 2.6: *Creation of a mach stem. The height of the mach front increases with an increase in propagation. The time-pressure history of the mach front is similar, but greater, to the ideal time-pressure history of figure 2.2. If the mach stem is higher than the target, the target is loaded by uniform pressure, else, the lower part of the target is loaded by uniform pressure, and the upper part (above triple point) is loaded by the combined pressure of the incident and reflected wave. The uniform load of the mach front is largest, and can be used as design criteria for the entire structure. [Karlos and Solomos, 2013].*

2.4 Shock wave propagation in foams

As the foam experiences a disturbance, the effect of this disturbance propagates through the foam, first as an elastic wave. If the disturbance is sufficiently large or of sufficiently high velocity, the wave is a plastic wave.

An idealized nominal compressive stress-strain curve for a metallic foam is shown in figure 2.7.

When a foam experiences an impact, an elastic wave propagates through it. If the stress of this wave is above σ_{pl}, it is followed by a plastic wave. A one-dimensional case is considered, fig. 2.8, and it is assumed that the bar is, initially, stationary and stress free, [Ashby et al., 2000]. At $t = 0$, the bar is subjected to a constant velocity v. An elastic wave propagates through the bar at the speed of $c_{el} = \sqrt{E/\rho}$ as a response, and yields a uniform stress of σ_{pl} and a negligibly velocity. Trailing is the plastic wave at speed c_{pl}. Downstream from this front, the stress is σ_{pl} and velocity is $v \approx 0$. Upstream from the front, the stress and strain is given by point D in figure 2.7, i.e. the stress and strain state is σ_D and ε_D respectively. Furthermore, the density has increased to $\rho_D = \rho/(1 - \varepsilon_D)$. [Ashby et al., 2000].

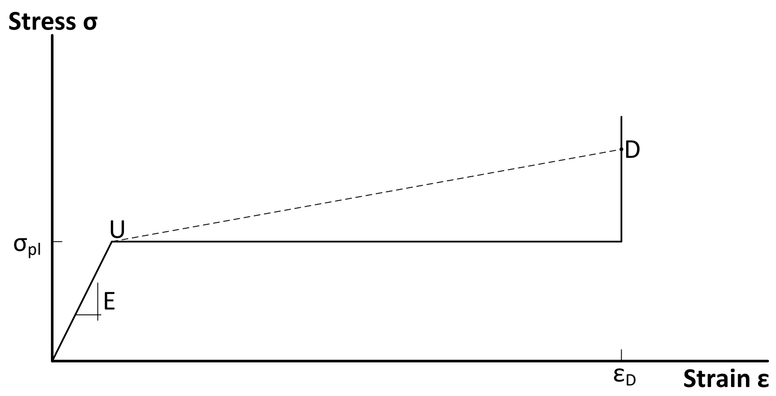

Figure 2.7: *A compressive idealized stress-strain curve for a foam. E: elastic modulus, σ_{pl}: plateau stress, ε_D: densification strain. Compaction/densification of the foam happens at the densification strain. Point D indicates the defined densification stress at the densification strain, and the slope of the line U-D defines the tangent modulus. [Ashby et al., 2000].*

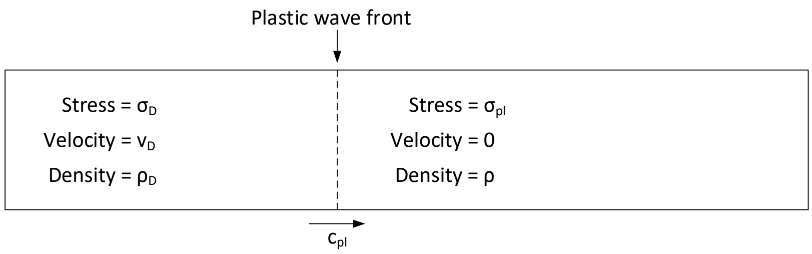

Figure 2.8: *One-dimensional wave propagation.*

The conservation of momentum is used to relate the change in stress $(\sigma_D - \sigma_{pl})$ across the wave front which is related to the change in velocity v_D, [Ashby et al., 2000].

$$(\sigma_D - \sigma_{pl}) = \rho \; c_{pl} \; v_D \tag{2.4}$$

and the change in velocity is related to the change in strain as

$$v_D = c_{pl} \; \varepsilon_D \tag{2.5}$$

From eq. 2.4 and 2.5, the plastic wave speed is

$$c_{pl} = \sqrt{\frac{(\sigma_D - \sigma_{pl})}{\rho \; \varepsilon_D}} = \sqrt{\frac{E_t}{\rho}} \tag{2.6}$$

where E_t is the tangent modulus, which is the slope of the line U-D in figure 2.7.

2.5 Energy absorber

Energy absorbing designs are used in impact structures of vehicles, packaging of products and blast protection. Increasing focus on the composition and manufacturing methods of energy absorbers has resulted in safer and better designs capable of greater absorption protecting the passenger, product, structure etc. ensuring only limited or no damage, [Alghamdi [2001], Ashby et al. [2000]]. The absorbers', whether of metal, plastic or cardboard, method of protection is stated as:

> *"An energy absorber is a system that converts, totally or partially, kinetic energy into another form of energy. Energy converted is either reversible, like pressure energy in compressible fluids and elastic strain energy in solids, or irreversible, like plastic deformation energy"*, [Alghamdi, 2001].

This happens, in a properly designed and employed energy absorber, just below the critical load, i.e. the load that causes damage to the product, passengers etc.

2.5.1 Energy absorption of a blast load

A blast load imparts an impulse onto the absorber and momentum is conserved, [Ashby et al., 2000]. As momentum is conserved, a relation between the level of the load and the duration of influence exists if the buffer plate, necessary due to the impulse, in front of the absorber is accelerated instantaneously to the velocity conserving momentum. Foam which is often used in energy absorbers behaves somewhat linear elastic - perfect plastic, the relation is established as in figure 2.9.

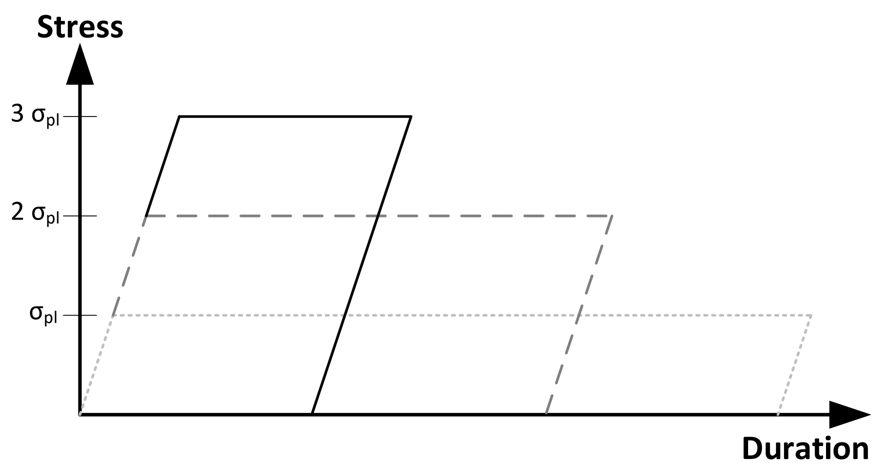

Figure 2.9: *Stress-duration relation of three linear elastic perfect plastic energy absorbers. Each of them absorbs the same amount of energy.*

As mentioned earlier, the energy absorber for this project is to be used in the floor of e.g. a Humvee. The energy is absorbed by plastic deformation, and three modes of deformation exists

- bending
- membrane
- translatory

All three of these deformation modes are utilised throughout the project. An example of the translatory deformation mode is given in the following. A purely translatory deformation mode is utilised meaning the disruptive layer in front of the energy absorber remains rigid and undeformed, an important assumption in the analytical model of section 6. The absorption of the energy in the blast load is done in the blast absorbing layer along with strategically placed fixation points transferring the residual energy to the chassis do to conservation of momentum, figure 2.10.

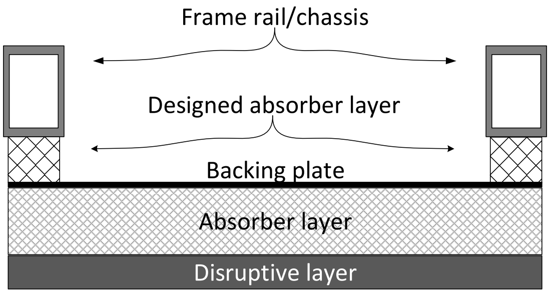

(a) Pre load.

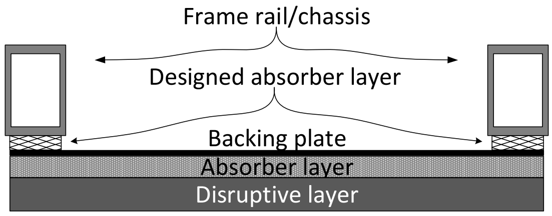

(b) Post load.

Figure 2.10: *General composition of an armour solution for the floor. The designed absorber layer is for cases where well defined material parameters are necessary at a higher cost, or the necessary thickness for using the cheap aluminium foam is impossible, e.g. near the suspension. Problems with the foam are discussed later, in chapter 5. Disruptive layer remains rigid and undeformed.*

It is described earlier how a ballistic panel for defeating fragments, projectiles etc. is not prioritised as the risks of penetration from these threats at this location of the vehicle is limited, and Composhield is in possession of known tools to counteract the threats. However, as stressed and further described in chapter 6, it is necessary to have a buffer plate in front of the energy absorber which conveniently could possess some protective properties such as a disruptive layer of high hardness steel ARMOX 500T or ceramic tiles with a backing plate of steel. The buffer plate is necessary as it protects the foam for complete disintegration during the blast load, and the additional mass greatly reduces the necessary thickness of the foam due to energy considerations.

The focus of material and structure for the absorbing layer is, for this project, foamed aluminium as it is relatively cheap, easy manufacturable in relatively large plates and possess the ideal linear elastic - perfect plastic properties for energy absorption, [Ashby et al., 2000]. Other options are honeycomb structures, truss structures, layered sacrificial claddings ([Karagiozova and Jones [2000], Guruprasad and Mukherjee [2000]]) etc. of aluminium or other materials, whereas novel structures are investigated for the fixation points or replacement of the aluminium foam in critical applications as treated later, section 5.3.

3 | Problem formulation

The following chapter presents the requirements at which the design considerations and evaluations are based on. Furthermore, the requirements quickly summarise the above chapter.

3.1 Requirements

Blast threat protection. The blast threats against the military vehicles vary from mission to mission. In some cases, a hand grenade rolled under the vehicle is the greatest threat, and at other times it might be an Improvised Explosive Device (IED) buried beneath the road surface. Cases of IED-attack from Iraq suggest that the use of artillery shells of 122 mm or larger as the explosive device is frequently used, [Global Security, 2017]. It is therefore suggested to design for a blast threat of a common hand grenade DM51 and consider up to a 155 mm artillery shell. See table 3.1 for the necessary parameters.

	DM51 hand grenade	**155 mm artillery shell M107**
Explosive	PETN 60,0 g	TNT
Equivalent TNT	0,0979 kg	6,62 kg
Geometry of casing	Ø57 mm	Ø154,89 mm
Geometry of pressure wave	Spherical	Spherical
Total weight	0,45 kg	40,82 kg

Table 3.1: *Parameters for the explosive threats considered in the project. The explosives used in the M107 artillery shell is dependent on the manufacture, [Jane's Information Group, 1996]. Even though the casing of the artillery shell is cylindrical, and resulting pressure wave of the explosion in close proximity of the shell will propagate cylindrically as well, it is assumed that the wave is spherical due to the influence of orientation of the shell relative to the vehicle, this is more conservative.*

The Standardization agreement (STANAG 4569) treats the protection of vehicle against kinetic threats, artillery and grenade/mine blasts, [NSA, 2012]. A combined table for the protection levels are shown in table 3.2 for the artillery and grenade/mine blasts. At the moment, is it chosen to design for the STANAG level 1, as the case explosive is a hand grenade, of the DM51 type.

Level	Artillery threat (155 mm)	Grenade and mine threat
1	RoB: 100 m	Hand grenade
2	RoB: 80 m	AT Mine: 6 kg
3	RoB: 60 m	AT Mine: 8 kg
4	RoB: 25 m	AT Mine: 10 kg
5	RoB:* 25 m	N/A
6	RoB: 10 m	N/A

Table 3.2: *Level of protection according to STANAG 4569. Note; the artillery coloumn indicate the minimum distance wrt. to the fragments from the casing of the artillery shell's ability to penetrate the armour, i.e does not indicate the blast pressure. RoB: Range of Burst. *Not an error. [NSA, 2012].*

Lightweight. As the focus of the project is on mobile armour applications for military vehicles, an important parameter to minimise is the weight of the armour solution. Excessive weight has an influence on the mobility of the vehicle with regards to fuel consumption, acceleration, top speed, manoeuvrability and additional cargo load. It is desired to utilise materials and designs offering a high protection level and low weight.
It is difficult to quantify lightweight, so design concepts are compared against the foam panel of equivalent mass, and the residual reaction force.

Ground clearance. To maintain the military strategical operational range of the vehicle, the ground clearance of 400 mm is in an ideal case maintained. This however is almost impossible unless the structural floor of the Humvee is replaced. It is desired to maintain as much ground clearance as possible. A 10% reduction is deemed acceptable, hence the armour panel can be 40 mm in thickness in total. This also include any ballistic protection applied at a later stage.

Mountable. The additional armour for the floor of the vehicle has to be mountable on any variation for the vehicle in question with relative small modifications. The possibility of attaching mounting point on the plate is therefore necessary.

Environment. Reliability of the solution in the operative environment is a necessity. This include resistance to water, great variation in temperature and general wear. Means of avoiding or reducing unnecessary wear are therefore taken.

4 | Prediction of blast loads

This chapter describes the effects of a blast wave produced by a hand grenade DM51 on the target plate. The effects here are represented by the reflected pressure and impulse as described in chapter 2. Two methods of obtaining the blast parameters are applied and compared, whereupon the pressure distribution on the target plate is determined.

Other hazards like fragments are not considered or calculated here, although all types of effects must be included in the final design.

4.1 Blast parameters

Values for the parameters describing the air blast in eq. 1.1 can be found in a few different sources. The work of [Kingery and Bulmash, 1984] includes blast data from numerous different tests, both for side-on and reflected cases, and their data is presented in the form of equations as a function of scaled distance Z. These air blast parameter equations (known as the Kingery-Bulmash equations) serve as the basis for the well-known air blast load generation program, ConWep (Conventional Weapons Effects), which is used in this project.

Blast parameters for design

Numerous sources including military technical manuals, such as TM 5-1300 (US Army 1990), and other sources on design [Guzas and Earls, 2010] suggest a simplification to the decaying exponential blast profile shown in figure 1.9. This approach involves approximating the typical overpressure profile with an equivalent triangular pulse. The peak overpressure, p_{so}, and the impulse, I_s, are preserved but the duration time is modified as

$$t_0^{'} = \frac{2\, I_s}{p_{so}} \tag{4.1}$$

The decay constant, b, is set to zero to give a triangular shape to the blast profile forming a triangular impulse equivalent, as shown by the dotted line on figure 1.9. This equivalent has the same initial peak overpressure but a shorter duration time.

4.1.1 Angle of incidence

The angle at which a shock wave strikes a structure affects the magnitude of the peak reflected overpressure. In fact, there is a complex relationship between the coefficient of reflection, C_r, which is a ratio of the peak reflected overpressure to the peak side-on overpressure, and the angle of incidence, θ. As discussed by [Guzas and Earls, 2010], assuming normal reflection is conservative and easier to implement within a blast generation program. [Randers-Pehrson and Bannister, 1997] assume that the reflected blast overpressure profile is a function of both time and angle of incidence and it is a combination of the normally reflected and side-on blast overpressure time histories. Accordingly, the air blast profile, $p(t,\theta)$, to be applied to an individual finite element at a point in time is calculated as

$$p(t,\theta) = p_r(t)\, \cos^2\theta + p_s(t)\,(1 + \cos^2\theta - 2\, \cos\theta) \tag{4.2}$$

where θ represents the angle between the normal of an element surface, which includes the point of interest, and a line between the point of interest and the blast detonation point as illustrated in figure 4.1. $p_r(t)$ is the reflected air blast profile, following eq. 1.1 with $p_{max} = p_r$, and $p_s(t)$ is the side-on blast profile, which is also computed from eq. 1.1 with $p_{max} = p_{so}$.

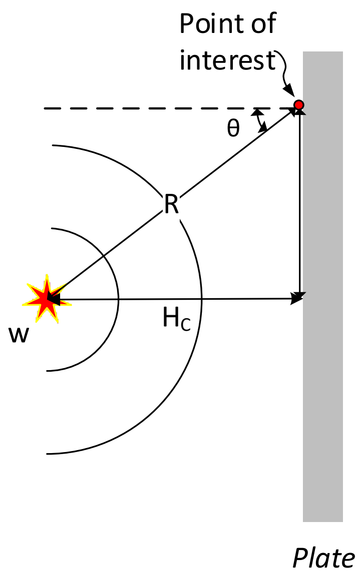

Figure 4.1: *Angle of incidence θ in 2D. H_c is the normal distance from the surface to the detonation point.*

It can be seen from eq. 4.2 that for $\theta = 0$, where the surface normal points toward the blast source, the air blast profile is represented by the reflected air blast profile from which the second term in eq. 4.2 becomes zero.
For all loading options, the incident impulse is calculated as

$$I(\theta) = I_r\, \cos^2\theta + I_s\,(1 + \cos^2\theta - 2\, \cos\theta) \tag{4.3}$$

where I_r is the impulse for normal reflection, I_s is the side-on impulse, and θ is the angle of incidence.

The duration time for the equivalent triangular parameter equations is also a function of this incident impulse

$$t_0^{'}(\theta) = \frac{2\, I(\theta)}{p(t = t_A, \theta)} = \frac{2\, I(\theta)}{p_r\, \cos^2\theta + p_s\,(1 + \cos^2\theta - 2\, \cos\theta)} \tag{4.4}$$

where $p(t = t_A, \theta)$ is the overpressure at the arrival time, from eq. 4.2, p_r is the peak reflected overpressure for normal incidence, and p_s is the peak side-on overpressure.

4.1.2 Hemispherical blast

Explosions located at the ground surface are categorized as a hemispherical blast as mentioned before. In [Unified Facilities Criteria, 2008], separate sets of parameters for spherical and hemispherical blasts are available.

When a charge is detonated at the ground surface, simultaneous reflected waves from the ground are produced, reinforcing the shock wave generated by the initial explosion. The surface charge is shown in figure 4.2(b) with a fictitious complementary hemisphere drawn in a dashed line, below the surface of the ground. A charge suspended in air, is shown in figure 4.2(a). Both charges has the same radius. It is observed that; as long as the ground surface is rigid and frictionless there is no difference in the explosion effects for the space above the charge between (a) and (b). Therefore, if the ground is a perfect reflecting surface, i.e. idealized surface, the effect of the hemispherical charge on its surface is the same as the free air explosion of a charge with the same radius. This is equivalent to a ground charge with weight W, under the conditions described, has the same effect as the air charge with weight $2W$. However, in most real situations a surface explosion results in a crater, which is associated with energy dissipation related to the type of soil. A magnification factor of (1,7-1,8) is, most frequently, used where the approach for hemispherical blast is exactly the same as for the spherical blast, except that the charge weight W is replaced by the equivalent weight, [Szuladzinski, 1940]. The incident pressure p_s from the ground burst may therefore be estimated from the air burst data.

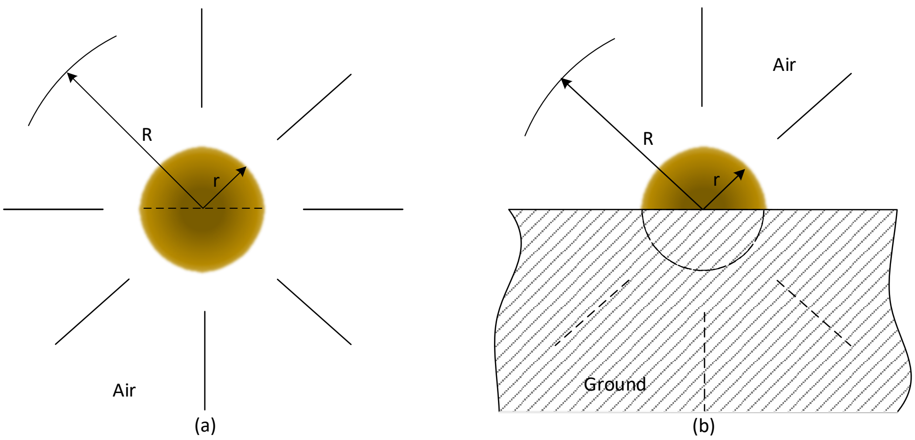

Figure 4.2: *(a): Free-air explosion, and (b): Surface burst. [Szuladzinski, 1940].*

A more accurate magnification factor is based on test results stated in the technical manual [Unified Facilities Criteria, 2008], which are the same data used in ConWep. The results for ten different charge weights with the same range are obtained in both cases, spherical and hemispherical (surface) burst, and the results are compared to estimate the magnification factor for the present case. The charge weights vary between $W/3$ and $3W$. The mean averaged value is found to be 1,644 for the magnification factor.

4.2 Pressure history determination by following Kinney, Graham and Brode

Detailed information, based on empirical data, about peak values of shock overpressure, as taken from [Brode, 1977] and used in [Guzas and Earls, 2010], are used to obtain the blast parameters, see appendix A. The procedure explained in appendix A for finding the blast parameters is applied for free-air burst but can be applied directly for the surface burst by using a magnification factor as mentioned before.

For the studied case, which is a hemispherical explosion, the blast parameters, the peak pressure values, impulses, arrival and positive duration time are obtained based on the same equations after multiplying the charge weight W by a factor of 1,644 as described in the previous section. The results are listed in table 4.1.

Pressure	**Peak pressure** [kPa]	**Impulse** [kPa – ms]	$\boldsymbol{t_A}$ [ms]	$\boldsymbol{t_0}$ [ms]	**Decay coefficient *b*** [ms]
Incident	1340	50,26	0,2215	0,4400	4,555
Reflected	8135	305,37	0,2215	0,4400	4,555

Table 4.1: *Peak pressure and the blast parameters obtained from appendix A.*

The equations used in appendix A to determine the blast parameters assume that the decay coefficient is the same for the incident and reflected pressure and thereby the only difference between them is the peak pressure value. The impulses are calculated using the integral in eq. 1.2.

4.3 Pressure history determination at a point by ConWep

ConWep (Conventional Weapons Effects) is a software developed by the US Army based on graphs and equations in the technical manual TM5-855-1; *Fundamentals of Protective Design for Conventional Weapons*. This software is based on empirical data collected on spherical air and hemispherical surface bursts following detonation of explosives weighing from 1 kg to 400.000 kg.

The studied case is illustrated in figure 4.3, where the plate surface is oriented normal to the wave propagation. This case represents the explosion of a hand grenade beneath a Humvee which is protected by the plate.

The program assumes an exponential decay of pressure with time. The modified version of Friedlander's equation (eq. 1.1) is used in the program to describe the pressure-time relation, where p_{max} is replaced by the side-on pressure or the reflected pressure. Based on empirical data, the air-blast parameters *[the side-on pressure p_{so}, reflected pressure, time of arrival t_A, positive phase duration t_0, and the specific side-on impulse i_s]* are calculated. The program iterates to find the decay parameter b that makes the area under the time-pressure curve equal to the calculated impulse. The program then uses the Friedlander

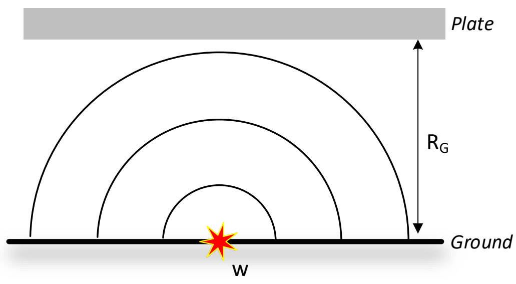

Figure 4.3: *Load case set up for hemispherical air burst. Protective plate located horizontally to the ground above an explosive charge.*

equation to find the pressure values at different time steps.
Note that the time of duration t_0 of the modified Friedlander equation is measured from time $t = 0$.

The program contains a library of standard weapons and lets the user chose from it or even insert new data to define the weapon. For the hand grenade DM51 which is not listed in the library, the data are inserted manually where the total weapon weight is 0,45 kg, the equivalent TNT charge weight is 0,0979 kg and the normal distance to the target is 0,5 m. The program returns the data listed in table 4.2.

Pressure	**Peak Pressure** [kPa]	**Impulse** [kPa – ms]	t_A [ms]	t_0 [ms]	**Decay coefficient** b [ms]
Incident	1299	113,04	0,2377	0,8883	0,0978
Reflected	7705	421,5	0,2377	0,8883	0,0586

Table 4.2: *Peak pressure and the blast parameters obtained by ConWep program for the present weapon (DM51 hand grenade).*

4.4 Comparison of the results obtained by the two approaches

The analysis of the structure accounts only for the positive phase, thereby the arrival time is of no interest and the pressure-time curves are plotted with peak pressure at time $t = 0$. In table 4.3 the results from the two calculations are tabulated. Graphically, the pressure-time history of the two calculations are shown on figure 4.4. The two approaches result in different peak pressures and different positive times. Kinney, Graham and Brode predicts higher peak pressure but much lower reflected impulse which is the main parameter for the design at the high pressure range.

Calculation method	**Peak reflected Pressure** [kPa]	**Specific reflected Impulse** [kPa – ms]	**Time of Duration** [ms]
Kinney et. al.	8135	305,4	0,2185
ConWep	7705	421,5	0,8883
Triangular ConWep	7705	421,5	0,1094

Table 4.3: *Comparison between the blast parameters obtained by ConWep and Kinney, Graham and Brode.*

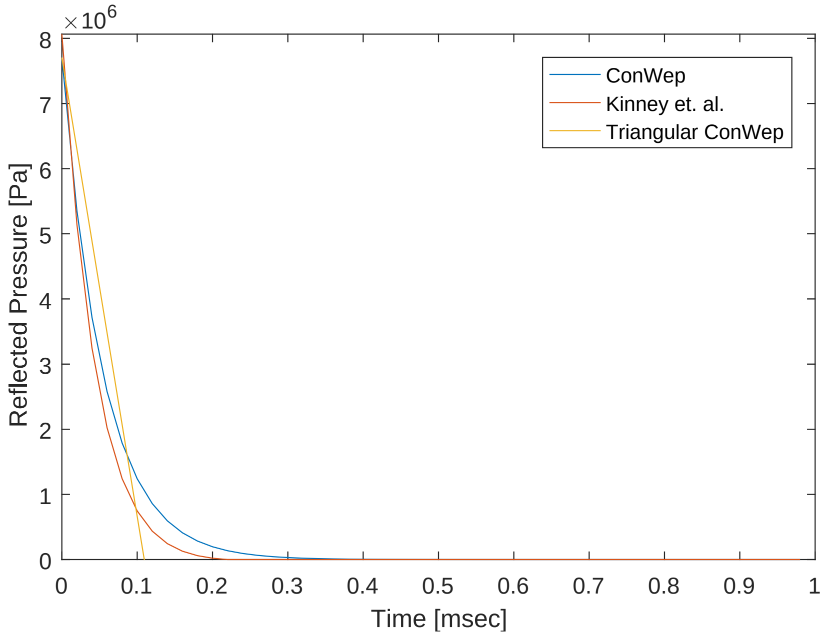

Figure 4.4: *Reflected pressure versus time for two different calculation methods and ConWep equivalent triangular distribution.*

It can be seen that the results obtained by ConWep are more conservative and thereby used for the design of the protective plate in this study.

4.5 Peak pressure distribution on the plate by ConWep

By comparing the results obtained by Kinney et. al. and ConWep program, it can be seen that results from ConWep are more conservative with respect to the impulse. On the other hand the peak pressures obtained by ConWep are slightly lower than results obtained by Kinney et. al. For a peak reflected pressure exceeds 7 MPa, the magnitude of the impulse is of great importance in design, it is thereby chosen to use the results from ConWep which are more conservative.

The peak pressure distribution over the plate is conducted using ConWep software where the parameters used are:

- Plate with dimensions of 1 × 1 m.
- Back surface representing the area of the Humvee floor as illustrated in figure 1.2.
- The distance between the plate and the explosive point is 0,5 m.
- The explosive weapon, hand grenade DM51, has an equivalent TNT charge weight of 1,2 × 0,0979 = 0,1175 kg, where 1,2 is to increase the charge weight a 20% extra as a safety factor [Unified Facilities Criteria, 2008].
- The explosive point is located exactly under the protective plate center at the surface of the ground representing a hemispherical surface burst.

A graphical presentation of the configuration is shown in figure 4.3. Among other parameters the peak reflected pressure, the specific reflected impulse and the duration of positive phase are returned from the program. The solution procedure is explained in appendix B.

Figure 4.5 shows the reflected pressure distribution over all the target plate. These results are obtained by implementing the graphical data in [Unified Facilities Criteria, 2008] using Matlab which are the same data used in ConWep program.

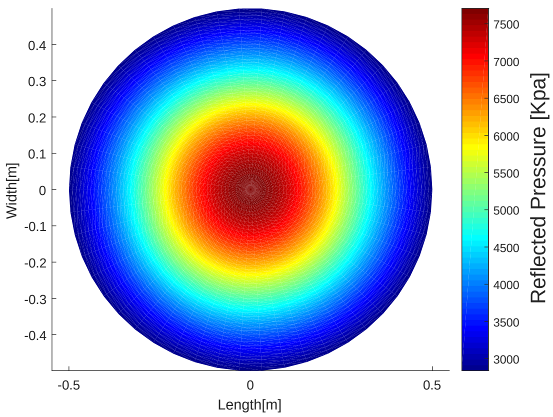

Figure 4.5: *The peak reflected pressure over the target plate based on ConWep software or [Unified Facilities Criteria, 2008].*

The maximum reflected pressure is of course at the closest location of the plate to the detonation point. The distribution follows non-linear relation with respect to the angle of incident and also depends on the distance between the detonation point and the point of interest at the target plate as shown in appendix B.

5 | Investigation of foamed aluminium

In the following chapter, the effect of the cell structure, orientation, and density on the energy absorbing properties of a metal foam is investigated. An alternative structure utilising trusses is also studied as an alternative for the foam as the sacrificial layer in the armour panel, i.e. the energy absorber.

Foamed aluminium is characterised as a cellular solid - as the relative density often is $\rho_f/\rho_s < 0{,}3$ - and is made up by a network of interconnected struts and plates forming the edges and faces of the cells, [Gibson and Ashby, 1997]. The foam exists in two configurations of either opened-cell or closed-cell (fig. 5.1) depending on their manufacturing method, where the opened-cell configuration is regarded as inconvenient and expensive to manufacture. The mechanical properties of the two configurations of foam are very similar whereas the open-cell structures generally are used for cooling applications, [Ashby et al., 2000]. Furthermore, the manufacturing process might introduce smooth sides of the panel resulting in some degree of anisotropy due to these sides of solid material. The level of anisotropy without the solid sides is investigated in appendix C, but the investigation is inconclusive tending to find the foam isotropic.

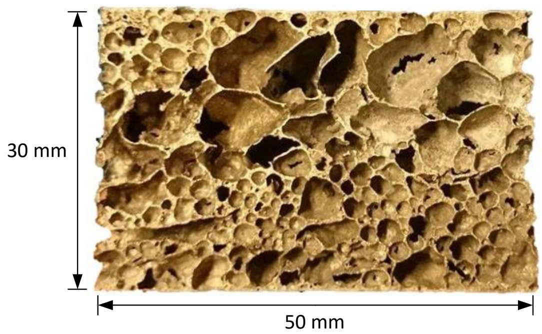

Figure 5.1: *Example of closed-cell aluminium foam. One of the test specimens in appendix C. Note the highly inhomogeneous size of the voids which is a tendency for the entire foam plate from which the test specimens are made.*

5.1 General properties of aluminium foam

The properties of the metal foams are mostly governed by the material used in the production of it and on the relative density. The internal structure of the foam is likewise governing, but is often stochastic and very difficult to account for/imperfectly understood, [Ashby et al., 2000].

As mentioned, when a closed cell deforms, the cell walls bend and the cell faces carry membrane stresses, which often is seen by an increase in stress during the plateau region, figure 5.3(a). Open-cell foams usually show a constant value in this region, as the idealized case in figure 5.3(b). The contribution to the overall stiffness when the cell faces stretch is linear in the relative density, and the contribution to the stiffness due to bending of the cell walls is non-linear in the relative density, [Olurin et al., 2000]. In [Gibson and Ashby, 1997], a relation between the material yield strength, σ_y, and the yield strength/plateau stress of the foam, σ_{pl}, is established from experiments as

$$\frac{\sigma_{pl}}{\sigma_y} = 0{,}3\,\phi^{3/2}\,\bar{\rho}^{3/2} + (1-\phi)\,\bar{\rho} \tag{5.1}$$

where ϕ is the 'distribution constant' and indicates the fraction of solid in the foam contained in the cell edges ($\bar{\rho} \leq \phi \leq 1$) and the remainder of the fraction $(1-\phi)$ is located in the cell face. $\bar{\rho}$ is the relative density of the foam. The definition of the cell faces and edges is shown in figure 5.2 along with the difference between a closed-cell and open-cell foam.

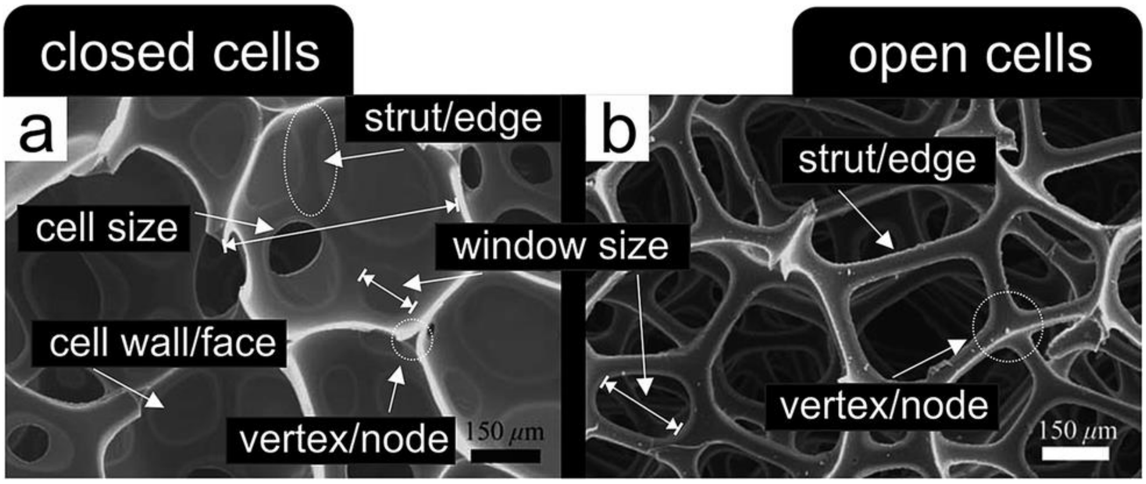

Figure 5.2: *The nomenclature of foams, and the difference between closed-cell (a) and open-cell (b) foams. [Kranzlin and Niederberger, 2015].*

A similar relation for the modulus of elasticity exists as

$$\frac{E}{E_s} = \phi^2\,\bar{\rho}^2 + (1-\phi)\,\bar{\rho} \tag{5.2}$$

where E_s is the modulus of elasticity for the solid material.

For eqs. 5.1 and 5.2, limiting cases are $\phi = 0$ for closed-cell foams, and $\phi = 1$ for open-cell foams. However, it is difficult to quantify the degree closed-cellness, but can for known values be used opposite to define the degrees of closed/open-cellness of the foam. In the present case, a closed cell ($\phi = 0$) yields larger plateau stress and Young's modulus than measured. There is no relation between the common equations, and the measured values, perhaps suggesting the foam has greater variance in the parameters than commonly experienced. Increasing the value of ϕ, i.e. an open-cell foam, ensures convergence.

The energy absorption of foam is given by the area under the stress-strain curve as

$$u = \int_0^{\varepsilon_D} \sigma \, d\varepsilon \tag{5.3}$$

where u is the strain energy density. The densification strain is, in cases where the transition is not obvious, determined as the strain at which the compressive stress is twice the value of the plateau stress σ_{pl}. As the plateau stress also varies, a slight increase is seen for closed-cell foams, this value is determined as the average stress in the range of 5% - 30% strain.

In general, the damping capacity of the foam is five to ten times greater than for the metal it is made of, [Ashby et al., 2000]. This damping capacity is even greater in polymer foams.

5.2 Foam used in the project

A closed-cell aluminium foam of alloy 5556 is available for use in the amour plate as the blast absorbing component. The determined material parameters of the aluminium foam are given in table 5.1.

Material parameter	**Designation**	**Value**			
Density of plate	$\rho_{alu-pla}$	458			kg/m^3
Relative density	ρ_f/ρ_s	0,172			$--$
Modulus of elasticity	E	336	$\pm$	48,8	MPa
Densification strain	ε_D	0,480	$\pm$	0,0504	$--$
Plateau strength	σ_{pl}	4,77	$\pm$	2,18	MPa
Strain energy density	u	2,19	$\pm$	0,573	MJ/m^3
Specific strain energy	e	4737	$\pm$	1324	J/kg
Poisson ratio	ν_{alu}	≈ 0			

Table 5.1: *Material parameters for the aluminium foam plate, please note the high standard deviation. The modulus of elasticity is determined from the unloading slope of the foam, following a plastic strain in the order of 1% as described in [Olurin et al., 2000] to make sure the cells set. This is shown in figure 5.3(c), and the material test is documented in appendix C. As the standard deviation suggests, the variation in the data is large and indicates an inhomogeneous material. This variance is in some cases unacceptable, why an alternative is sought in sec. 5.3.*

The quasi-static engineering stress-strain curve, figure 5.3(a) for selected specimens, for the aluminium is determined in the material test, and resembles other material tests on closed-cell aluminium foams, as there is a strong dependency on the density. For the remaining specimens, see appendix C. Furthermore, the stress-strain curve is dividable into three regions; 1) linear elastic region, 2) collapse region and 3) densification region, [Gama et al., 2001].

As is suggested, region 1 represents the elastic deformation, and is due to bending of the cell walls.

Initially in region 2, the first walls of the cells start to plastically collapse, which is indicated by the slight drop in stress. For the remainder of the region, the cell walls collapse in bending at near constant stress in the foam, commonly known as the 'plateau stress'. For maximum energy absorption it is desired that this region is as long as possible until it reaches the densification strain, ε_D. A slight increase in stress during region 2 is also possible, as the cell faces carry membrane stresses.

In region 3, the foam progressively collapses, densifies, and behaves as the solid material. [Gama et al., 2001]. A quasi-static material test is sufficient, as closed-cell aluminium foams are found to be strain-rate independent, [Yu et al. [1998], Yu et al. [1999], Sriram et al. [2006]]. The test, appendix C, is conducted at a maximum strain rate of $3{,}33 \cdot 10^{-2}$ s^{-1} which relative to the strain rates in a blast load is deemed quasi-static. However, this is assumed to have little influence on the material parameters and they should be valid for a blast application. In compression, the foam behaves almost elastic-perfect plastic, as seen in the idealised stress-strain curve in figure 5.3(b).

A major advantage of the foam is, that as long as it is not completely densified, the plastic stress wave propagating in the material doesn't pass through. As the plastic wave leaves the foam behind fully densified, the plastic wave passes through the foam at the same moment as the full densification occurs.

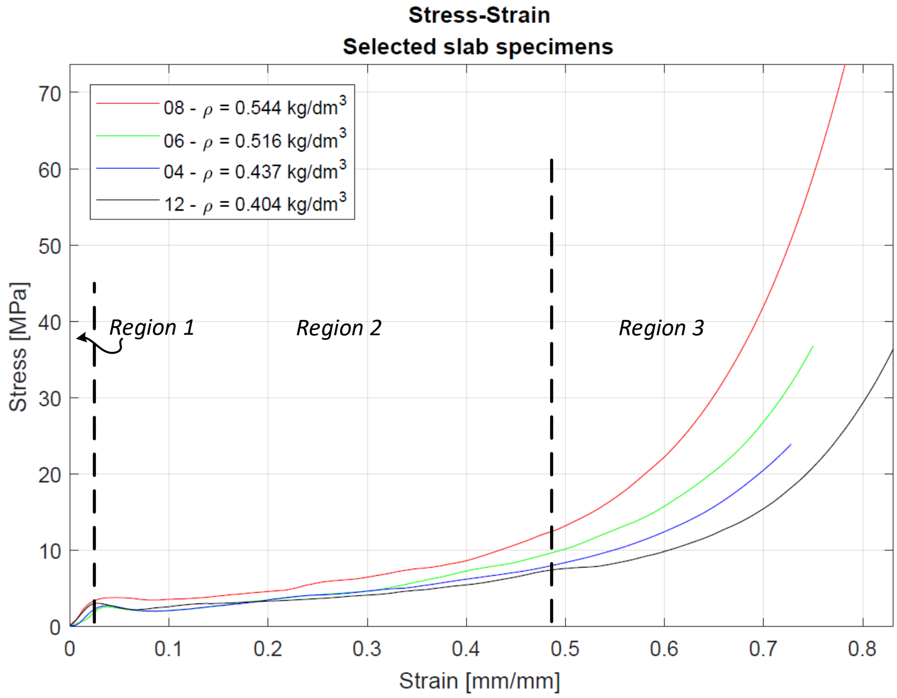

(a) Dependency of the quasi-static stress-strain curve on density for closed-cell aluminium foam. 1) linear elastic region, 2) collapse region and 3) densification region. Notice the drop in load in the low density foam specimens following the linear elastic region, contrary to the high density specimen. This is assessed to be down to the sensitivity of wall collapse and softening in low-density specimens.

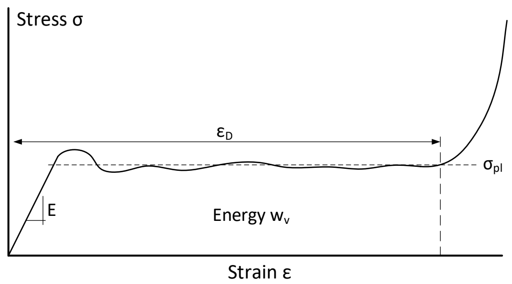

(b) Idealised stress-strain curve for closed-cell aluminium foam. ε_D: densification strain, σ_{pl}: plateau stress, and w_v: specific energy. [Ashby et al., 2000].

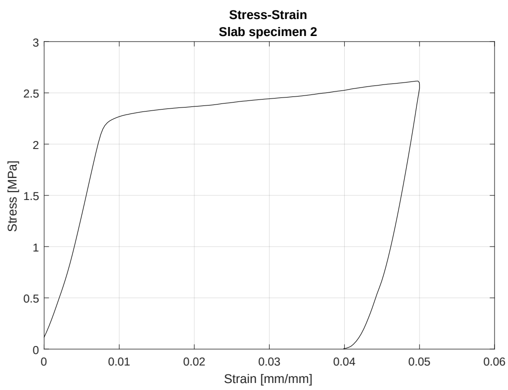

(c) Determination of the modulus of elasticity from the unloading of the foam following a small plastic strain.

Figure 5.3

5.3 An option for replacing the aluminium foam

It is noted throughout the experiments on the aluminium foam, that a great variance in the material parameters is present based on which part of the aluminium foam plate the test specimen is cut from, due to inhomogeneous density distribution as the manufacturing procedure, i.e. control of buble growth, is difficult to control. This is in some applications unsustainable and an alternative is sought, at least for applications requiring well defined material parameters or enhanced material parameters e.g. the plateau strength, but where a higher cost is tolerable, i.e. the mounting points for the armour plate on the chassis.

A micro-truss system is trialled as a replacement for the aluminium foam. The micro-truss plate in figure 5.4 has a core density of $\rho_{\mu-truss} = 274$ kg/m^3 which results in a relative density of $\rho/\rho_s = 0{,}1014$ as it is conceived from aluminium 6061-T6 with a density of $\rho_s = 2700$ kg/m^3. Comparable, this is a lower density than the aluminium Alulight foam described previously, see table 5.1 for the material parameters.

The suggested geometry of the initial micro-truss concept, figure 5.4, is taken from [Queheillalt et al., 2008].

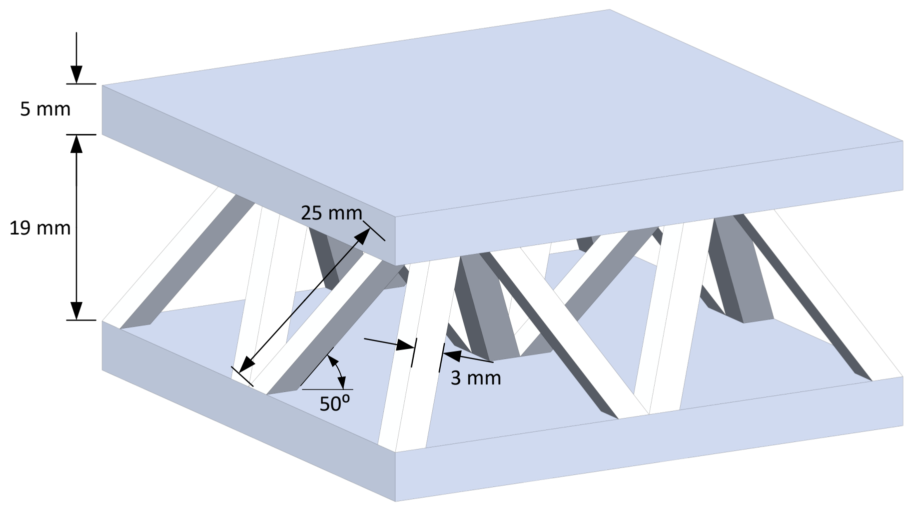

Figure 5.4: *A sketch of the initial micro-truss structure with the independent defining parameters; core thickness, truss width and face thickness. Density of the core is* $\rho_{\mu-truss} =$ 274 kg/m^3. *From [Queheillalt et al., 2008].*

As the micro-truss structure is not manufactured, it is not possible to conduct a material test on a test specimen for determining the material parameters and compare them against the aluminium foam. A comparison by a numerical study is therefore the only option. For the aluminium foam, both experimental and numerical data has been obtained. This data is used for verification of the stress-strain curve obtained using numerical simulations, by comparing it against the data obtained in the foam material test described earlier in section 5.2 and appendix C. This is seen in figure 5.5. It shows a good correlation between the numerically and experimentally obtained strees-strain curve, and it is assessed that numerically obtained stress-strain curves yields a sufficiently accurate representation of the reality in both the linear- (region 1) and plateau-region (2), and can therefore be used for the micro-truss studies self-sufficient.

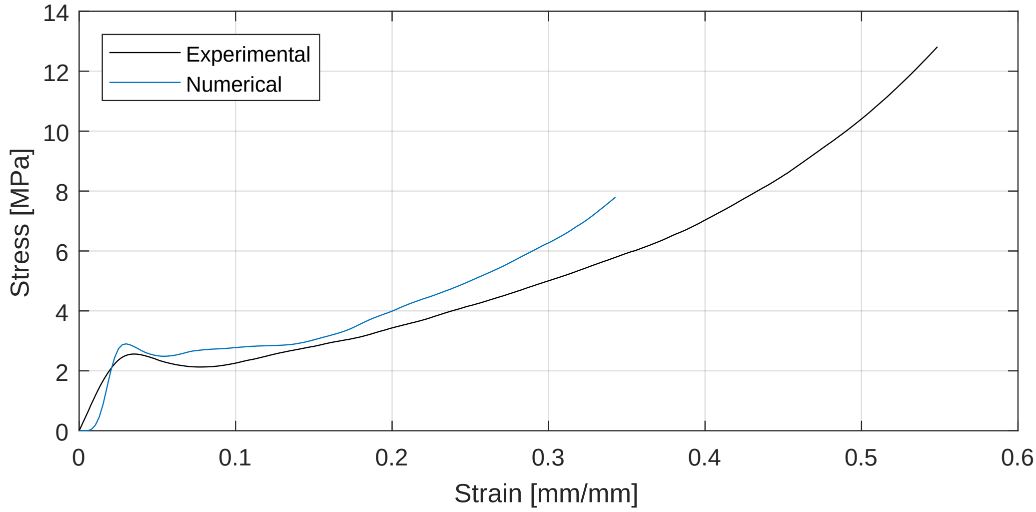

Figure 5.5: *Comparison of the experimental and numerical data for aluminium foam in compression. A satisfying correlation exists and permits a direct comparison of two sets of numerical data for the foam and the micro-truss structure respectively.*

The stress strain curve for the micro-truss structure (fig. 5.4) is shown in figure 5.6. It is seen that a single layer of the micro-truss structure shows relatively great strength until the bifurcation point at where initiation of inelastic buckling of the trusses takes place and a plastic 'hinge' forms. Hereafter the core softens until the deformed trusses make contact with the face sheets, i.e. densification.

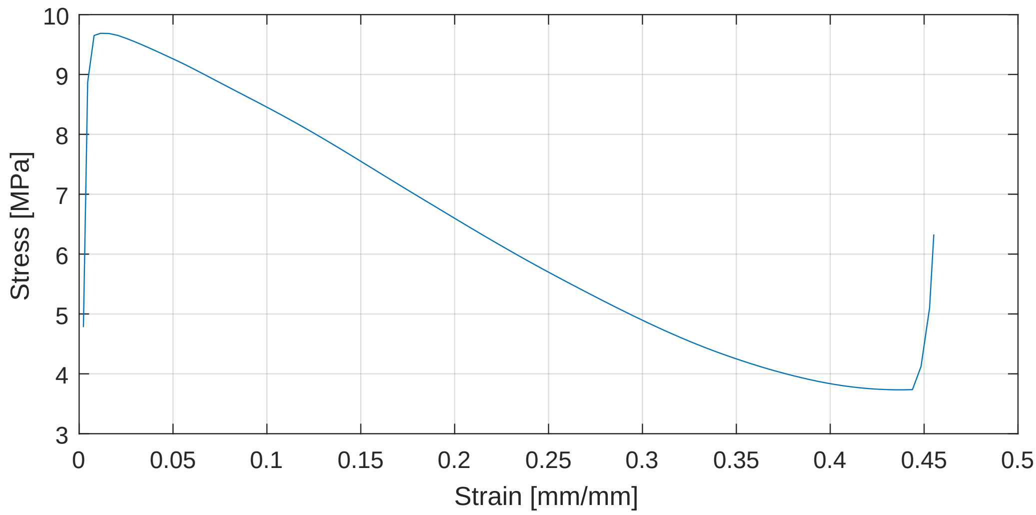

Figure 5.6: *Compressive stress strain curve for the micro-truss structure in figure 5.4. A great amount of softening due to plastic buckling takes place in region 2, i.e. the plateau region. Complete densification is reached at strain 0,44.*

5.3.1 Adjusting the structural response

It is possible to adjust the properties of the micro-truss structure by modifying the geometry of the trusses and adjusting the relative density. The structure is thereby modifiable for a variety of applications, e.g. increasing the layers of the truss structure increase or create a plateau of collapse stresses, see figures 5.7. The boundary conditions, or symmetry conditions, for the models mean that the trusses in the outer planes are restricted from deformation in the outward direction, the effect of this is treated later.

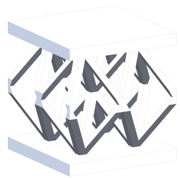

(a) 2x2 structure.

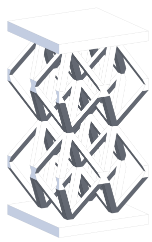

(b) 2x4 structure.

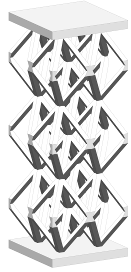

(c) 2x6 structure.

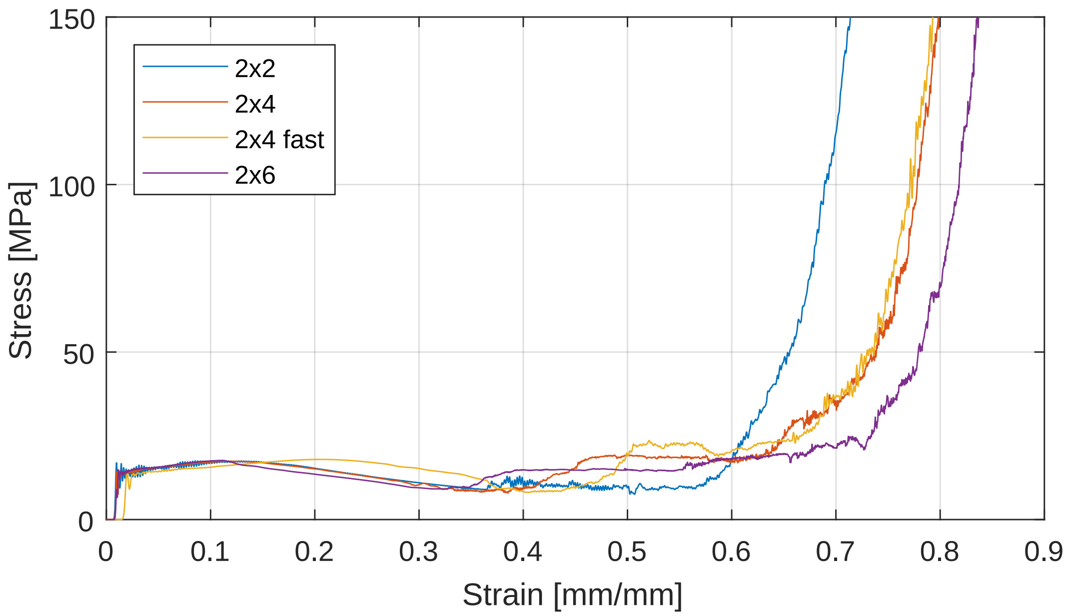

(d) Stress-strain curve for the structures. Initial strain rate for fast: 816 s^{-1}, and for regular: 408 s^{-1}. This also explains the initial shift in the 'fast' curve to a strain twice as large as the other curves.

Figure 5.7: *The effect of multiple layers of micro-trusses. Note the plateau-like deformation similar to the metallic foams, and the method to increase/decrease the duration of this region, i.e. the point of densification. The softening is due to plastic buckling of the trusses. Strain rate independency seems to exists, but for the delayed response. The effects of the boundary/symmetry conditions in the simulations are not exactly disclosed, but believed to indirectly cause the fluctuation in the stress/strain curve as deformed trusses engage/disengage. The effect of width has been tested, and shown negligible differences.*

Different adjustments of geometries are shown in figure 5.8. It is here seen, that the relative density of the core is very important. The two cases of identical relative density show the same level of plateau strength, but in the case of the thin structure, increasing the number of cells stabilise the core behaviour and yield a more constant plateau strength. The aspect ratio in the two cases are identical, so it must be do to the trusses supporting each other. However, this effect is not seen for the 4x4 standard thickness structure, it infacts destabilize the core and thereby the plateau region and one could therefore suspect it is due to numerical discrepancies, i.e. arbitrary mesh generation for each simulation. This might explain some of the fluctuation in the curves.

It is also shown, how the plateau strength can be altered by changing the thickness of the trusses and thereby the bifurcation point and the relative density of the trusses and core geometry. Quite significant differences are achieved by halving or doubling the standard thickness of 3 mm, both for the plateau strength and the densification strain as the increase in thickness of the trusses entail inter-contact sooner. The micro-truss structure is thereby adjustable for specific uses, i.e. the micro-truss structure with a very low plateau strength but a notable high densification strain can be used for protection of delicate components. A normalization of the stresses with respect to the density is performed on the same stress-strain data, and shown in figure 5.9.

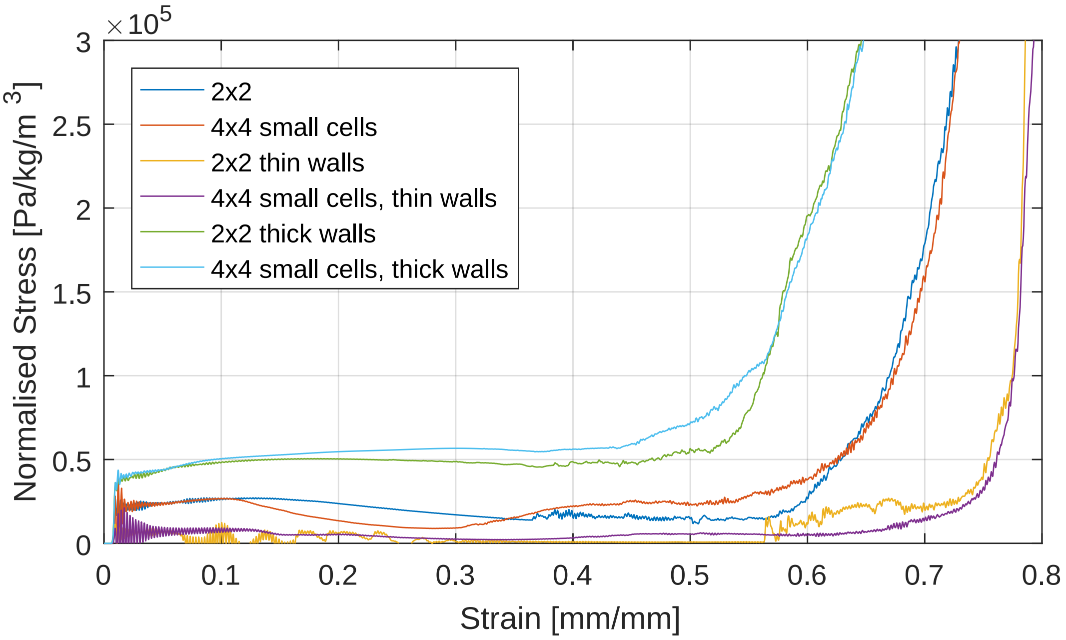

Figure 5.9: *The stress-strain curve of figure 5.8(g) normalized with respect to density. The same tendencies as without the normalisation are seen.*

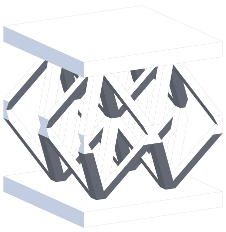

(a) 2x2 structure, standard.
$\rho/\rho_s = 0{,}242$

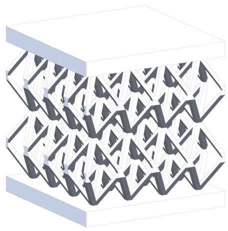

(b) 4x4 structure, standard.
$\rho/\rho_s = 0{,}242$

(c) 2x2 structure, thin.
$\rho/\rho_s = 0{,}200$

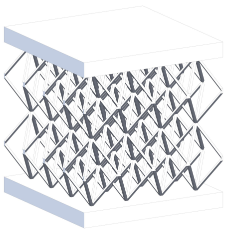

(d) 4x4 structure, thin.
$\rho/\rho_s = 0{,}200$

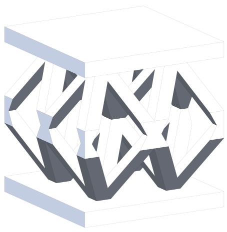

(e) 2x2 structure, thick.
$\rho/\rho_s = 0{,}298$

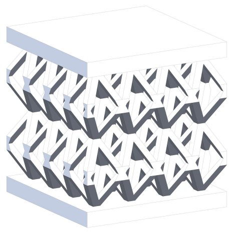

(f) 4x4 structure, thick.
$\rho/\rho_s = 0{,}298$

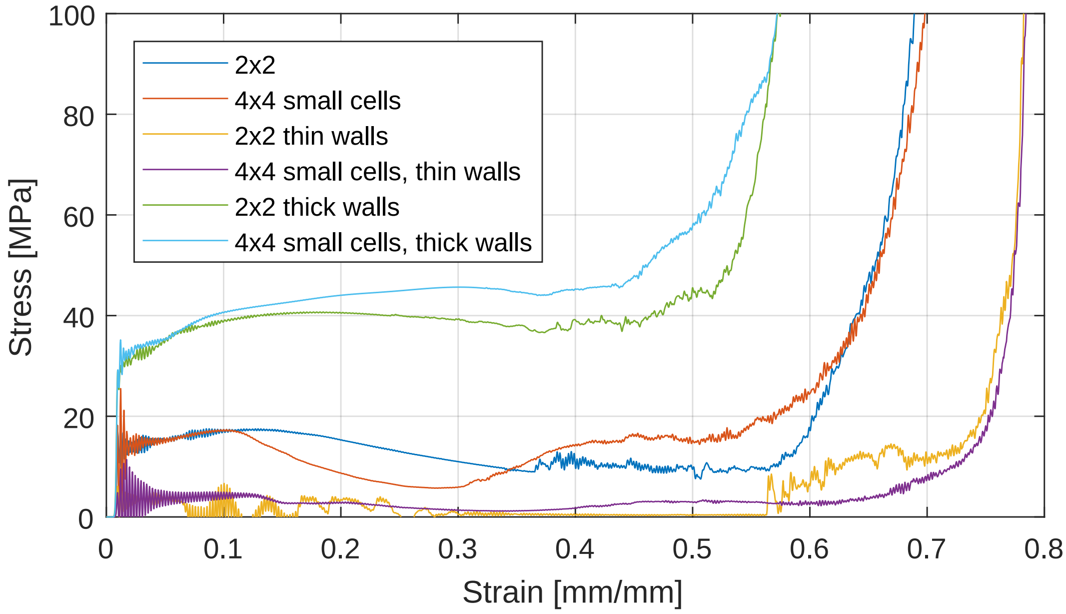

(g) Stress-strain curve for the three pair of cases of thickness and cell size. The plateau stress of the '2x2 thin' version is 0,4 MPa.

Figure 5.8: *Comparison of geometry effect on the micro-truss core structure.*

It was mentioned earlier, how the boundary conditions of the simulations are applied. An attempt is made to loosen this boundary or symmetry condition and investigate the effects of doing this. It should be noted however, that the project group assess that using the boundary conditions is the closest resemblance of the actual case. Unfortunately, it has been impossible to determine which of the boundary condition that is the most correct option as experiments have not been performed. The effect of the stress-strain curve is shown in figure 5.10 where an unfortunate significant difference is seen.

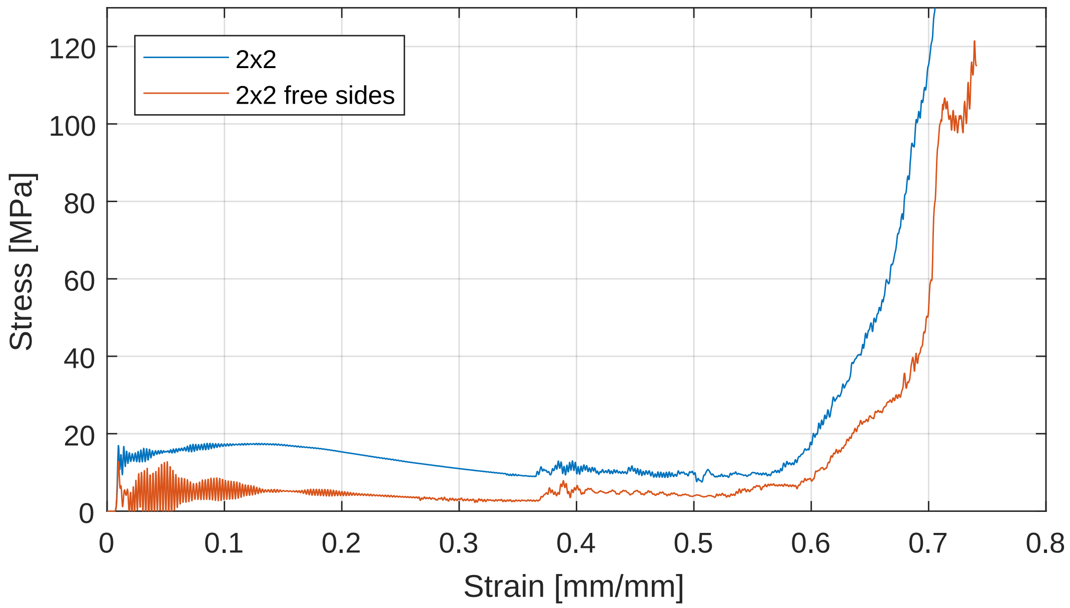

Figure 5.10: *Comparison of the effect of the boundary condition on the stress strain curve for the simulations on the micro-truss cores.*

The deformation of the micro-truss core happens as shown in figure 5.11 for the 4x4 thin structure. The deformation propagates through the core layerwise, which is similar to the densification front for the metallic foam.

5.3.2 Tetrahedral truss core structure as an alternative

Investigations of the statics of respectively a tetrahedral and pyramidal core are conducted in [Deshpande and Fleck, 2001]. This study shows, that there is no difference in strength and stiffness in the normal direction between the two core geometries. The only difference is, that the pyramidal core shows a greater degree of anisotropy in shear strength, [Deshpande and Fleck, 2001], why a pyramidal truss core structure is maintained. Furthermore, the study showed that an inclination of the trusses of 45° maximises the shear strength and stiffness whereas the normal stiffness and strength of course is maximised at an inclination of 90°. The current configuration has an inclination of 50° which offers a good compromise between normal compression and shear strength.

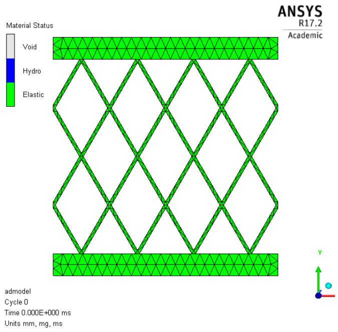

(a) 0 ms.

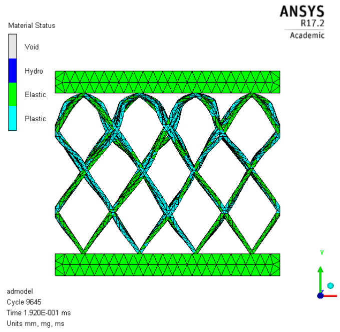

(b) 0,192 ms.

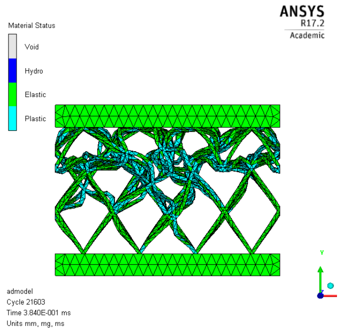

(c) 0,384 ms.

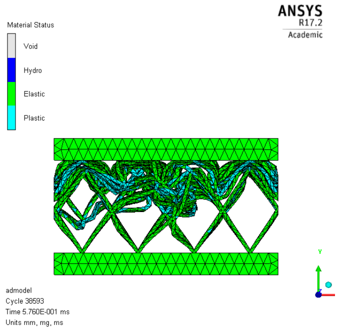

(d) 0,576 ms.

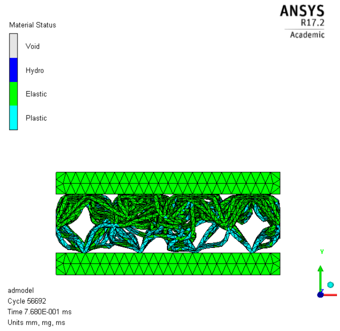

(e) 0,768 ms.

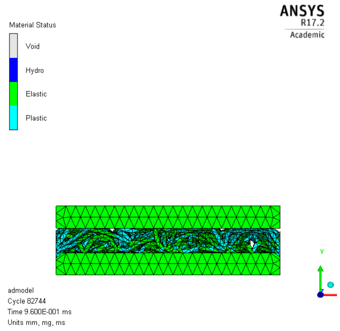

(f) 0,960 ms.

Figure 5.11: *Propagation of the deformation front by layerwise plastic buckling in the micro-truss core structure. Simulation performed on the 4×4 thin structure. Boundary condition is set to strict, i.e. no outwards movement of the side nodes.*

5.3.3 Summary of micro-truss study

The study of the micro-truss structure is summarised in the following section.

- There is good correlation between experimental data and numerical data for the metallic foam. It is therefore decided, that an approach utilising only a numerical study of the micro-trusses is sufficient.

- The micro-truss core shows a varying degree of softening in the second region, i.e. the plateau region. This is due to the forming of a hinge or plastic buckling of the trusses. It seems to be a general observation in all the simulated models but it is indecisive how to remove this effect as introduction of e.g. smaller cells yields varying results, see figure 5.8. This observation is the opposite of the metallic foam in which a slight hardening during region 2 is noticed.

- It is in these studies noticed, that the micro-truss structure, like the metallic foam, appears to be strain rate independent. Granted, a broad study of this phenomena has been neglected, and a definitive conclusion is therefore premature.

- The plateau region, i.e. region 2, is extendable by increasing the quantity of layers, i.e. increasing the thickness of the core, figure 5.7.

- It is possible to achieve a similar response by increasing/decreasing the thickness of the trusses in the core. However, this also influence the plateau strength of the core in upward or downwards direction respectively, i.e. there is a great dependency of the response on the relative density

- The material parameters for the 2x2 thin thickness micro-structure is shown in table 5.2, and a direct comparison with the foam (experimental data) is also shown in this table as the densities are close. However, the micro-truss structure is highly configurable, as shown in the previous section

Material parameter	**Designation**	**Value μ-truss**	**Value foam**			
Density of plate	$\rho_{\mu-truss}$	539	458			kg/m^3
Relative density	ρ_μ/ρ_s	0,200	0,172			$--$
Modulus of elasticity	E	419	336	$\pm$	48,8	MPa
Densification strain	ε_D	0,75	0,480	$\pm$	0,0504	$--$
Plateau strength	σ_{pl}	3,16	4,77	$\pm$	2,18	MPa
Strain energy density	u	2,28	2,19	$\pm$	0,573	MJ/m^3
Specific strain energy	e	4229	4737	$\pm$	1324	J/kg

Table 5.2: *Comparison of the numerical obtained data for the micro-truss structure; 2x2 thin thickness configuration, against the material parameters for the aluminium foam plate from experimental data. See appendix C for the material test.*

Finally, the manufacturing method used might entail different failure modes. In the cases studied above the manufacturing method is expected to be extrusion followed by wire electric discharge machining transverse to the extrusion direction. This entail no significant weaknesses in the interface of the truss and face-sheet, but is a costly manufacturing method. Another manufacturing method is perforation of a plate, followed by a folding of the perforated plate into the desired pyramidal geometry. The layers and face-sheet are thereafter connected by brazing. This is a cheaper method, but in some cases entail failures in the nodes instead of buckling, [Queheillalt et al., 2008].

6 | Analytical study

This chapter includes an analytical study for deformation of the metallic foam under blast load. Parameters influencing the total capacity of energy absorption of the protective plate are also investigated with the objective of enhancing the understanding of the governing parameters. The analysis is divided into two steps. For the first; two analytical approaches for the response of the protective plate under uniform blast loading are presented. For the second; the response of a protective plate under spherical blast loading is investigated. Furthermore, a comparison of the results with numerical simulations, comments and observations are presented.

6.1 Response of a protective plate subjected to a uniform blast load

Analysis of metal foam response under blast load can be divided into two approaches [Zhou et al., 2015]. The first, the target is assumed at a sufficient distance from the explosion where the blast load is considered uniformly applied to the target plate. As a consequence, the response is one dimensional and the front panel doesn't deform or dissipate any energy. This approach is investigated in subsequent sections. The second, the target is close to the detonation point and the blast load is distributed exponentially over the target plate as can be seen subsequently. This distribution requires a deformation of the front panel where the deformation profile is similar to the load profile and thereby, energy dissipated by the front panel deformation must be accounted for as explained later in section 6.3.

For the first case, where the protective plate consists of a metallic foam covered by a metallic front panel figure 6.1, the optimal thickness of the foam and the front panel can be found [Ashby et al., 2000].

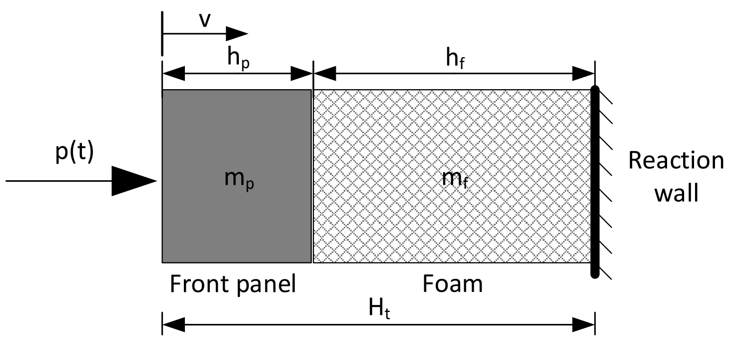

Figure 6.1: *1D model system of foam plate with front panel subjected to a blast load. The plate is of total thickness H_t, cross-sectional area A. The initial velocity of the front panel is given by v.*

A blast imparts an impulse i per unit area as given in eq. 1.2. Assuming that the front panel of density ρ_p and thickness h_p accelerates from zero velocity to v instantaneously where the specific impulse i imparts a momentum M_p for a unit area of the front panel

$$M_p = \rho_p \, h_p \, v = i \tag{6.1}$$

This initial velocity means an initial specific kinetic energy e_s [J/m^2] of the front panel

$$e_s = \frac{1}{2} \rho_p \, h_p \, v^2 = \frac{i^2}{2 \, \rho_p \, h_p} \tag{6.2}$$

This energy must be dissipated by the foam. Assuming w_v is the energy dissipated by a full densification of a unit volume of the foam and h_f is the thickness of the foam, it can be written

$$e_s = w_v \, h_f \qquad \Rightarrow h_f = \frac{i^2}{2 \, \rho_p \, h_p \, w_v} = \frac{D}{\varepsilon_D} \tag{6.3}$$

this yields the deformation of the foam for given impulse

$$D = \frac{i^2}{2 \, \rho_p \, h_p \, \sigma_{pl}} \tag{6.4}$$

where $w_v \approx \sigma_{pl} \; \varepsilon_D$ is the area under the stress-strain curve, see figure 5.3(b), D is the deformation distance the front panel crosses and ε_D is the densification strain of the foam. It is assumed here that the pressure is uniform at the front panel, this is sufficient when the target is far enough from the explosive point, thus, no energy consumption by bending or membrane of the front panel is considered in this discussion.

For most design cases, reducing the total mass is the most important task where the mass for a unit area on the protective plate m_t is the sum of the front panel mass m_p and the foam mass m_f per unit area

$$m_t = m_p + m_f = \rho_p \, h_p + \frac{\rho_f \, i^2}{2 \; \rho_p \, h_p \, w_v} \tag{6.5}$$

and minimizing the mass m_t with respect to the front panel mass m_p leads to $m_p = m_f$.

It means that for the best design (minimum mass) the foam and front panel must be equal in mass, and hereby the thickness of the front panel is simply related to the foam thickness as

$$h_p = \frac{\rho_f}{\rho_p} \, h_f \tag{6.6}$$

and the total mass per unit area can be written as

$$m_t = 2 \; m_f = i \sqrt{\frac{2 \; \rho_f}{w_v}} \tag{6.7}$$

The above discussion quickly shows the minimum mass of the plate to absorb the kinetic energy imparted in the front plate by the impulse of the blast wave and can be used for a quick estimate of the necessary foam thickness for blast applications. On the other hand, the total thickness of the protective plate is

$$H_t = h_p + h_f = h_p + \frac{i^2}{2\,\rho_p\,h_p\,w_v} \tag{6.8}$$

Minimizing the total thickness H_t with respect to the front panel thickness h_p leads to $h_p = h_f$. This can be applied for the cases where the size is more important than the weight of the protective panel.

6.1.1 Another approach for a response of aluminium foam bar

The model above describes the deformation based on kinetic energy saved in the front panel neglecting the effect of the densified foam inertia during deformation. This effect can be significant especially for thin or even no front panel where the kinetic energy has to be transferred to this densified layer of the foam.

This model is based on the work in [Hanssen et al., 2002] for determining the one-dimensional deformation in an aluminium foam bar under the assumption of a linearly decaying blast load. The model is summarized here and explained in details in appendix D. This model accounts for the increase in mass at the proximal end during the deformation process. The model is shown in figure 6.2 and consists of a foam bar covered by a front panel of mass m_p and area A loaded by a blast loading $p(t)$ while it is fixed to a rigid wall in the distal end.

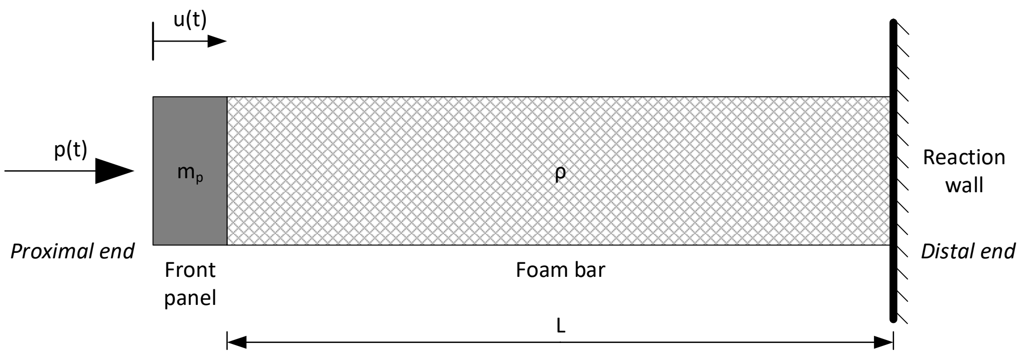

Figure 6.2: *1D model system of foam bar with front panel subjected to a blast load. The bar is of length L, cross-sectional area A and mass $m_f = \rho\,A\,L$. The deformation of the bar is given by $u(t)$. [Hanssen et al., 2002].*

In figure 6.3 the model system at time t and $t + dt$ is shown. The foam bar starts deforming in the loaded end/proximal end, and a densification front moves through the material resulting in the left part of the foam becoming completely densified achieving the same velocity as the rigid front panel, whereas the remaining right part is not affected by this deformation, [Hanssen et al., 2002].

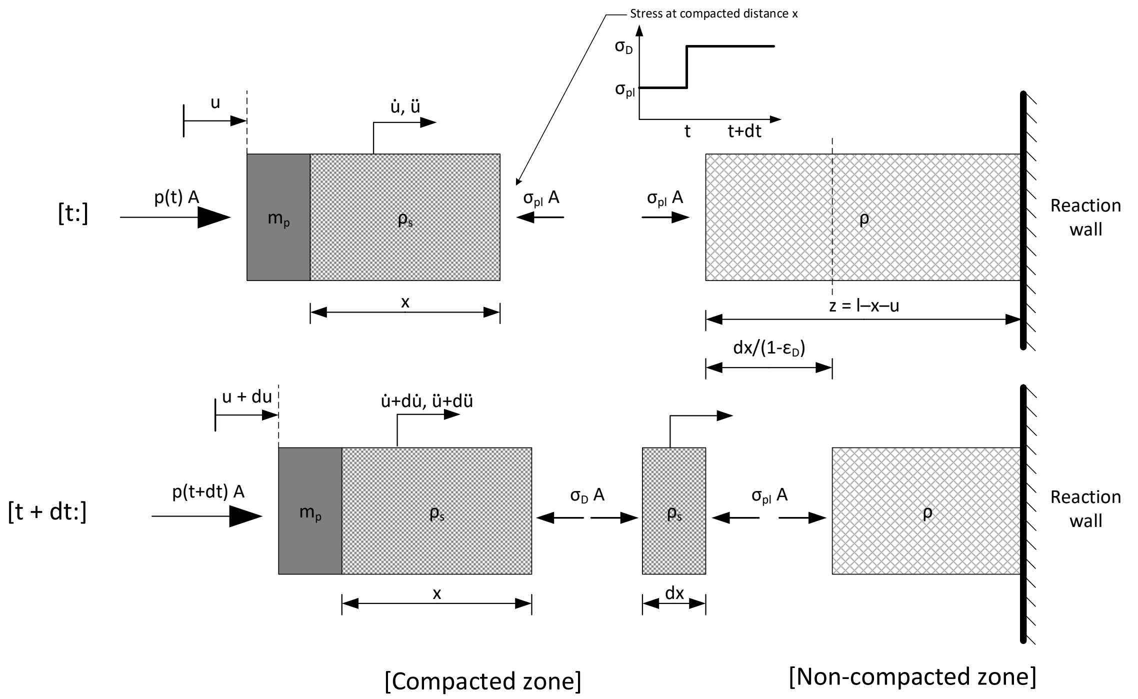

Figure 6.3: *FBD at time t and $t + dt$. [Hanssen et al., 2002].*

Using conservation of mass, and the size of the compacted zone x, and the displacement of the front panel u for time t is

$$u = \frac{\varepsilon_D}{1 - \varepsilon_D}\, x \tag{6.9}$$

In the time interval of t to $t + dt$, the impulse from the forces has to equal the change in momentum of the element, [Hanssen et al., 2002].

$$\rho_s\, A\, dx\, (\dot{u} + d\dot{u}) = (\sigma_D - \sigma_{pl})\, A\, dt \tag{6.10}$$

Assuming that the second order term $dx\, d\dot{u}$ is negligible, then by dividing with dt and taking the limit $dt \to 0$

$$\sigma_D = \sigma_{pl} + \frac{\rho}{1 - \varepsilon_D}\, \dot{x}\, \dot{u} \qquad \text{note } \rho_s = \frac{\rho}{1 - \varepsilon_D} \tag{6.11}$$

Similarly, the conservation of momentum (Newton 2nd) for the front panel and compacted region (rigid body) to the left of the element dx gives

$$\left[m_p + \frac{\rho\, A}{1 - \varepsilon_D}\, x\right]\, \ddot{u} + (\sigma_D - p(t))\; A = 0 \tag{6.12}$$

By combining eqs. 6.9, 6.11 and 6.12, a single differential equation is obtained

$$\left[1 + \frac{\rho\, A}{m_p\, \varepsilon_D}\, u\right]\, \ddot{u} + \frac{\rho\, A}{m_p\, \varepsilon_D}\, \dot{u}^2 + (\sigma_{pl} - p(t))\, \frac{A}{m_p} = 0 \tag{6.13}$$

which is a second order differential equation and its solution, see appendix D, for the proper boundary conditions yields

$$D_a \geq \frac{I^2}{(\rho\, L + 2\, \rho_p\, h_p)\, p_0} \left(\frac{p_0}{\sigma_{pl}} - \frac{4}{3} \right), \qquad \frac{p_0}{\sigma_{pl}} > 2 \tag{6.14}$$

which can be written as

$$b_1\, {D_a}^2 + b_2\, D_a + b_3 = 0 \tag{6.15}$$

where

$$\begin{aligned} b_1 &= \frac{\rho}{\varepsilon_D} \\ b_2 &= 2\, \rho_p\, h_p \\ b_3 &= -\frac{I^2}{P_0} \left(\frac{P_0}{\sigma_{pl}} - \frac{4}{3} \right) \end{aligned}$$

where $D_a = L\, \varepsilon_D$ is the deformation of the foam bar, I is the reflected impulse in Pa s, ρ_p, h_p are the density and thickness of the front panel respectively and p_0 is the peak pressure.

The main difference between eq. 6.4 and eq. 6.15 is that the first one doesn't account for the inertia of the foam during deformation. The result of a numerical simulation of the same case is plotted together with the results obtained by the two different approaches in figure 6.4. It can be seen that [Ashby et al., 2000] overestimates the deformation of the foam as the mass of the foam and its inertia is absent from the eq. 6.4.

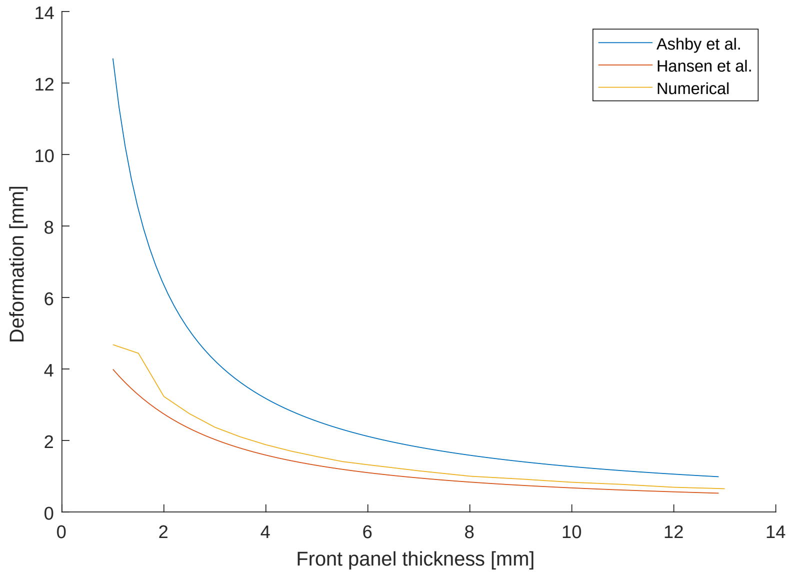

Figure 6.4: *Deformations obtained numerically and by eqs. 6.4 and 6.15 for different front panel thicknesses. The peak pressure* $p_r = 13{,}7$ MPa *and the panel density* $\rho_p = 2700$ kg/m^3.

For a relatively large front panel mass, the densified foam mass has less influence on the results where the panel mass is dominant and the results of the two approaches seem to converge towards the numerical solution as $h_p \longrightarrow \infty$. On the other hand, for a thinner front panel where the mass becomes small and the influence of the foam mass becomes very noticed, the results become quite different and eq. 6.4 seems to overestimate the deformation.

For a foam plate without a face sheet, eq. 6.4 cannot be used while eq. 6.15 is still able to yield the deformation of the foam. However, both methods are only applicable for a uniform loading case, why a model for the plate-response under a non-uniform distributed load is investigated next.

6.2 Response of a target plate subjected to a spherical blast load

The solutions described above can be used to calculate the minimum length/deformation of a foam plate or bar covered by a front panel only when the load can be assumed uniform. In this section the distribution of the load produced by relatively close range burst is considered. Thereby, the shape and depth of deformations over the protective plate are considered based on energy methods.

A structure can be disturbed from its normal position of static equilibrium by giving it an initial displacement or initial velocity. The structure vibrates with a period of oscillation dependent on its mass and a factor characterizing the resistance that the structure develops. For an elastic structure, this resistance is characterised by a stiffness of a spring. The amount of damping determines the amplitude of vibration. An initial velocity can be derived from an impulse applied to the structure [Smith and Hetherington, 1994]. When a structure is forced to vibrate by the application of a time dependent loading, the response is termed *forced* vibration. A forcing function representing the blast load exciting the structure can be found from the triangular load pulse as shown in figure 6.5 where t_0 is the positive phase duration of the blast wave which produces a peak force on the structure F. Any impulse causes an increment in velocity of the system, in accordance with Newton's second law, which states that an impulse I produces a change in momentum. Thus

$$velocity\ change = \frac{force \times time}{mass}$$

Thus, the forces acting on a structure associated with a plane shock wave are dependent upon the impulse of the incident shock pressure where the force acting on any finite element of the structure is a function of the impulse acting on that element.

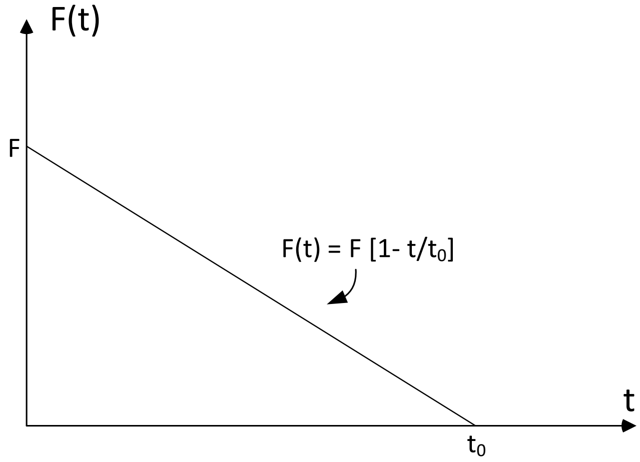

Figure 6.5: *Idealised blast load pulse [Smith and Hetherington, 1994].*

6.2.1 Deformation Profile

A target plate consisting of a metallic foam, with or without a thin face sheet, undergoes plastic deformation when exposed to a blast wave producing a peak pressure higher than the strength of the foam material, i.e. the plateau stress. For a fully supported plate the deformation profile must be similar to the load profile as in figure 6.6. The pressure-time curve for a point of the target differs from that of another point located at a different distance from the detonation point. Besides this, the duration of the positive phase and thereby the impulse acting on the target plate is a spatial function, see appendix B.

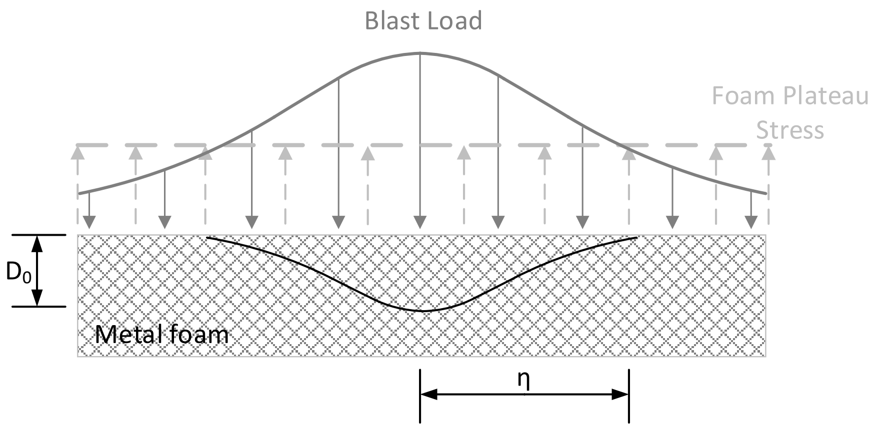

Figure 6.6: *Load and deformation profile of a metallic foam exposed to a blast load.* D_0 *is the maximum depth of the bulge and* η *is the radius of the bulge. Modified from [Zhou et al., 2015].*

As the blast load lasts for an extremely short duration, typically from several microseconds to 1 ms, it is often simplified as a triangular load with zero rise time [Smith and Hetherington, 1994]. By using the equivalent triangular reflected pressure shown in figure 4.4, which indicates that the reflected pressure is maximum at $t = 0$ and zero at $t = {t_0}'$, the reflected pressure at any point of the target is

$$p_r(t) = p_{r\alpha}\left(1 - \frac{t}{{t_0}'}\right) \tag{6.16}$$

where $p_{r\alpha}$ is the peak reflected pressure at the point of interest which has an incidence angle α. It must be noted that the equivalent triangular pressure depends on the impulse at the considered point which means that the equivalent positive time ${t_0}'$ has different values for the different points.

A spatial function describing the impulse at any point can be approximated based on the distribution shape of the impulse which is, sometimes, similar to a bell function and thereby can be fitted to a Gaussian function [Zhou et al., 2015].

$$I_r(r) = I_r(0)\, e^{-\frac{r^2}{2\,{C_1}^2}} \tag{6.17}$$

where $I_r(0)$ is the impulse value at the bulge center and C_1 is the characteristic size of the blast loading area, following the standard deviation of the data – where the function value becomes 1% of its peak value at the point $r = 3\,C_1$ – which can be found from the data obtained in section 4.5, r is the radius of a circle that concentric with the bulge area exposed to the blast and $I_r(r)$ is the reflected impulse at distance r from the center. The deformed area is defined by the reflected pressure and the total resistance of the target plate R_t. This resistance consists of the plateau stress, the inertia of the front plate, bending resistance of the front plate and the membrane resistance of the front plate.

The plate undergoes a plastic deformation as long as the peak reflected pressure is higher than the total resistance of the target plate.

6.2.2 Determination of the bulge profile for a protective plate

For a metallic foam with a very thin face sheet(skin), as the aluminium foam used in this study, the only resistance to deformation comes by the plateau stress of the foam, where bending and membrane forces are too small in this case and therefore neglected.
At some distance η from the bulge center the reflected pressure is equal to the plateau stress and no deformation occurs after this point, see figure 6.7. As the reflected pressure still has a value outside the area defined by η, although this value is less than the plateau stress, it causes an impulse which gives an initial velocity to the face sheet. This initial velocity for all points outside the bulge area is not enough to produce a plastic deformation in the foam. When applying an energy method for obtaining deformations, only plastic deformations are considered as seen subsequently.

The distribution of the reflected peak pressure can also be approximated as a Gaussian function where it is rewritten as

$$p_{r\alpha} = p_{r0}\ e^{-\frac{r^2}{2\,{C_1}^2}} \tag{6.18}$$

where p_{r0} is the peak reflected pressure at zero angle of incidence, C_1 is the characteristic size of the deformed area as defined earlier, the data obtained in section 4.5 can be used to find the radius r for any value of $p_{r\alpha}$ and thereby C_1 can be determined. Note that the characteristic size C_1 is assumed identical in both impulse and pressure functions which is not the case for the whole set of data, but within the bulge area it is found to be a reasonable approximation.

Equating the plateau stress with eq. 6.18 yields η, i.e the bulge radius

$$p_{r\alpha} = \sigma_{pl} \qquad\qquad \Rightarrow \eta = C_1\sqrt{2\ \ln\frac{p_{r0}}{\sigma_{pl}}} \tag{6.19}$$

It can be seen that the area outside a circle of radius η and center at the closest point to the detonation point remains undeformed, see figure 6.7.

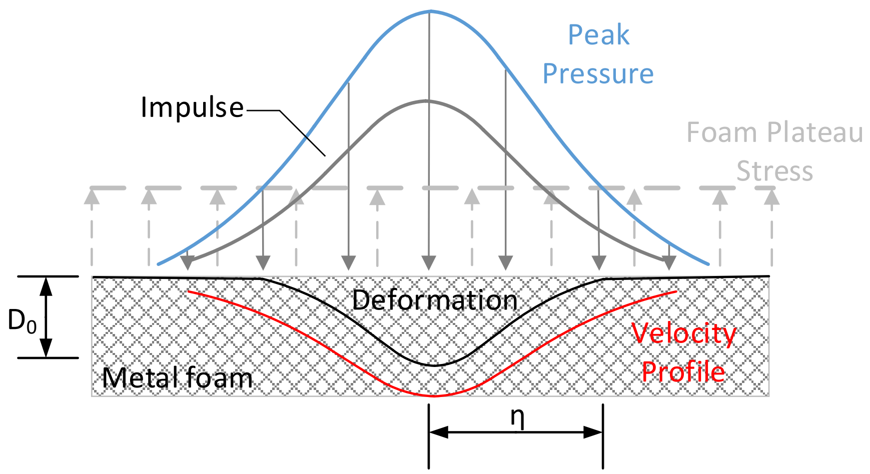

Figure 6.7: *Pressure, Impulse, Velocity and Deformation Profiles of a metallic foam with thin face sheet exposed to a Blast load, D_0 is the maximum depth of the bulge and η is the radius of the bulge. Modified from [Zhou et al., 2015].*

Each point within the deformed area of the target plate is subjected to an impulse which, if assumed that this impulse is imparted onto the face sheet before deformation starts, gives this point an initial velocity v_0 before deformation starts and comes to rest - by the action of the net forces as Newton second law states - when deformation ends. This initial velocity differs from one point to another as the impulse does.

For a bulge area A with radius r and velocity field $v_0(r)$ the momentum M_A over the entire area can be obtained

$$M_A = \int_A \rho_p \, h_p \, v_0(r) \, dA \tag{6.20}$$

where ρ_p and h_p are the density and thickness of the face sheet respectively. This equation gives the momentum for the face sheet assuming that the impulse produced by the blast is converted into a momentum saved in the face sheet. The total impulse the bulge area A is subjected to can be obtained by integrating eq. 6.17 over the area

$$I_A = \int_A I_r(r) \, dA \tag{6.21}$$

Equating eqs. 6.20 and 6.21 yields the velocity as a function of r

$$v(r) = \frac{I_r(r)}{\rho_p \, h_p} = \frac{I_r(0)}{\rho_p \, h_p} \, e^{-\frac{r^2}{2\,{C_1}^2}} = v_0(0) \, e^{-\frac{r^2}{2\,{C_1}^2}} \tag{6.22}$$

This equation shows that the initial velocity of the bulge center can be reduced by increasing the face sheet density and/or thickness. It is seen from eq. 6.22 that the velocity has the same characteristic size C_1 but peak value.

The total kinetic energy E_k carried by the bulge area of the face sheet is the summation of kinetic energies of all material points of the bulge area where

$$E_k = \int_A \frac{1}{2} \, \rho_p \, h_p \, {v_0}^2(r) \, dA = \frac{\pi \, [I_r(0)]^2 \, {C_1}^2}{2 \, \rho_p \, h_p} \left(1 - \frac{{\sigma_{pl}}^2}{{p_{r0}}^2}\right) \tag{6.23}$$

whee $A = \pi \, \eta^2$ is the bulge area.

The metallic foam has to dissipate this kinetic energy during its plastic deformation where the energy absorbed by the plastic deformation of the front panel is neglected in this section.

To obtain the deformation profile at any point of the plate, it is assumed that the work done by the resistance of the foam within the bulge area is equal to the kinetic energy carried by the bulge area. At the bulge edge, the peak reflected pressure is equal to the plateau stress. Thus, no deformation occurs after that point. It can be assumed that the deformation function has the general form

$$D(r) = D_0 \, e^{-\frac{r^2}{2\,{C_2}^2}} \tag{6.24}$$

where $C_2 = \eta/3$ is the characteristic size of the function. At the bulge edge where $r = \eta$, the deformation is equal to 1% of the peak deformation value and thereby neglected.

Hence, the work done by the foam resistance is

$$W = \int_A \sigma_{pl}\, D_r\, dA = 2\,\pi\,\sigma_{pl}\, D_0\, {C_2}^2 \tag{6.25}$$

equating eqs. 6.23 and 6.25 yields the peak deformation value at the bulge centre

$$D_0 = \frac{[I_r(0)]^2\, {C_1}^2}{4\,\sigma_{pl}\,\rho_p\, h_p\, {C_2}^2} \left(1 - \frac{{\sigma_{pl}}^2}{{p_{r0}}^2}\right) \tag{6.26}$$

and the minimum foam thickness needed at the bulge centre is

$$h_f \geq \frac{D_0}{\varepsilon_D} \tag{6.27}$$

It is clear from eq. 6.26 that increasing the plateau stress, the face sheet density and/or the face sheet thickness decreases the maximum deformation at the bulge center. This also increases the weight of the plate which is not desired. Increasing the front panel thickness and/or density leads to less foam thickness h_f and mass m_f. The relation between the front plate thickness and the total thickness, for $W = 0{,}1175$ kg TNT and $R = 0{,}5$ m, is shown in figure 6.8(a) and the detailed results are listed in table 6.1.

Case		**Minimum Mass**	**Minimum Thickness**
Maximum deformation	[mm]	7,7	3,1
Panel thickness	[mm]	2,6	6,5
Foam thickness	[mm]	16	6,4
Total thichness	[mm]	18,6	12,9
Panel mass	[kg/m^2]	7,03	17,55
Foam mass	[kg/m^2]	7,32	2,93
Total mass	[kg/m^2]	14,35	20,48

Table 6.1: *Minimum values and associated thicknesses and masses of the protective plate. The results obtained by eq. 6.26. The explosive charge weight $W = 0{,}1175$ kg, the range $R = 0{,}5$ m, the front panel density $\rho_p = 2700\ \mathrm{kg/m^3}$, the foam density $\rho_f = 458\ \mathrm{kg/m^3}$,the peak reflected impulse at the bulge center $I_0 = 421{,}5\ \mathrm{Pa\ s}$ and the plateau stress $\sigma_{pl} = 4{,}77$ MPa.*

It can be seen from table 6.1 that the total mass at the minimum point converges to distribute equally between the foam and the front panel, $m_p = m_f$ which is consistent with the result found in section 6, the same result is found for the minimum thickness as well where the two thicknesses become equal at the minimum thickness of the plate, see figure 6.8(a). However, a design point can be found between these two optimum points by weighting the two functions.

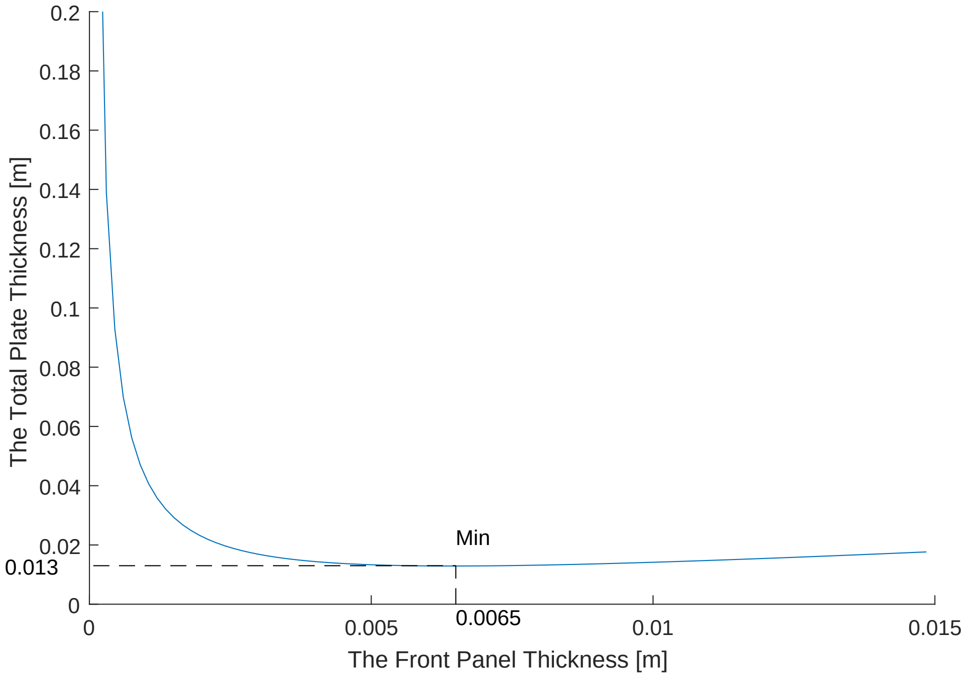

(a) The minimum total thickness of the plate

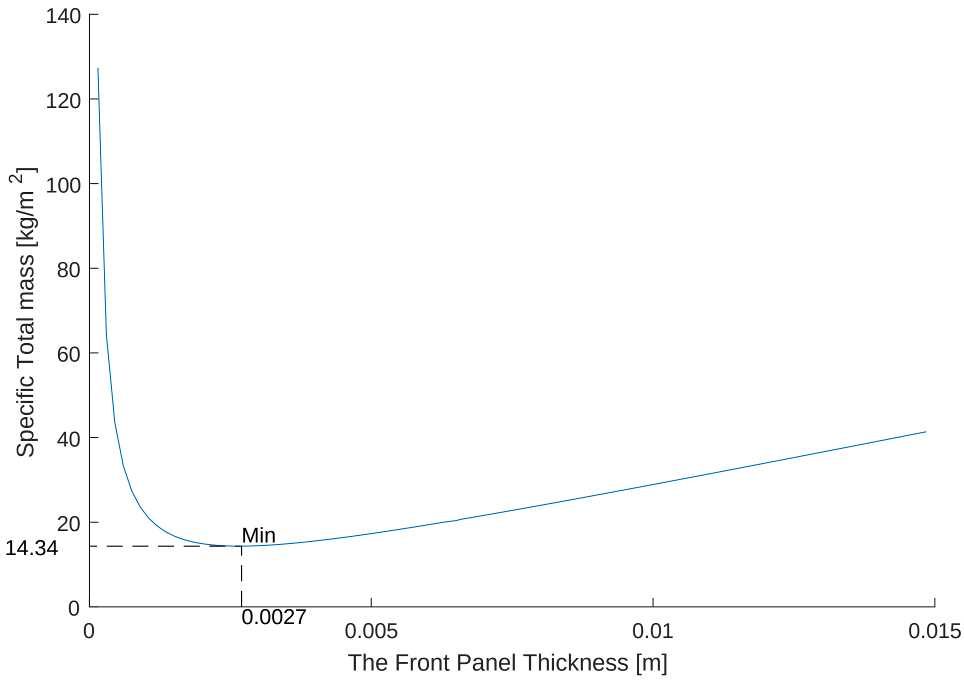

(b) The minimum total mass of the plate

Figure 6.8: *The optimum values of the protective plate, the charge weight* $W = 0{,}1175$ *kg and the range* $R = 0{,}5$ *m: (a) The total specific mass* $m_t = 20{,}48$ kg/m^2 *when the thickness is minimum. (b) The total thickness* $H_t = 18{,}6$ *mm when the mass is minimum.*

6.3 Bending and membrane energy

The results obtained above contain a relatively thick front panel, around half the total thickness, where the maximum deformation at the bulge center is $D_0 = h_f \, \varepsilon_D$. Figure 6.8 shows that the deformation of the front panel is equal to half its thickness and approximately three times the thickness for minimum thickness and minimum mass respectively. The bulging process is thereby governed by the membrane forces and the contribution from bending can be neglected [Goel et al., 2013]. Thus, including the membrane energy yields even lighter and/or thinner protective plate than the results shown in figure 6.8.

The plastic strain energy for large deformation of a rigid plastic membrane with an axissymmetrical bulging is given in [Teeling-Smith and Nurick, 1991] as

$$E_d = \pi \, h_p \int_0^{\eta} \frac{Y_D}{(1-\nu-\nu^2)^{\frac{1}{2}}} \left(\frac{\partial D}{\partial r}\right)^2 r \, dr \tag{6.28}$$

where Y_D is the dynamic yield stress for the front panel material, ν is Poisson's ratio for the panel and D is the deformation profile defined by eq. 6.24.

At time $t = 0$ before deformation starts, the initial velocity of the front panel is a spatial function defined by eq. 6.22. At time $t = t_1 < t_m$, the deformation at the bulge center is assumed to be x_0 and the spatial deformation function $x(r)$ is similar to eq. 6.24, the deformation velocity at the bulge center is a function of deformation distance $v_D = f(x)$.
The front panel decelerates from $v = v_0$ at $t = 0$ to $v = v_D$ at $t = t_1$. Assuming that the deformation velocity is a linear function of the deformation distance yields

$$v_D(r) = -\frac{v_0(r)}{D(r)} \, x(r) + v_0(r) = \left(v_0(0) - \frac{v_0(0)}{D_0} \, x_0\right) e^{-\frac{r^2}{2\,C_1{}^2}} \tag{6.29}$$

where $v_0(r)$ is given in eq. 6.22 hence, the deformation velocity is a two dimensional function.

At maximum deformation $x_0 = D_0$ and the deformation velocity becomes zero over all the bulge area. The work done by the resistance of the plateau stress within the bulge area up to $t = t_1$ is

$$W = \int_A \sigma_{pl} \, x(r) \, dA = 2\,\pi \, \sigma_{pl} \, C_2{}^2 \, x_0 \tag{6.30}$$

At time t_1, the fully densified foam moves with the front panel at the same velocity $v_D(r)$.

A conservation of energy yields

$$E_k = E_d + W + \int_A \frac{1}{2}(\rho_p \, h_p + \rho_f \, x) \, v_D(r)^2 \, dA \tag{6.31}$$

where E_k is the total kinetic energy as given by eq. 6.23.

Substituting eqs. 6.23, 6.28, 6.29 and 6.30 in eq. 6.31 and manipulating the resultant equation yields

$$a\,{D_0}^2 + b\,D_0 + c = 0 \tag{6.32}$$

where

$$a = \frac{h_p\,Y_D}{(1-\nu-\nu^2)^{\frac{1}{2}}}$$
$$b = 4\,\sigma_{pl}\,{C_2}^2$$
$$c = -\rho_p\,h_p\,{C_1}^2\;v_0(0)^2\left(1-\frac{{\sigma_{pl}}^2}{{p_{r0}}^2}\right)$$

The required dynamic yield stress Y_D for the front panel is calculated using an iterative procedure [Teeling-Smith and Nurick, 1991] by

$$\frac{96421{,}8\,I^2}{\sqrt{Y_D}} = 40\left(\frac{Y_D}{\sigma_y}-1\right)^5 \tag{6.33}$$

where I is the impulse imparted onto the front panel and σ_y is the static yield stress of the front panel material. Since I is not constant over the plate, the maximum peak value is used which yields a more conservative results.

Solving eq. 6.32 for different thicknesses of the front panel yields the results listed in table 6.2.

Case		**Minimum Mass**	**Minimum Thickness**
Maximum deformation	[mm]	6,8	2,9
Panel thickness	[mm]	2,5	5,9
Foam thickness	[mm]	14,2	6
Total thichness	[mm]	16,7	11,9
Panel mass	[kg/m^2]	6,75	16,06
Foam mass	[kg/m^2]	6,53	2,74
Total mass	[kg/m^2]	13,28	18,8

Table 6.2: *Minimum values and associated thicknesses and masses of the protective plate. The results obtained by eq. 6.32. The explosive charge weight* $W = 0{,}1175$ kg*, the range* $R = 0{,}5$ m*, the front panel density* $\rho_p = 2700$ kg/m^3*, the foam density* $\rho_f = 458$ kg/m^3*, the peak reflected impulse at the bulge center* $I_0 = 421{,}5$ Pa s *and the plateau stress* $\sigma_{pl} = 4{,}77$ MPa*.*

It is seen by the comparison of results in tables 6.1 and 6.2 that the membrane resistance reduces the minimum weight of the protective plate by 7,5%.

6.4 Comparison and validation of the results

A validation of the analytical work can be done by a comparison with real tests representing the blast load. This kind of experiment is, unfortunately, not possible at the University lab. Alternatively, a comparison with numerical results is shown in this section.

A numerical simulation for a protective plate, consisting of aluminum foam and front panel, fully supported and subjected to a peak reflected pressure and impulse equivalent to the blast load from an explosive charge $W = 0{,}1175$ kg TNT. The main objective is to validate the results obtained by eq. 6.24. The deformation vs. the front panel thickness is plotted in figure 6.9. A clear discrepancy in the results can be seen. It is noticed that the difference decreases as the thickness/mass of the front panel increases. This observation needs a further investigation as follows.

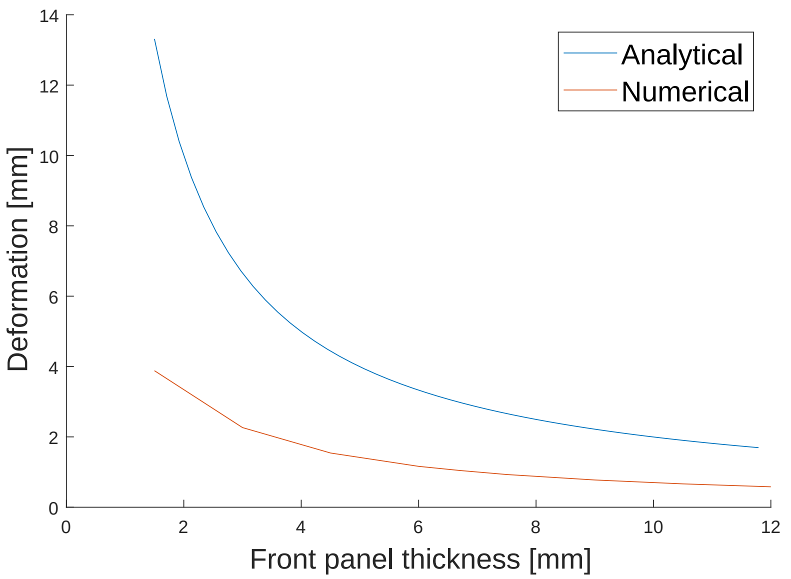

Figure 6.9: *Numerical and analytical results for the deformation vs. front panel thickness of a plate subjected to a peak reflected pressure* $p_r = 7{,}7$ MPa *and reflected impulse* $I_r = 421$ Pa s*, The front panel density* $\rho_p = 2700$ kg/m^3 *and foam material parameters are listed in table 5.1.*

It is assumed in section 6.1 that the deformation doesn't start before the front panel reaches its maximum initial velocity. However, the numerical simulation shows that the deformation starts directly as the blast wave reaches the plate which is more realistic.

For the high pressure design range, figure 1.5, the response time (max deformation time) is much longer than the duration time t_0 and the load is considered impulsive. For low pressure design range, figure 1.6, the load is considered dynamic and thereby the impulsive loading assumption is not valid. Hence, the ratio t_m/t_0 decides how sufficient the assumption is. The structure reaches the maximum deformation after one quarter of the eigenperiod T which means that the duration time must be shorter than one twelfth the eigenperiod. Thereby, an investigation of the ratio t_0/T and its influence on the results is needed.

Assume, that the protective plate system is equivalent to a single degree of freedom mass-spring system loaded by a triangular blast load pulse, as shown in figure 6.10. The mass is equal to the front panel mass and the spring represents the foam stiffness.

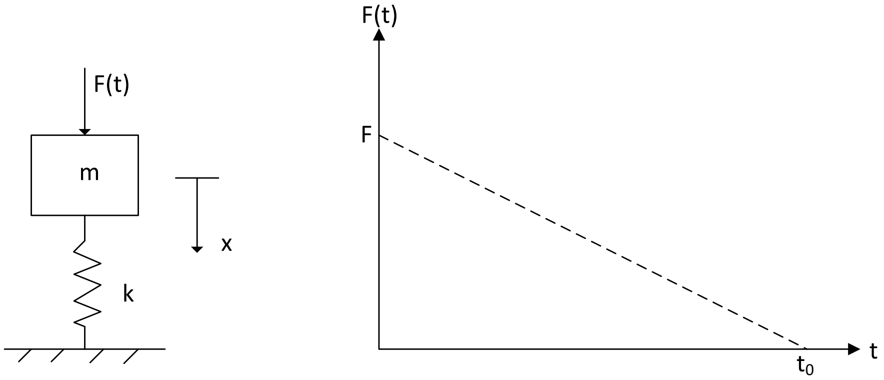

Figure 6.10: *Single degree of freedom system loaded by triangular blast load pulse, [Smith and Hetherington, 1994].*

This blast load can deliver a total impulse I to the target

$$I = \frac{1}{2} F\, t_0 \tag{6.34}$$

The equation of motion for this system is [Smith and Hetherington, 1994]

$$m\, \ddot{x} + k\, x = F \left(1 - \frac{t}{t_0}\right) \tag{6.35}$$

The solution for eq. 6.35 is given in [Smith and Hetherington, 1994] as

$$x(t) = \frac{F}{k\, \omega\, t_0}\; [\sin(\omega\, t_0) - \sin\left(\omega(t - t_0)\right)] - \frac{F}{k}\; \cos(\omega\, t) \tag{6.36}$$

where $\omega = \sqrt{k/m}$ is the radial velocity, m is the mass of the panel, F is the peak load and k is the stiffness of the foam material

$$k = \frac{E\, A}{L} \tag{6.37}$$

where A is the cross section area of the foam and L is the thickness of the foam and E is the modulus of elasticity for the foam material.

The natural response period of the structure with a unit foam thickness is

$$T = \frac{2\, \pi}{\omega} = 2\, \pi \sqrt{\frac{\rho_p\, h_p}{E}} \tag{6.38}$$

where ρ_p and h_p are the density and thickness of the front panel respectively.

Eq. 6.36 can be rewritten as

$$x(t) = x_{st} \left(\frac{T}{2\,\pi\,t_0} \left[\sin(\omega\,t_0) - \sin\left(\omega(t - t_0)\right)\right] - \cos(\omega\,t) \right) \tag{6.39}$$

where $x_{st} = F/k$ is the static displacement produced by the load.

A typical response for two values of t_0/T are compared in figure 6.11. The structure undergoes a number of vibrations while the load is still present for high t_0/T ratio as can be seen from the figure. This situation is categorized as a quasi-static or pressure loading as described in section 1.3. For the low ratio, the loading finishes before the structure completes even a single cycle of response. This is the so called high pressure loading.

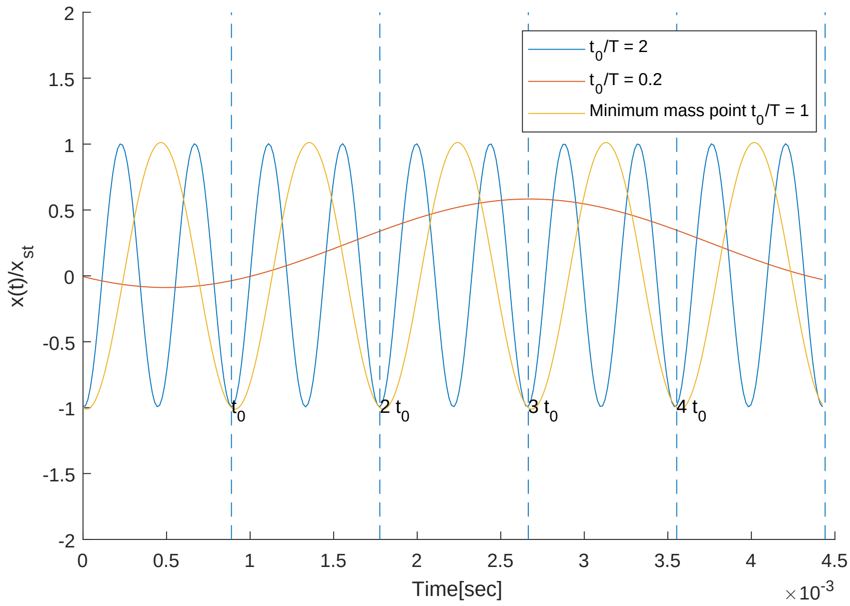

Figure 6.11: *Response of SDOF system to idealize blast loading for two different* t_0/T *ratios and the case of the minimum mass point, for front panel thickness* $h_p = 2{,}5$ *mm. Modified from [Smith and Hetherington, 1994].*

It can be concluded that the ratio t_0/T tells which design range is the closest to the system. For the minimum mass point seen on figure 6.8(b) it is found that $t_0/T \approx 1$. The response curve plotted in figure 6.11 shows that the duration time and response period are approximately equal which means that the maximum deformation time t_m is even shorter than the positive duration time t_0. Thus, this case can't be considered as a high pressure design range, i.e. the design based on impulsive loading overestimates the deformation of the plate.

The ratio between deformation results obtained numerically an analytically D_n/D_0 is plotted against the ratio between the duration time and natural period t_0/T in figure 6.12.

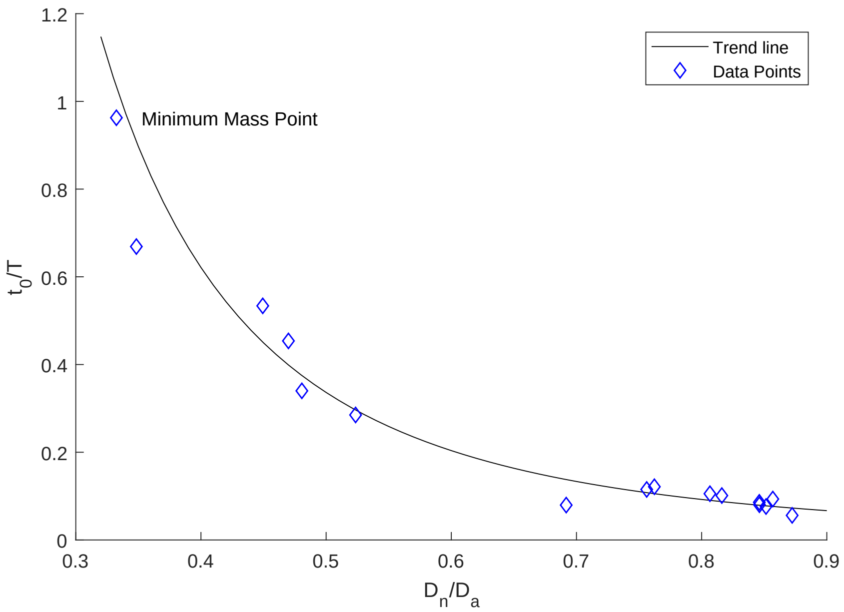

Figure 6.12: *Discrepancy ratio D_n/D_0 vs. time ratio t_0/T. D_0 and D_n are deformation obtained analytically and numerically respectively. The fitting curve is a power function.*

It can be seen from the figure that $D_n/D_0 \longrightarrow 1$ as $t_0/T \longrightarrow 0$. The minimum mass point for the analytical results listed in table 6.1 is shown on figure 6.12. It is seen that the analytical solution overestimates the deformation by a factor of 2,7 relative to the numerical solution why the plate period is almost equal to the positive duration time of the blast load.

6.5 Summary

Analytical model describing the response of a protective plate, foam core and metallic front panel, under blast load are described in the above sections. Some observations are made.

The capacity of energy absorption can be increased by increasing the mass of the front plate, the thickness of the foam, and the plateau stress of the foam. For practical reasons, it is preferred to keep the mass at a minimum why the effect of especially the front plate has to be a compromise. Furthermore, the front plate helps in preventing disintegration of the foam during a blast loading.

The assumption of Gaussian distribution of the data is valid for the area within the bulge, wheres the accuracy of fitted data for some functions decreases as the distance from the bulge center increases. A better fit can be achieved by using second order (two terms) Gaussian function which also increases complexity. It should be noted that for cases where the change in load is less dramatic, more flat curve, the Gaussian function may not be the best choice. However, polynomial, sinusoidal, rational, power functions can also be used.

The bending energy can also be included in the final solution, especially for a thick front panel and relative small deformation.

If the position of the charge relative to the plate is known, the plate can be designed based on the deformation profile, where the thickness of the plate becomes a function of deformation. This reduces the total mass as the maximum thickness is only needed at the bulge center.

The results obtained analytically deviate from the numerical results for high values of t_0/T. Hence, the impulsive loading assumption for high pressure design range must be applied with caution.

7 | Numerical simulations

Numerical simulations by the use of Hydrocode are conducted on various systems. The applied Hydrocode is ANSYS Explicit Dynamics and ANSYS Autodyn where both uses the Autodyn solver. A short description of the methods and some of the material models are found in appendix E. A quick overview and some additional description of relevant behaviour and material models are included here.

7.1 Methods

Multiple methods for solving problems are available in Autodyn. This gives the possibility of choosing the method most suitable for the specific structure/problem.

- Finite element for structural dynamics (Lagrange)
- Finite volume for transient fluid dynamics (Euler)
- Adaptive mesh for structural dynamics with large deformation (ALE)
- Mesh-free particle for large deformation and fragmentation (SPH)

The different methods can be combined so that each part of a system can be simulated using the most suitable method. The current project only makes use of Lagrange and Euler. Euler is used for simulating blast waves and Lagrange for everything else. Lagrange parts can interact with Euler through an Euler-Lagrange coupling. This is achieved by regarding the Lagrange body as a moving boundary for the Euler domain. This results in stress in the Euler material and reactions forces that are applied to the Lagrange part in a feedback system. It is important for Euler-Lagrange coupling that the Lagrange elements are larger than the Euler cells as leakage of material in the Euler domain otherwise may happen. Euler cells should in general be smaller than Lagrange elements to obtain similar accuracy.

7.2 Material models

Materials in hydrocodes consists of multiple parts which can each be one of several different models, all materials contain an equation of state which models the elastic behaviour relating pressure (p), density (ρ) and energy (e). Most material also contain a strength model which models plastic behaviour. Failure is governed by a failure model and can also contain erosion. Autodyn contains multiple different material models of which only a few are relevant for this project. Appendix E contains a description of these but some of the more relevant ones are given here.

7.2.1 Equation of State

Air is described by the use of the ideal gas law under the assumption of perfect gas. This is a simplification but has shown good results and requires few input parameters.

$$p = (\gamma - 1)\,\rho\, e \tag{7.1}$$

where γ is the adiabatic index found as the ratio of specific heat at constant pressure and constant volume, $\gamma = C_p/C_v$.

Explosives such as TNT are modelled with the Jones-Wilkins-Lee (JWL) EOS for rapid expansion of detonation products, it converts to ideal gas EOS at sufficient expansion. The propagation of detonation is controlled by the detonation velocity moving from the detonation point and happens linearly over time. Detonation can also be set to happen instantaneously at the first cycle.

$$p = A\left(1 - \frac{\omega\,\mu}{R_1}\right) e^{-\frac{R_1}{\mu}} + B\left(1 - \frac{\omega\,\mu}{R_2}\right) e^{-\frac{R_2}{\mu}} + \omega\,\rho\, e_0 \tag{7.2}$$

$$\mu = \frac{\rho}{\rho_0} \tag{7.3}$$

where ρ_0 is the reference density, A, B, R_1, R_2 and ω are semi-non-physical constants determined from dynamic experiments.

7.2.2 Strength

The Crushable Foam model is a relatively simple model for modelling the behaviour of porous materials like foams, see figure 7.1. It links the principal stress to the volumetric strain by tabular data. Unloading and reloading is governed by the EOS, usually linear. A built in failure criteria is part of the model, namely a maximum tensile limit.

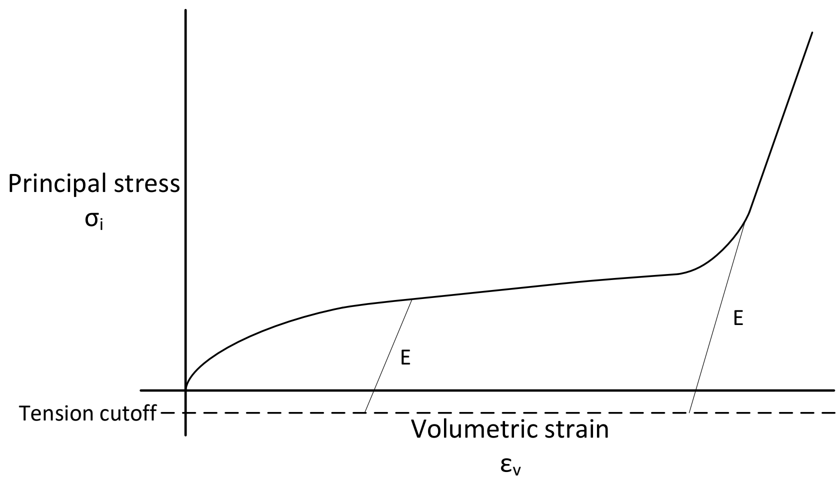

Figure 7.1: *Visualisation of the Crushable Foam model.*

7.3 Considerations when performing hydrocode simulation

When performing a simulation there are a number of options that must be considered to obtain a simulation of sufficient accuracy and reasonable solve time. The solve time is mainly dependent on the smallest element/cell size and number of nodes. Complexity of material models and interactions also effect the solve time. Accuracy is also effected by these parameters, but in the opposite way. Finer mesh means smaller elements/cells and more nodes mean longer solve time, but better accuracy. It should be noted that an academic license is used during the project which limits the number of nodes in a simulation to 32000.

7.3.1 Detonation

Simulation of the effects of explosions and blast loads is often done by simulating the explosion from the initial charge. The charge itself can be modelled in multiple ways but especially two methods are common. Modelling the charge from undetonated explosive to detonation product from a detonation point and propagates from there, or as pure detonation product. The physical difference is that the detonation duration and propagation are included. This may prove important for large volumes and/or special geometries of explosive. The other method simulates the explosive as having detonated instantaneously and completely converted to detonation product. This may save some computation time but this is usually not noticeable compared to the total solve time. The real advantage of the second method is that the charge can be modelled with the ideal gas EOS and thereby make use of a higher order Euler scheme. The disadvantage of using the ideal gas EOS for detonation product instead of e.g. JWL is that the material behaviour may be inaccurate. To investigate this issue a number of simulations are conducted.

Blast model comparison

A simple free-air blast can be considered to be one dimensional. This can easily be modelled in Autodyn with the Euler wedge mesh in axisymmetric conditions. The wedge is modelled with a minimum radius of 1 mm, a maximum radius of 1000 mm and meshed with a cell size of 1 mm, the angle is controlled by the program (10°). A flow out boundary condition is put at the outer end and gauges are placed at an interval of 100 mm from the centre, see figure 7.2.

Two simulations are conducted with this setup, one with the TNT from the material library (JWL EOS) with a detonation progressing from the centre and one with the Air from the material library (Ideal Gas EOS) modified with the density and internal energy of TNT detonation product. The amount of explosive for the simulation is set to 0,5 kg. As the wedge has a minimum radius the outer radius of the charge is determined from

$$V = \frac{4}{3}\pi\,(R-r)^3 \tag{7.4}$$

where r is the minimum radius, here set to 1 mm for convenience, V being the volume

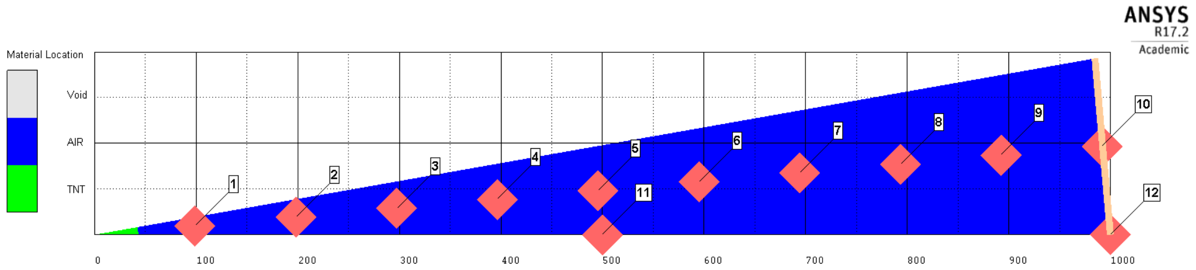

Figure 7.2: *Wedge used for "1D" blast simulation. Beige line indicates flow out boundary condition and red diamonds indicate measuring gauges.*

of 0,5 kg of TNT with a density of 1630 kg/m^3 equal to 306,75 cm^3. The outer radius of the charge, R, is thereby determined to 42,8 mm. The simulation is solved until 2,1 ms, which is the time of arrival and duration time for the last gauge, plus some margin, determined with ConWep. The gauge measurements are compared with each other and results from ConWep, see figure 7.3. ConWep is used as a benchmark as it is deemed trustworthy given the extensive experimental work the software is based on and wide use among military and researchers.

It can be seen that there are general agreement between the three methods. However it appears that Autodyn slightly underestimates the pressure at most of the distances, but are still within reasonable tolerance for distances over 0,5 m. For the first three distances the difference between Ideal Gas and JWL is seen in that Ideal Gas curve is significantly lower than JWL but grows to comparable value. A slight difference in time of arrival is observed between ConWep and Ideal Gas, while JWL follows ConWep closely in the beginning, Ideal Gas converges closer to JWL while ConWep develops some difference to both of them. Figure 7.4 shows the maximum pressure at each gauge and it is clear that Autodyn underestimates for the short distances and are closer to ConWep for larger.

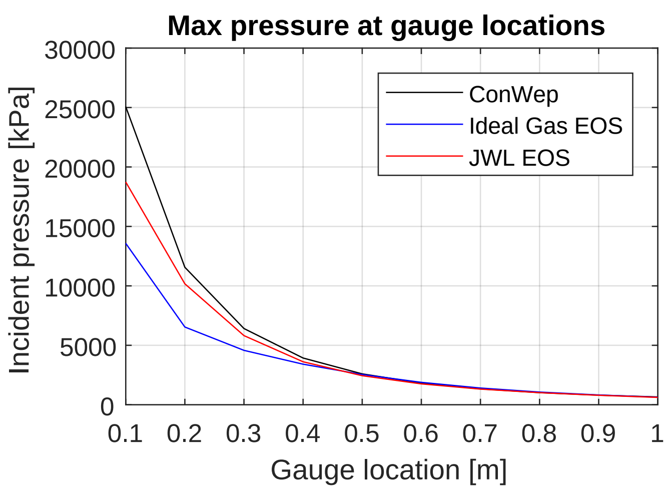

Figure 7.4: *The maximum overpressure for the three methods at each gauge point.*

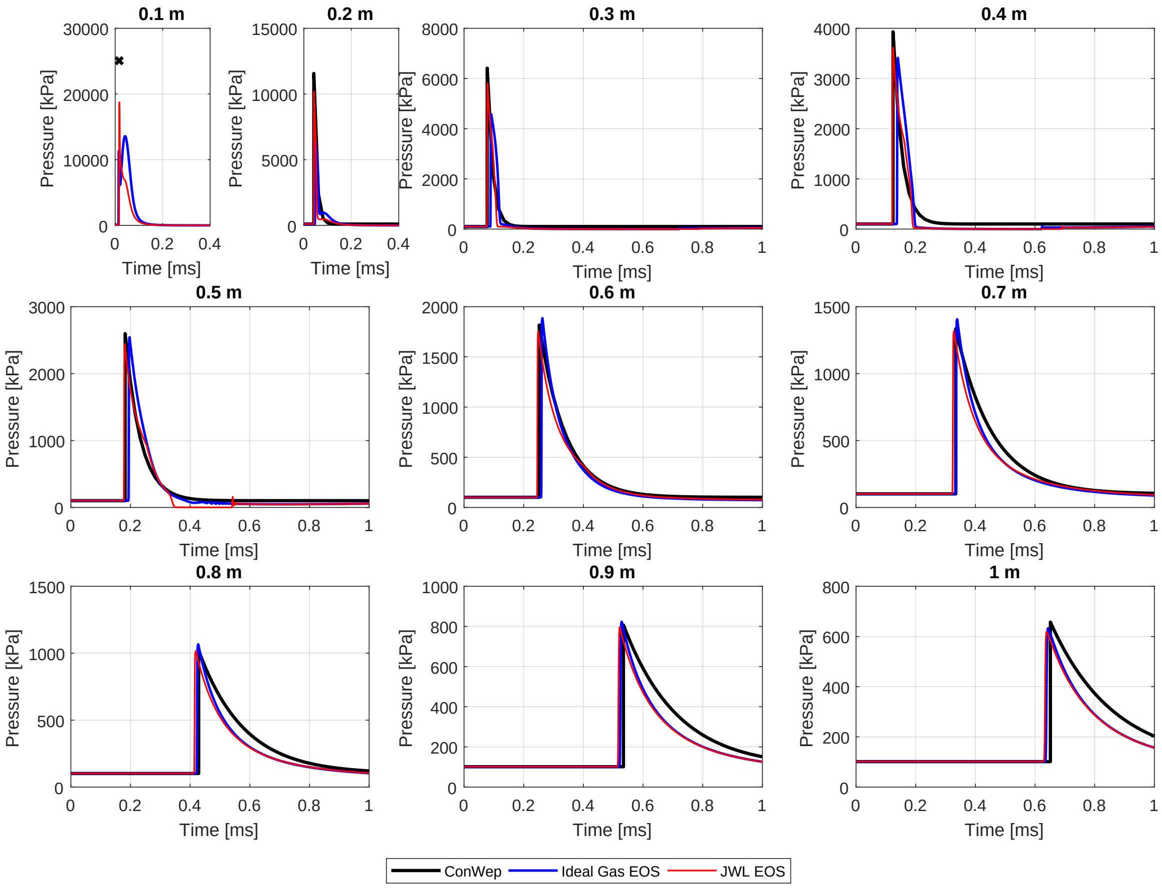

Figure 7.3: *The pressure responds of 0,5 kg of TNT for different distances and methods. The lack of a curve from ConWep at 0,1 m is due to lack of data for this small scaled distance.*

Figure 7.5 shows the incident impulse at each gauge location and it is clear that Ideal Gas greatly overestimates the impulse at distance 0,1 m. It also shows that all methods yield the same general tendency with a small bump around distance 0,5 m.

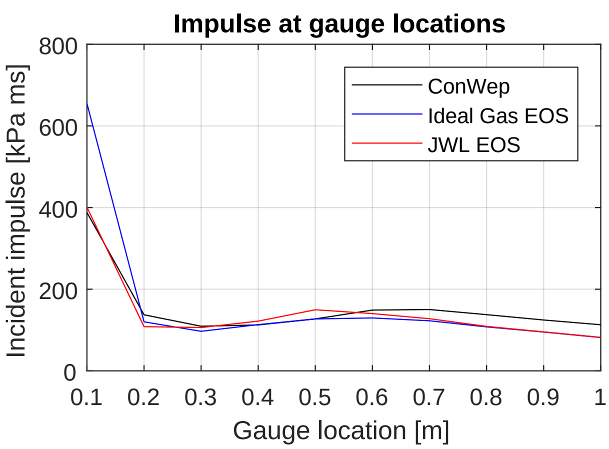

Figure 7.5: *The incident impulse for the three methods at each gauge point.*

7.3.2 Mesh

The mesh is one of the most important factors in a simulation with regard to solve time and accuracy, if not the most important. The size of the elements/cells directly impact the solve time as the time step size is defined by the characteristic length of the smallest element/cell and the sound speed in that element/cell. See appendix F. This means that the solve time can be quite long, even if the mesh is relatively coarse but a single element is small. A finer mesh follows the geometry of the structure better and give a more detailed result. Failure happens for full elements and a coarse mesh results in large sections of a part to be marked as such. If erosion is used and activates at failure, this yields large losses of potential energy and physical boundary.

7.3.3 Boundary conditions

The boundary conditions are, as in most simulation tools, highly important for hydrocode simulations. Different types of boundaries exist and what is equivalent to no boundary condition. Lagrange treats no boundary as free and Euler as rigid, no flow in or out. Like the rest of the simulation, the boundary conditions should mimic the real world as close as possible, but still let the simulation finish in reasonable time. The boundary conditions may not affect the solve time by themselves, but in the grander scheme they can be an effective way to reduce the size of the system.

Fixed

In Lagrange, a fixed boundary condition enforces a zero velocity for the selected nodes. No movement is thereby obtained. In the real world this is a very rare occurrence as everything have some flexibility and stress waves may propagate through a mounting point and into the ground. If this point is modelled with a fixed boundary condition these waves will reflect back into the system. This must be taken into consideration when setting up the system. The equivalent condition in Euler is a rigid face that blocks material flow through a cell face. As it is applied to the cell it acts more like a rigid wall than a fixing of material.

Flow out

In Euler, a flow out boundary condition allows material movement out of a cell, usually at an edge of the domain. As the data for the material that leaves the domain is lost, possible re-entry, inflow, of the material is impossible.

Analytical blast load

Autodyn contains a special boundary condition named Analytical Blast Boundary Condition and is an implementation of the pressure calculations of TM 5-855-1, similar to ConWep, described in chapter 4. This makes it possible to apply an accurate blast load to a Lagrange face without simulation the entire blast. Analytical blast load is not accessible through ANSYS Explicit Dynamics and is not supported for parallel processing.

8 | Design of Humvee floor

The following chapter concerns the design of the floor of the Humvee capable of absorbing the energy in a blast load.

Different concepts in blast absorbing armour design are to be tried and compared against reference design. The reference design is a basic sandwich consisting of a disrupter-absorber-disrupter plate combination which is equivalent to a sandwich of 3 mm ARMOX 500T steel plate, a 18 mm Alulight foamed aluminium plate, and 3 mm ARMOX 500T steel plate as backplate. This has a combined specific mass of 54,9 kg/m^2 which is equivalent to a 7 mm ARMOX 500T steel plate, making the 18 mm of Alulight foam equivalent to 1 mm of ARMOX 500T with regard to mass. With a radius of 250 mm the area becomes $196{,}4 \cdot 10^3$ mm^2 and the total mass becomes 10,8 kg.

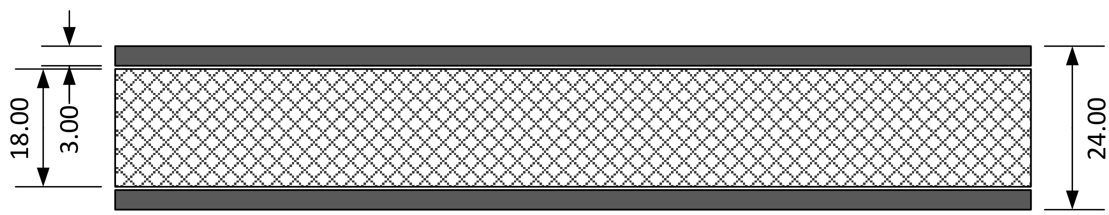

Figure 8.1: *The basic sandwich design for comparison. Composition: ARMOX 500T - Alulight - ARMOX 500T. Mass: 10,8 kg. Area:* $196{,}4 \cdot 10^3$ mm^2.

In the preceding concept, the main task of the disrupter plate is to maintain structural rigidity of the foam during the blast. It is mentioned in chap. 2 that advanced ballistic protection is not necessary in the armour for the vehicle floor, and therefore it is tolerable with a minimum of ballistic protection against e.g. fragments which the ARMOX offers in this case.

The design concepts showing the most promising effects are further investigated in an augmented study.

8.1 Design concepts

A variety of very different concepts are presented in the following. Ideally, it is necessary to fully optimise the specific design concept before a comparison against the basic design presented in the preceding section. However, this is not an option within an appropriate timeframe whereas the design concepts are simulated in a somewhat basic version, i.e. a first iteration of a design along with some intuition, and evaluated based on the ability to reduce transferred force in the current iteration, and the potential of the design assessed by the members of this project. Granted, this is not ideal but a necessity.

Furthermore, a number of limitations are imposed on the design concept to make sure a potential design comply with the requirements of an armour plate for the floor of a military vehicle, in this case the Humvee, see chapter 3 for the general limitation.

- **Ballistic protection:** The use of ARMOX as the disruptive plate is regarded as sufficient protection against ballistic threats such as fragments. This assumption greatly reduces the number of configurations as decision and options regarding disruptive layer (usually ceramic), backing plate (usually ARMOX) and spall liner (usually Aramid) are not considered. Composhield are experts in this field of study, and if ballistic protection in the future is deemed necessary, they have the solution.
- **Blast load:** The blast load is applied with the use of the analytical blast load boundary available in Autodyn.

8.1.1 Concept 1: blast wave effect reduction system

This design concept utilises the property that flow at supersonic speed has different reflection responds depending on angle and speed. Mainly two types of reflection are of interest, regular reflection and mach reflection. Mach reflection yields forces upon the target at higher magnitude than regular reflection. The design concept utilises this by shaping the surface so that regular reflection occur at most of the exposed plate. The concept is therefore an add-on for the basic design and investigate if there is any noteworthy effect, [Kucherov and Hubler, 2014].

The design concept consists of alternating peaks and valleys of parabolic shape. The peaks alternates between high and low. The high peaks must have an angle, α, that ensures regular reflection while the low peaks must ensure that the exiting wave clears the high peak to avoid trapping the wave. See figure 8.2.

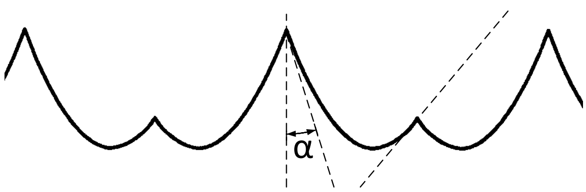

Figure 8.2: *Example profile of the blast wave effect reduction system, [Kucherov and Hubler, 2014].*

8.1.2 Concept 2: elastomeric coating containing hollow spheres

This concept utilise an elastomeric coating in which hollow spheres of either ceramic or hard metal are encapsulated for blast protection, [Roland et al., 2015]. To maintain the characteristic rubber-like properties of the elastomer, it is desired to use an elastomer with a glass-transition temperature in the negative span. Despite the purpose of containing the spheres, the elastomer distributes the singular pressure to a larger area in cases of a kinetic threat for e.g. a projectile. This means one has to consider an impact-induced phase transition of the elastomer to the glassy state which is accompanied by large energy absorption and brittle fracture, [Bogoslovov and Roland, 2007]. Furthermore the backplate is added for rigidity.

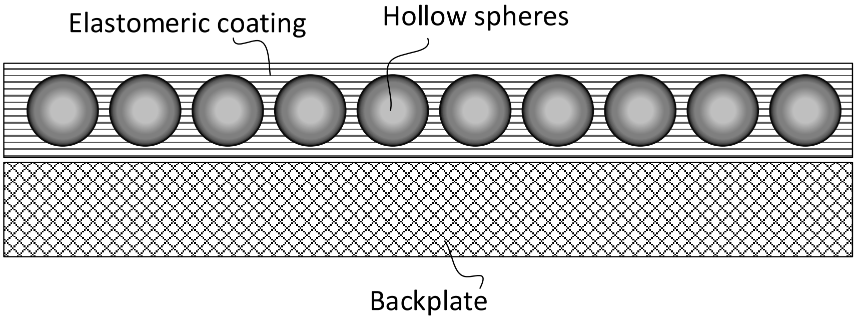

Figure 8.3: *Sketch of design concept. A single layer of spheres is shown, but two or three layers etc. are also a possibility. From: [Roland et al., 2015].*

Three mechanisms are thought to contribute to the blast resistance, [Roland et al., 2015];

1. Energy dissipation due to the visco-elasticity of the elastomer, an absorption that becomes even greater if it undergoes the phase transition.
2. Energy dissipation due to break-up of the spheres
3. Difference in acoustic impedance between the different compounds of the armour plate, i.e. spheres, elastomer, backup plate resulting in destructive interference and dispersion of the wave.

It is suggested in [Roland et al., 2015] to consider using spheres in the range of Ø1-5 mm with a wall thickness so the areal density of elastomer and spheres are homogeneous.

8.1.3 Concept 3: hemispherical indentations

Following the above described concept, a similar concept utilising some of the same mechanism of wave dissipation through mechanical deformation is suggested using hemispherical indentations in two opposite facing sheets, figure 8.4. The sheets are to be of an elastically deformable material, as stated in [Wagner et al., 2014].

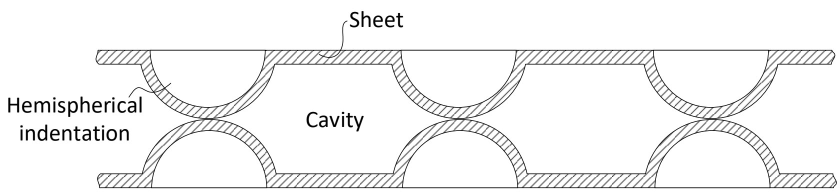

Figure 8.4

8.1.4 Comparison of design concepts

To compare the different proposed concepts and their protective effects under blast loads a number of hydrocode simulations are conducted. To simplify and reduce the number of nodes and solve time, axisymmetry is applied. The concepts are modelled as plates with a radius of 250 mm, and are axially constrained at the distal 10 mm. The concepts are applied an analytical blast load, as available in Autodyn and decribed in chapter 7, of 0,5 kg equivalent TNT and a distance of 0,5 m to the back side of the back plate.

The comparison is made by two methods. A comparison of the design concept against the basic design in figure 8.1 in which the mass of the system is kept equal, i.e. a comparison of specific energy absorption. The other mean of comparison is keeping the thickness of the system equal. Hereby, the two main requirements for the floor panel is assessed in the design generation.

The different concepts as modelled in Autodyn are shown in figure 8.5. Figure 8.5 also shows a model with a rubber sheet as front, a model with a thicker foam core and one with an additional aluminium front sheet. Displacement of the back sheet at the centre is recorded as well as the reaction force at the support. The materials used for the simulations are obtained from the ANSYS material library, except the ARMOX 500T and Alulight material which are described in appendix G.

Concept 1: Blast wave effect reduction system concept.

The blast wave effect reduction system, called the wave concept, is modelled so that the mass of the system is the same as that of the base concept. The height of the high peaks is 10 mm and 2 mm for the low peaks with a distance of 20 mm between each high peak. The angle of the high peak is 19°. Due to the nature of the effect of this concept, this can not be modelled using the analytical blast load. It is therefore modelled with the blast load applied through an Euler domain modelling the explosion from a charge in the same way as in section 7.3.1. To ensure that the effect of the wave concept can be properly compared, a similar simulations are conducted for the base concept. The displacements for the two simulations are shown in figure 8.6.

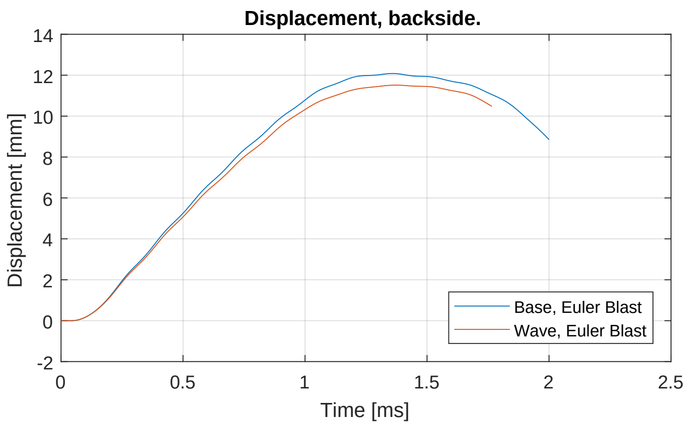

Figure 8.6: *Displacement of the centre point of the back plate for the base concept and wave concept.*

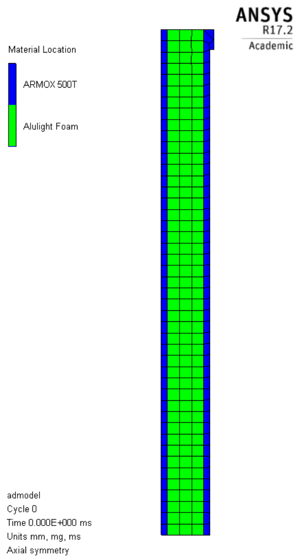

(a) Base concept.

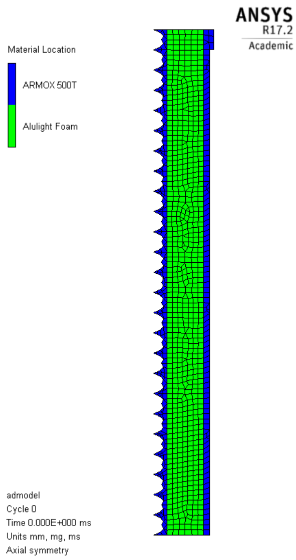

(b) Blast wave effect reduction system concept.

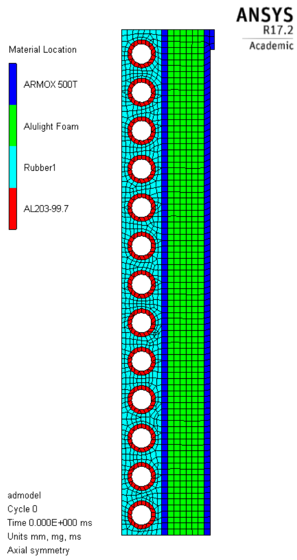

(c) Elastomeric coating containing hollow spheres concept.

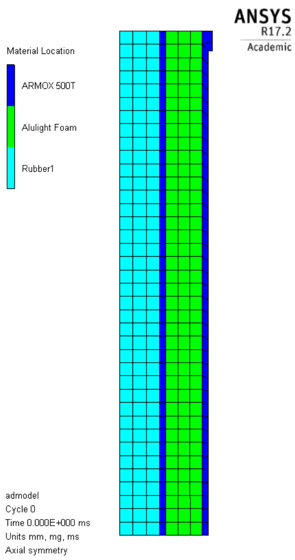

(d) Elastomeric coating concept.

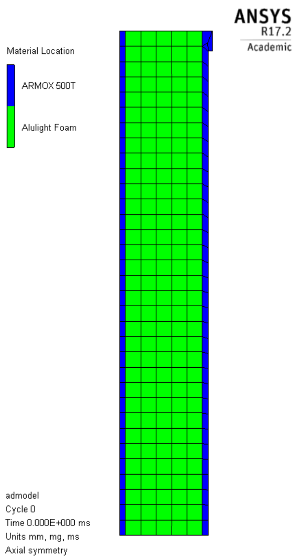

(e) Thick foam concept.

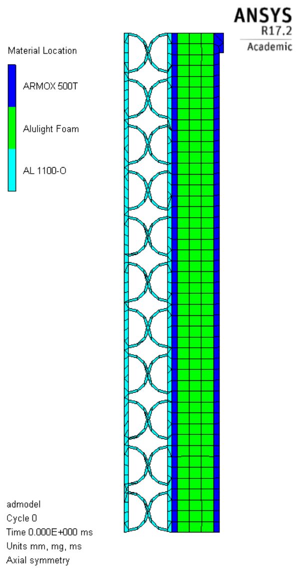

(f) Hemispherical indentations concept.

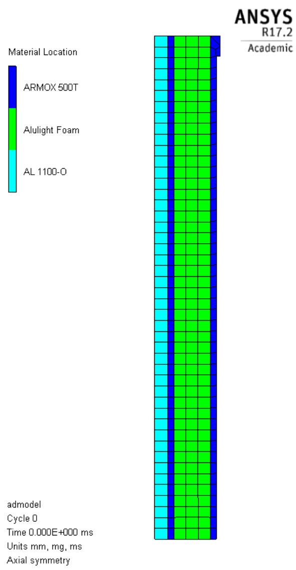

(g) Additional aluminium front sheet concept.

Figure 8.5: *The different concepts as modelled in Autodyn.*

As is seen in figure 8.6, the effect of the concept is noticeable but small. It must be noted that simulating Euler-Lagrange integration requires a fine mesh in the Euler domain for an accurate result. Again due to the constraint on number of nodes and time, the model is relatively coarse. It is therefore likely that the effect would be greater in physical experiments. The concept is here implemented into the outer disruptive ARMOX plate, but according to the inventor it does work for softer materials.

Concept 2: Elastomeric coating containing hollow spheres concept.

The elastomeric coating containing hollow spheres concept is, as mentioned, meant to be hollow ceramic spheres embedded in rubber. But as axisymmetry is used for the simulation the spheres are instead modelled as hollow cylinders and is called ceramic cylinder concept. These are modelled as 14 mm in diameter, and an overall thickness of 20 mm. It is desired to test the effect of cylinders of smaller diameter, approx Ø5 mm, but this is impossible due to the available number of nodes. The ceramic cylinder concept is compared to the base concept, a similar one with a rubber sheet of the same thickness, and one with thicker foam core so that the overall thickness is the same. The four models are shown in figure 8.7.

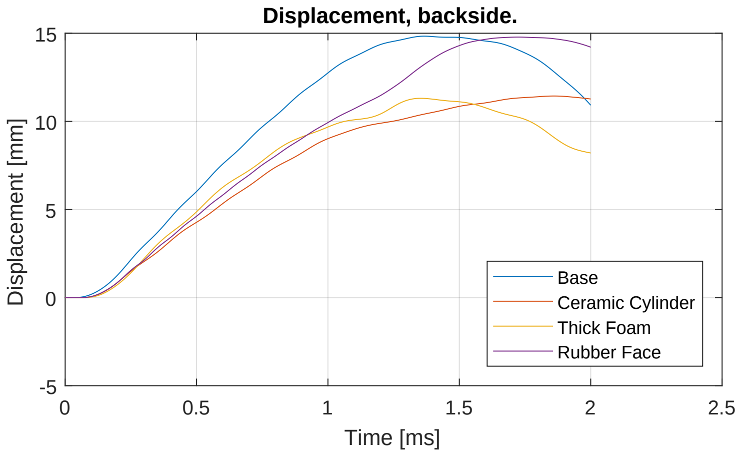

Figure 8.7: *Displacement of the back plate at the centre for the base concept, ceramic cylinder concept, a rubber face concept.*

It is seen in figure 8.7 that the ceramic cylinders reduce the displacement significantly compared to both the base concept and for a pure rubber face. It is noted that the rubber face delays the displacement but has little to no effect on the magnitude. The thicker foam core reduces the displacement approximately as effective as the ceramic cylinders, but do not show the same delay. It should be noted that the ceramic cylinder concept and the rubber face concept have the same mass and dimensions, while the thicker foam core concept have the same dimensions it is less than half the mass making it superior to the others.

Concept 3: Hemispherical indentations concept.

The hemispherical indentations concept is, like ceramic cylinder, modelled as axisymmetric, despite this making them half tubes instead of hemispherical indentations. The indentations are modelled in aluminium 1100-O as is shown in figure 8.5(f). A similar concept with a solid sheet of similar material and same mass is modelled for comparison. The displacement at the center of the back sheet of these two concepts and the base concept is shown in figure 8.8.

It is seen from figure 8.8 that, compared to the base concept, the hemispherical concept significantly reduces the displacement at the centre of the back sheet. The added mass

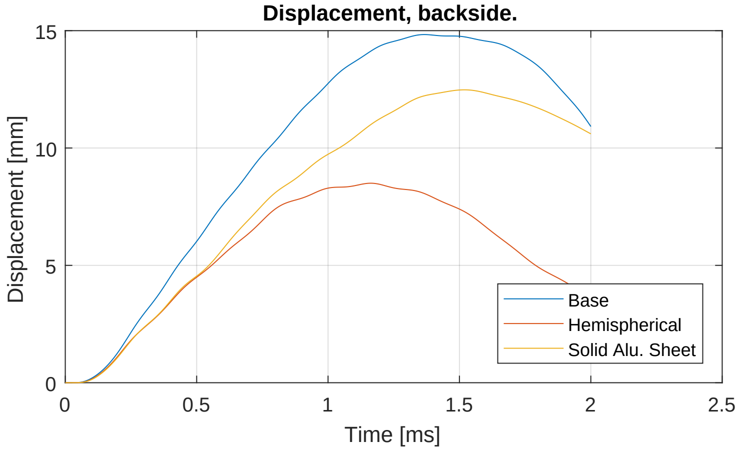

Figure 8.8: *Displacement of the back plate at the centre for the base concept, hemispherical indentations concept, and a thick front sheet concept.*

and stiffness from the additional aluminium front sheet also reduces the displacement, but not to the same extent.

Conclusion on concept comparison

It is important to note that the dimensions of each concept are dimensions in a very initial state and are in no way an optimum. The behaviour of each concept is observed to ensure that they correspond with those described in the respective patents. Each concept is compare to a concept with an equivalent base property, mass or thickness, but devoted the critical feature of the specific concept. The maximum displacement of each concept is shown in table 8.1 together with the displacement relative to the base concept.

Concept	Max. displacement	Relative displacement
Base	14,83 mm	1
Wave*	11,51 mm	0,95
Ceramic cylinder	11,44 mm	0,77
Rubber face	14,78 mm	0,99
Thick foam	11,31 mm	0,76
Hemispherical indentations	8,30 mm	0,57
Extra aluminium sheet	12,48 mm	0,84

Table 8.1: *Summary of the maximum displacement of the different concepts and the displacement relative to the base concept. *The wave concept is relative to the base concept with Euler load.*

The wave concept shows little improvement compared to the mass equivalent base concept. The analysis is done in Autodyn with a Euler-Lagrange coupling. The nature of the concept requires a high level of detail and thereby a fine mesh. The restrictions imposed by the academic license limits this and it is expected that the concept yields better result in physical experiments.

The ceramic cylinder concept shows improvement over the mass and thickness equivalent rubber face concept while it yields same deflection as the thickness equivalent but lighter thick foam concept. Manufacturing hollow ceramic spheres, as the patent describes, must be considered to be quite expensive compared to expanding the foam thickness. The analysed concept makes use of ceramic cylinder rather than spheres but it is not expected that the difference will be significant enough to justify the cost, compared to alternative concepts.

The hemispherical indentations concept shows very significant reduction in the deflection compared to the lighter base concept and the mass equivalent solid aluminium sheet concept. The concept is considered to be relatively cheap to manufacture as it can be made by deep drawing aluminium sheets and then welded together.

From the analysed concepts it is clear that the hemispherical indentations yields the most significant improvement. The wave concept can be combined with this concept by milling it into the front face for an enhancing effect. The ceramic cylinder/sphere concept is dropped as it is not considered to yield improvements significant enough to justify further work.

8.2 Further investigation of the indentations concept

The hemispherical indentations concept is in the following section investigated further. Parameters that affect the blast protective properties are identified and an ideal configuration is determined.

The original concept describes the indentations as hemispherical, but the ratio between the height and radius of the indentations is found to have significant effect on the protective properties. The indentations are therefore designed as hemiellipsoidal with the two radii, denoted as height and radius, controlled independently. The indentations are fixed to the base sheet which they are formed from and are therefore of the same thickness, see figure 8.9. A sheet with indentations is called an indentation sheet. The height of the indentations is measured as the height of the indentation sheet, from top point of indentation to opposite side of the base sheet. The indentations are evenly spaced with a fixed, centre to centre, interval in a grid pattern.

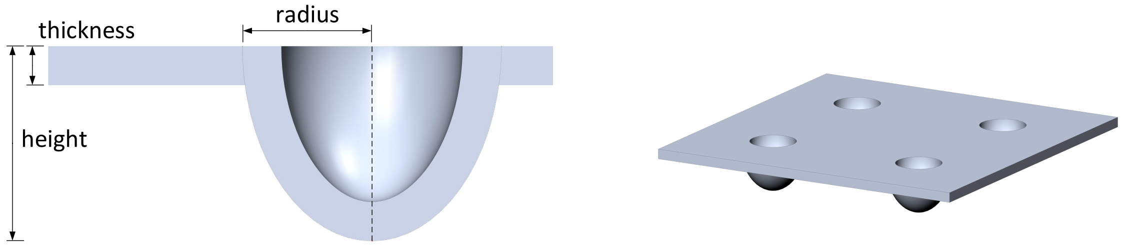

(a) The hemiellipsoidal indentations.

(b) The indentations are placed in a regular grid pattern.

Figure 8.9: *The indentations shape and placement.*

The original concept places two indentation sheets opposite each other so the indentations connect, apex on apex. This is hereafter called the `mirrored configuration`.

To provide some stiffness, and ballistic protection, armour plates are placed on either side of the indentation sheets. This is illustrated on the `mirrored configuration` in figure 8.10.

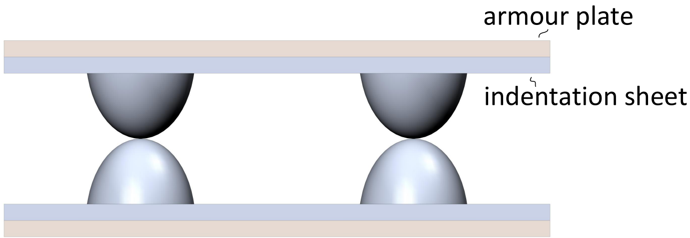

Figure 8.10: *The* `mirrored configuration` *of indentation sheets with armour plates.*

Different configurations are also designed and tested. One configuration is a shifting of the two indentation sheets relative to each other, hereafter called the `shifted configuration`. Thereby making the indentations connect on the base sheet, as illustrated in figure 8.11(a). This configuration essentially doubles the 'density' of indentations in the plane and halve the thickness. Another configuration is also based on shifting the indentation sheets, but adding an additional sheet between the indentations, hereafter called the `shifted w. middle sheet configuration`, as illustrated in figure 8.11(b). This configuration retains the 'density' of indentations if disregarding the slight increase in thickness.

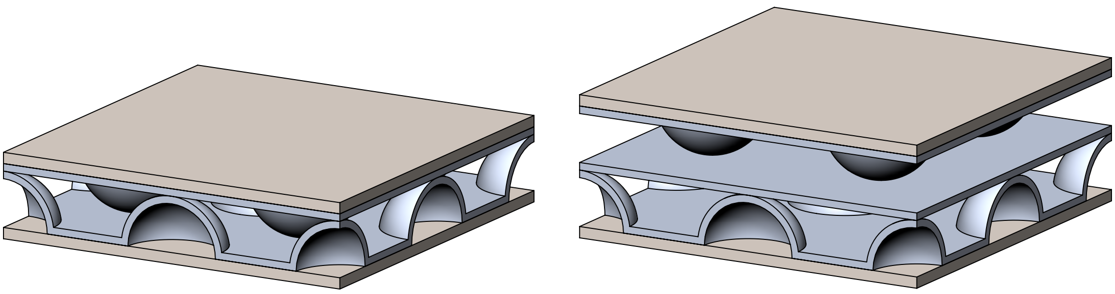

(a) `Shifted configuration` with connection on base.

(b) `Shifted w. middle sheet configuration` that connects on the middle sheet.

Figure 8.11: *Shifted indentations configurations.*

All three configurations are simulated in ANSYS and compared on their blast protective properties. The analyses are performed on 100x100 mm sections. The height and radius of the indentations are set to 15 mm, making them hemispherical. The thickness of the indentation sheet is set to 2 mm, likewise is the middle sheet for the latter configuration. The distance between each indentation is set to 50 mm which gives four indentations in each indentation sheet. The shifted indentation sheets contain half and quarter indentations, but adds up to four in total. The armour plates on either side are given a thickness of 3 mm. This yields an overall thickness of 36 mm for the `mirrored` configuration, 23 mm for the shifted configuration and 38 mm for the shifted w. middle sheet configuration.

The indentation sheets are modelled with the Al 1100-O material from the material library and the armour plates are modelled with the ARMOX 500T material, see app. G. An evenly distributed, linearly decaying pressure load is applied on one side of the sections. This represents a surface blast from a 0,5 kg charge at a distance of 0,5 m, this equals a peak reflective pressure of 24,8 MPa and a duration time of 0,108 ms. The sections are fixed in the opposite end. The peak force load is thereby 248 kN. The charge size and distance is chosen as a benchmark that is also used in other simulations. The analyses are made with an element size set to 2 mm to achieve a sufficient fine mesh and to avoid the constraint of maximum number of nodes.

The mirrored configuration yields a peak reaction force of 64,3 kN while the shifted configuration yields 120,4 kN, and 92,3 kN for the shifted w. middle sheet configuration.

The ratio of roughly a factor of two between the mirrored configuration and the shifted configuration can be explained by considering that the indentation density of the shifted configuration with connection at base is the double of that the mirrored configuration is.

The middle sheet in the shifted w. middle sheet configuration have a blending effect on the reaction force. Blending the responds of the configuration between the mirrored configuration, for a fully stiff middle sheet, and the shifted configuration with connection on base, for a zero stiffness middle sheet.

The reduction in overall thickness for the shifted configuration gives the impression that it is sufficient with just a single indentation sheet and using the stiffer front armour plate as substitute for the second indentation sheet. This configuration is hereafter called the single sheet configuration and is shown in figure 8.12(a). This is investigated in the same way as the other configurations, with an indentation height of 15 mm, radius of 15 mm and thickness of 2 mm.

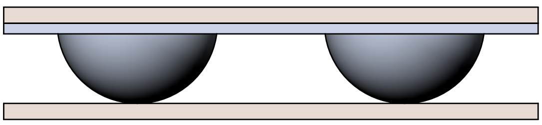

(a) The single sheet configuration.

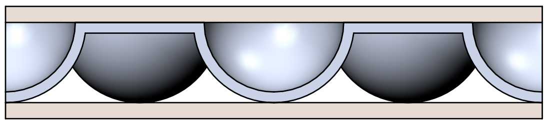

(b) Indentations configuration with only one indentation sheet with packed indentations.

Figure 8.12: *Single sheet configurations.*

The single sheet configuration yield a reaction force of 123,9 kN which is more than twice as high as for the mirrored configuration. This is due to a larger compression of the individual indentations and thereby larger force. Similarly a single sheet configuration with twice the number of indentations is analysed to compare with the shifted configurations, this one is hereafter called the dense single sheet configuration. The indentations are packed with middle indentations, see figure 8.12(b). This configuration yields a reaction force of 138,8 kN, slightly larger than for the shifted configuration. It is expected that these two configuration show similar result, but with the dense single sheet configuration yielding slightly higher as the shifted configuration have a base sheet against the front armour plate and thereby putting more mass towards the blast load. As it is earlier explained a higher mass of the front plate yields a lower energy which is converted to a reaction force. Flipping the indentation sheet should yield a slightly lower reaction force.

The five different configurations and their results are summarised in table 8.2, masses and reaction forces are given with respect to area, thus specific mass and reaction stress.

Configuration	**Specific mass**	**Reaction stress**
Mirrored	60,23 kg/m^2	6,43 MPa
Shifted	60,23 kg/m^2	12,04 MPa
Shifted w. middle sheet	65,64 kg/m^2	9,23 MPa
Single sheet	53,66 kg/m^2	12,39 MPa
Dense single sheet	54,81 kg/m^2	13,88 MPa

Table 8.2: *Different indentation configuration with height and radius set to 15 mm, indentation sheet thickness set to 2 mm and armour plate thickness set to 2 mm. The masses and reaction forces are normalised with respect to area.*

Further work with the indentation concept is focused on the `mirrored configuration` as this yields the lowest reaction force. A series of simulations are conducted to identify and analyse parameters that affect the blast protective properties. The analyses are again performed on a 100x100 mm section with 50 mm between each indentation and a thickness of 3 mm for the armour plates. The height of the indentations are initially kept constant at 15 mm so that the outer dimensions are likewise kept constant. The radius of the indentations are varied between 7,5, 10, 15, 20 and 22,5 mm, and the sheet thickness is varied between 1, 2 and 3 mm. This necessitate a total of 15 simulation. The recorded peak reaction forces are visualised with a surface plot in figure 8.13

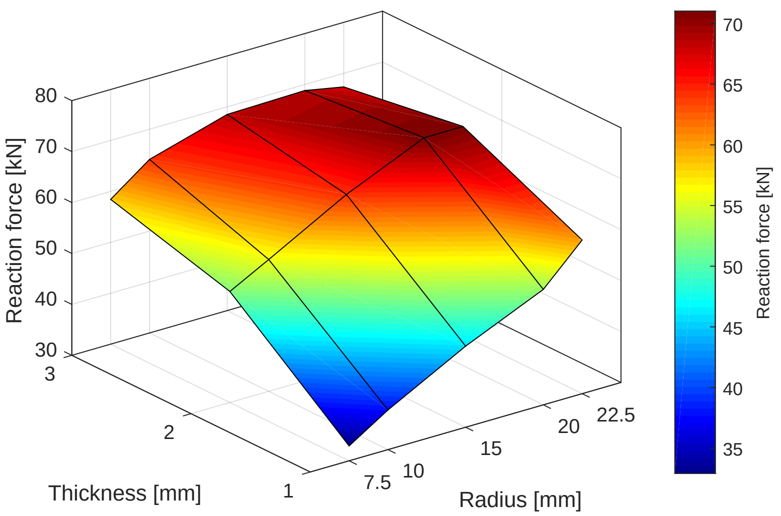

Figure 8.13: *Largest reaction forces, for the* `mirrored configuration`*, with respect to indentation radius and sheet thickness, the indentation height is set to 15 mm.*

It is seen from figure 8.13 that the smallest reaction force, 32,92 kN, of the analysed dimensions, is obtained with a sheet thickness of 1 mm and indentation radius of 7,5 mm, meaning a height to radius ratio of 2. The force increases with both the sheet thickness and the indentation radius. The largest reaction force, 71,02 kN, is found with a sheet thickness of 2 mm and indentation radius of 22,5 mm, meaning a height to radius ratio of 2/3.

It is worth noting that the indentation sheets can be manufactured by deep drawing the indentations into stock sheets. This process can be made fast, relatively cheap and yield consistent results. The parameters can be finely controlled to produce a sheet with specific properties. Compared to the process of foam manufacturing which, for the treated Alulight specimen, yields quite inconsistent results throughout the specimen.

8.3 Final design of protective plate

The previous section analyse the indentation concepts' blast protective properties with respect to different parameters and configurations. The analyses are performed on 100x100 mm sections which are fixed at one side, the final plate is to be a 1x1 m section that is supported on two 100 mm wide stripes on the back plate, running parallel on either side, see figure 8.14.

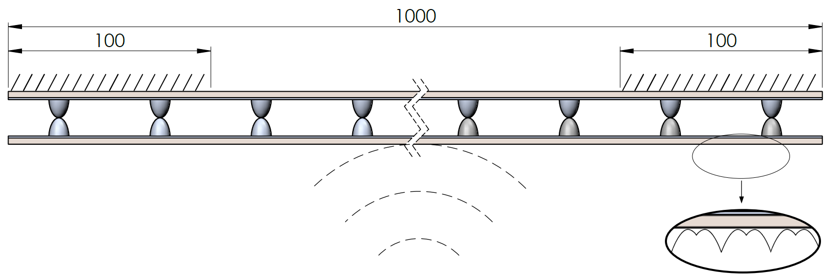

Figure 8.14: *The support profile for the final panel design with the load direction indicated. The blast wave effect reduction system is shown as a possible add on for added protective effect.*

The blast load that is protected against is, as mentioned in earlier chapters, equivalent to a charge weight of 0,1175 kg and a distance of 0,5 m, this is included 20% safety. This results in a peak pressure of 7,706 MPa and a duration time of 0,109 ms. The significant smaller blast load gives the possibility of reducing the indentations on all parameters, but it must be taken into account that the protective plate should still be able to withstand effects and loads from the environment other than the blast load. These effects may arise from the normal use of the Humvee as it traverses rough terrain. As it is shown in figure 8.13 the lowest reaction forces are obtained with a sheet thickness of 1 mm, for the analysed sizes. Thinner sheets are expected to yield an even lower reaction force until an optimum is reached, but to avoid that the indentations become to flimsy to withstand loads from normal use the sheet thickness is set to 1 mm. Ideally an optimisation would be performed to find the optimum indentation radius and height. But the computational heavy nature of the simulations makes this option impossible due to time constraints.

Instead the parameters are set based on intuition obtained from the previous analyses and validated with simulations, first on the 100x100 mm section and finally in a full scale model of a 1x1 m sheet. The analysis of the 100x100 mm section is to ensure that the indentations do not compress completely and the full scale model is to determine the displacement of the back plate.

As the displacement of the back plate is of some importance it is desirable to give the plate sufficient bending stiffness. The bending stiffness is mainly governed by the two outer armour plates, the thickness of the core and the height of the indentations. As it is desired to minimise both the thickness and the mass of the protective plate a compromise is needed. Simulations of simplified models show that 3 mm is a good compromise between stiffness and mass.

It is sought to lower the indentation height as this is the main contributor to the thickness of the design, but it is still important that the reaction force is also low. At least the reaction force must be lower than what is achievable with the foam. The indentation height to radius ratio is set to 2 as it is shown to yield good result and a larger ratio may prove difficult to manufacture. The indentation distance is kept at 50 mm as a higher 'density' would only increase the reaction force and lowering it risks inducing to little local support for small radius blast loads, which the design load is considered to be. After a number of simulations with different indentation heights, the height in the final design is set to 10 mm and an indentation radius of 5 mm. Larger indentations height yields little to no reduction in reaction force and lower height causes full compression of the indentations which has to be avoided.

The final design is thereby a `mirrored configuration` of the indentations concept with an indentation height of 10 mm, radius of 5 mm, with a distance of 50 mm between each indentation and a sheet thickness of 1 mm, made from 1100-O aluminium. Two armour plates of 3 mm thickness each is placed in either side to form a sandwich structure. For the 100x100 mm section the reaction force is 10,8 kN and the mass is 0,528 kg resulting in a specific mass of 52,8 kg/m^2. A full scale optimisation may yield different parameters, but this is found to be, at least, close. Additionally can the blast wave effect reduction system be added to the front of the panel, as illustrated in figure 8.14, for added protective effect at little to no additional cost with respect to mass and thickness.

The parameters for the final panel are summarised in table 8.3.

Parameter	Value	
Indentation height	10	mm
Indentation radius	5	mm
Indentation sheet thickness	1	mm
Indentation distance	50	mm
Armour plate thickness	3	mm
Total thickness	26	mm
Specific panel mass	52,8	kg/m^2
Reaction stress	1,08	MPa

Table 8.3: *The best found parameters for the indentations for a blast load from a charge of 0,1175 kg and at a distance of 0,5 m. The indentation sheets are made from 1100-O aluminium and the armour plates are made from ARMOX 500T.*

A simulation of a section with the same dimensions, but with a core of Alulight foam instead of the indentation parts, is conducted, i.e. a sandwich of 20 mm foam with a 3 mm ARMOX 500T sheet on either side with a mass of 0,563 kg, and thereby a specific mass of 56,3 kg/m^2. Applied the same boundary conditions as for the indentation section, the largest compressive reaction force is recorded to 26,4 kN, or 2,64 MPa. Likewise, the section is simulated with a foam core thickness of 12,52 mm making it mass equivalent to the indentation parts. The largest compressive reaction force is recorded to 26,5 kN, or 2,65 MPa for this foam thickness. The results for the foam sections and the final indentations design as well as the best design from the parameter study are shown in table 8.4.

Configuration	Specific mass		Reaction stress	
Indentation - 15-7,5-1	53,3	kg/m^2	1,09	MPa
Indentation - 10-5-1	52,8	kg/m^2	1,08	MPa
Foam - equal mass	52,8	kg/m^2	2,65	MPa
Foam - equal thickness	56,3	kg/m^2	2,64	MPa

Table 8.4: *Comparison of the specific mass and reaction stress for the best configuration from the parameter study, the final configuration and two foam configurations. The indentations configurations are given with there height-radius-sheet thickness. The load is equal to a blast from a 0,1175 kg charge at 0,5 m distance. The ARMOX plates are 3 mm thick for all configurations.*

It is noted, from table 8.4, that the indentation sections are capable of yielding lower reaction forces, than the foam sections, for both configurations. Given that the mass of the aluminium foam sandwich is higher, or equal, than the indentation concept in the mirrored configuration, it is thereby reasonable to conclude that the indentation concept is superior to the treated Alulight foam in blast protection compared to both mass and volume. The two indentation configurations in table 8.4 yields very similar reactions but the final one is 2/3 the thickness.

The final 1x1 m panel is modelled and an analytical blast load, as described in chapter 7 is applied at the centre of the plate, with a charge weight of 0,1175 kg and a distance from the centre of the panel of 0,5 m. By the use of symmetry the model is reduced to a quarter section. As the model greatly exceeds the maximum number of nodes, it is impossible to run the simulation using the academic license. The more than 380.000 nodes, the small time step and the long simulation duration also makes it highly impractical to perform even with a full license on a fast computer. Additionally, the analytical blast load is not supported for parallel processing, extending the solve time even more.

A way around this problem is to simulate a compression test of the indentations and use the results to define a material model. This makes it possible to use significantly larger elements and thereby reduce the number of nodes and achieve a larger time step. This procedure is not applied with sufficient successfully results due to time constraints, but a simulation using the Aluligth foam is performed. As the foam yields larger reaction forces than the indentations it is reasonable to assume that the indentations will perform better.

The simulation of the foam panel yields a displacement at the centre of the backplate, directly opposite the explosion, of 17 mm and a time to maximum deformation of 3,2 ms. That may not be considered to be much, but it could still prove to be dangerous for personnel inside the vehicle. The indentations are expected to at least half the result of the foam.

The micro-truss structure from section 5.3 is proposes as a replacement for the foam and is like the indentations highly modifiable to a specific load case. The micro-truss structure shows a behaviour which is more like that of the foam, with a plateau stress and densification strain, than the indentations. The plateau stress behaviour is often considered to be favourable when treating blast loads, but the complex and costly manufacturing process of the micro-truss structure make the indentations a better alternative in certain cases. The computationally heavy nature of the micro-truss structure, like the indentations, makes them impractical to simulate in full scale. The equivalent material method may also be applicable in this case but are likewise not applied with sufficient successfully results due to time constraints.

Experimental physical test of, indentations, micro-truss and foam are to be performed. It is expected that the indentations are to yield the most beneficial results based on the simulations. The wave concept is of special interest as it is proven difficult to simulate this reliably. Experimental test can be used to validate the simulation and expose unexpected behaviour.

9 | Plan for experimental work

The following chapter treats the planned experimental work of the project. It has not been possible to put up a deal to conduct a live-blast test of the armour plate, why small validating laboratory experiments are utilised as replacements. This also means, that the live-fire test only reached the planning phase which is documented in the following chapter. This includes considerations of possible implementations of measurements, assembly of plate etc.

9.1 Laboratory experiments

The laboratory experiments are conducted in the terminal ballistics laboratory in the basement of Fibigerstræde 14, Aalborg University. This lab possess a gas cannon approved to a pressure up to 200 bar ($20{,}0 \cdot 10^6$ Pa), capable of firing projectiles between Ø10 - 70 mm. The propellant gas is in the present case atmospheric air compressed to the desired pressure by an industrial compressor. The valve to release the pressure in the chamber is remotely operated in safety outside the room. Documentation of the impact is achieved using a high speed camera capable of 200.000 fps, however at a very low resolution. A chronograph using photocells is present to measure the velocity of the projectile used for replication of the blast wave.

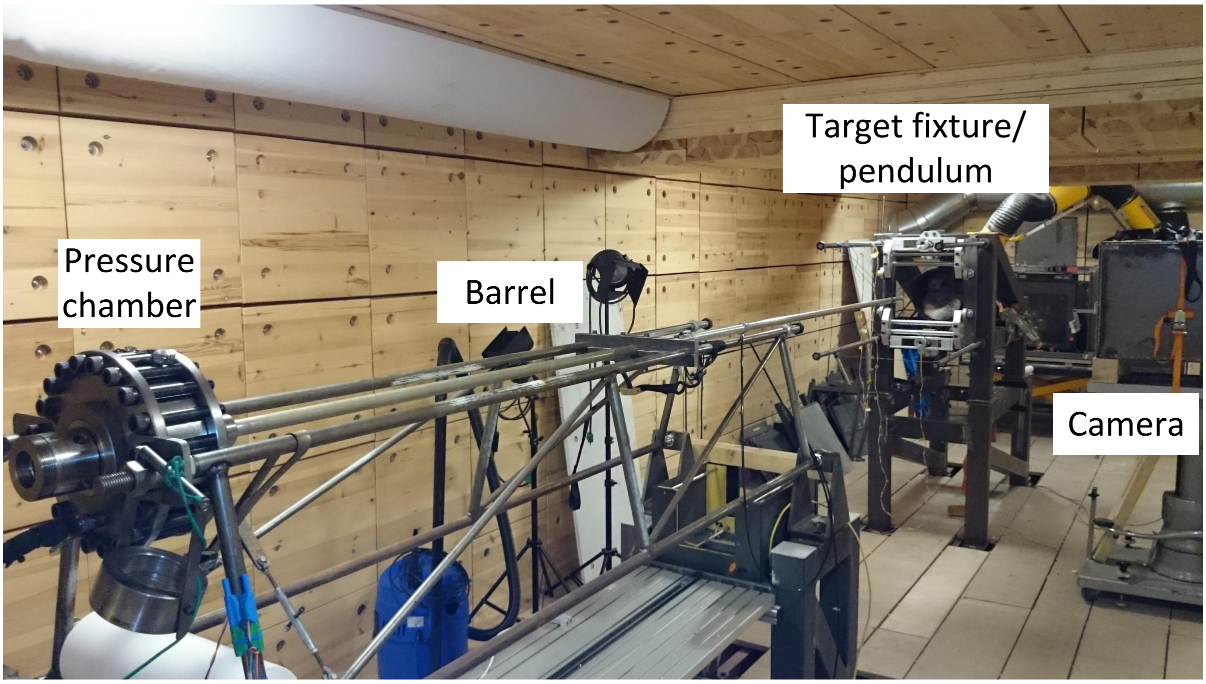

Figure 9.1: *Terminal ballistics laboratory in the basement of fibigerstræde 14, Aalborg University.*

9.1.1 Motivation for the experiment

In this section, a plan for the small validating experiments conducted in the laboratory for validation of some of the analytical and numerical parameters are described.

At the moment, a discrepancy between the analytical and numerical models exists, either the analytical model is overestimating or the numerical model is underestimating the deformation quite significantly. It is because of the assumptions taken in the two methods, e.g. when the same initial velocity is applied to the front plate as a direct input, the deformation in the foam is equal using the two methods. However, when calculating the kinetic energy transferred from the blast load to the front plate in the analytical model, and using the '*analytical blast load*' in the numerical study to calculate the kinetic energy transferred to the front plate, the results deviate significantly. The difference is, that the analytical model accumulate the kinetic energy in the front plate before deformation starts assuming impulsive loading, in the numerical case, this happens gradually and deformations are obtained for every time step based on the pressure loading, see appendix F, where the software solves the equation of motion for an element at every time step.
Furthermore, the relation between the mass of the front plate and the deformation in the foam is also to be investigated in this experimental work, i.e investigating eq. 6.26.
A number of test specimens of the micro-truss structure is, at the time of hand-in, expected to be manufactured using additive manufacturing (3D-printing), which is a great compromise for prototype manufacturing and should not entail any significant weaknesses in the nodes of the trusses. Experimental validation of the promising results of this structure (sec. 5.3) is desired, and conducted in near-future.

9.1.2 Description of the experiment

An energy transfer from the front plate to the foam is desired replicated in the laboratory. It is assessed, that this is achievable by imparting the kinetic energy in the front plate by launching a projectile into the front plate using the air pressure from the cannon, figure 9.2. The projectile transfers its kinetic energy and gives the front panel an initial velocity, equal to the impact velocity, representing the real case. Conservation of momentum yields

$$m_1\ u_1 = m_1\ v_1 + m_2\ v_2 \tag{9.1}$$

where m_1 and u_1 are the mass and preimpact velocity of the projectile respectively, v_1 is the projectile velocity just after impact and m_2, v_2 are the mass and the velocity after impact of the front plate respectively. To ensure a perfect elastic impact, the contact area must be big enough to reduce the contact stresses to minimum. This allows to assume a conservation of kinetic energy of the system before and after impact which yields

$$m_1\ {u_1}^2 = m_1\ {v_1}^2 + m_2\ {v_2}^2 \tag{9.2}$$

Solving these two equations simultaneously and setting $m_1 = m_2$ yields

$$v_1 = 0 \quad \text{and} \quad v_2 = u_1 \tag{9.3}$$

The foam is attached to a ballistic pendulum as illustrated in figure 9.2. This is used for determination of the energy consumption by deformation of the foam by comparing it with a shot against the plate-pendulum without foam. The perfect-elastic impact assumption can also be validated by comparing the kinetic energy of the projectile and the energy transferred to the pendulum when impacting the front plate without the foam.

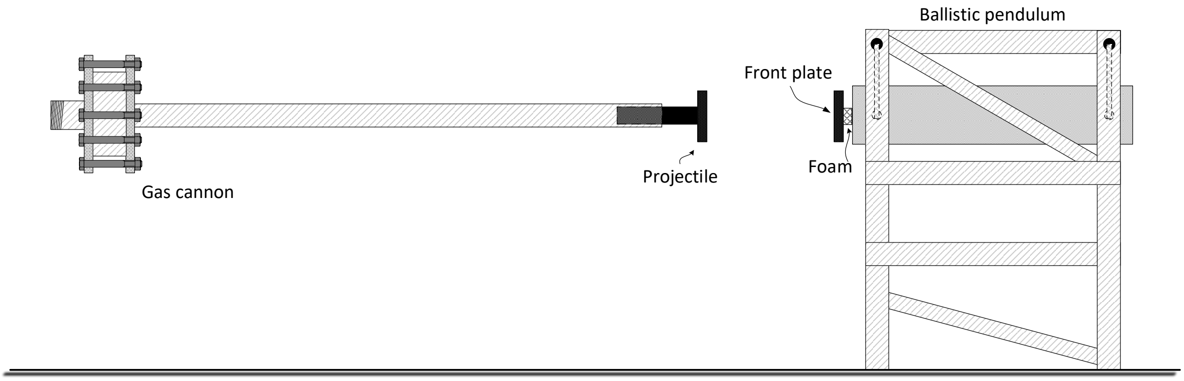

(a) A sketch of the experimental set-up.

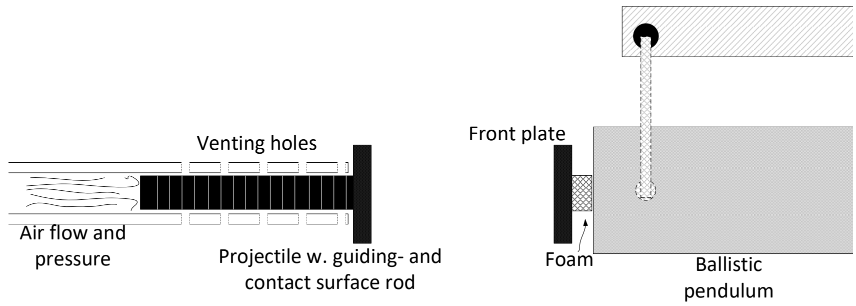

(b) A detailed sketch of the set-up.

Figure 9.2: *Opening the valve in the pressure chamber after pressure build-up ensures airflow into the barrel due to the pressure difference supplying kinetic energy to the projectile. The projectile has a rod attached for guiding to ensure a perfectly normal impact with the front plate and foam. The rod furthermore acts as contact surface for the air flow maximising the energy transfer from the airflow. The lines on the rod are for velocity determination using the high-speed camera. The venting holes distribute the airflow away from the target to avoid tilting of the projectile. Furthermore, they are a safety precaution against barrel explosion in case the rod doesn't leave the barrel, on purpose or not. The ballistic pendulum is for measuring the energy consumption in deformation of the foam based on the swing. The pendulum is designed by the project group, and shown in appendix H.*

Furthermore, the target foam is to be kept as small an area as possible for maximising the pressure applied on it, while remaining representative of the material parameters. Material test performed on cylindrical foam specimens of Ø25 mm, appendix C, showed great variation in material parameters not attributed to anisotropy which is the main test parameter for these specimens. It is therefore concluded, that an area of 419 mm^2 is too little. Slab specimens in the area range $\{1250\ \text{mm}^2 - 3750\ \text{mm}^2\}$ are likewise tested, and showed small variation due to size effect. A foam target of 1250 mm^2 is therefore the smallest obtainable tested target size.

As the impact starts, the projectile comes to rest in very short time, while the front plate accelerates from zero to the impact velocity at the same time. This experiment can be repeated for different thicknesses of the front panel, i.e. different mass. With the same kinetic energy imparted into the plate, the deformations of the foam vs. front plate thickness can be recorded and used for validating the results obtained analytically and numerically.

The above procedure is an attempt to represent a uniform blast load without using a real explosive. The physical nature of a wave pressure produced by an explosion is quite different from that of a metallic projectile. However, in both cases some energy is transferred to the front plate and accelerate this plate resulting in crushing and deformation of the foam.

9.2 A plan for live-blast test

The following section treats the plan and procedure for conducting the live-fire test of the armour floor panel if the opportunity at some point arises. This includes a description of the test set-up including strain gauge measurements and preparation of the panel. The description of strain gauge measurements, including general theory, sources of error, sampling etc. is placed in appendix I.

9.2.1 Set-up

It is desired to replicate an explosion beneath a Humvee as close to real life as possible along with the replication of the analytical blast load.

The analytical blast calculations predict that the entire blast effect is deposit in a 1x1 m plate, if the distance to the explosion is 0,5 m and a charge weight of the DM51 hand grenade with 20% additional margin meaning a TNT equivalent weight of 0,1175 kg is used, see figure 4.5 for the plot of the pressure due to this explosion. This is a sufficient representation of the distances beneath the Humvee, as shown in figure 1.2, as the main objective of the test is to determine the behaviour of the armour panel against a real blast load, instead of the replicate in the laboratory tests.

A fixation of the armour panel is seen in figure 9.3. The fixation has to allow a fully vented explosion which is equivalent to an explosion beneath a vehicle.

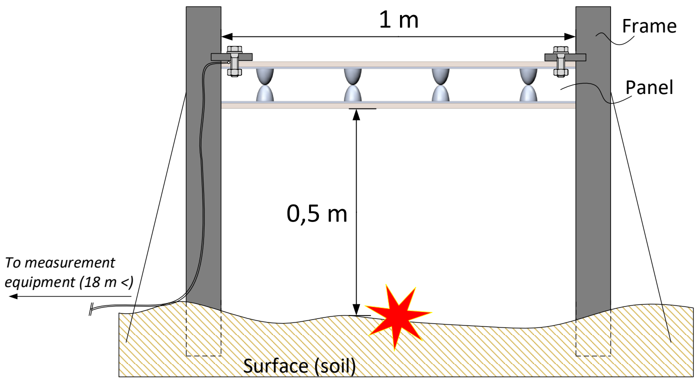

Figure 9.3: *Side view. Sketch of the test set-up for the live blast test. The frame is planned to consist of two welded structures which are buried and anchored sufficiently into the ground so the frame remains completely rigid. The armour panel is bolted to the frame as it is expected the final solution is to the chassis of the vehicle.*

A similar blast test is performed by a former project group where the measurement equipment is placed 53 m away in a 2 m deep hole and the equipment is suspended in rubber bands to protect it against the ground shock and blast wave. Still, the harddrive was affected by the ground shock and data was lost, [Christensen and Olesen, 2007]. Granted, the test was performed with a 155 mm artillery shell with 6,620 kg of equivalent TNT. A similar safety distance is not necessary for conducting tests using the DM51 hand grenade. A quick study is conducted using ConWep's ground shock plug-in for approximating the necessary safety distances.

The case in [Christensen and Olesen, 2007] is replicated in ConWep using the following input parameters, and resulting in the output likewise shown in table 9.1.

Artillery shell 155 mm		
Explosive parameters		
Surface burst		
TNT equivalent	6,620	kg
Distance parameters		
Horisontal	53	m
Vertical	2	m
Soil parameters †		
Dense sand		
Density	2030	kg/m^3
Seismic velocity	488	m/s
Impedance	995	kPa/m/s
Attenuation coef.	2.5	–
No tensile reflection from surface		
No reflections from deeper soil layers		
Output		
Peak pressure	0,1216	kPa
Impulse	$0{,}1309 \cdot 10^{-1}$	kPa-s
Peak particle velocity	$0{,}1288 \cdot 10^{-3}$	m/s
Peak displacement	$0{,}4169 \cdot 10^{-4}$	m

Table 9.1: *Ground shock parameters for artillery shell 155 mm calculation. †: a guess, which utilise median values of soil paramers.*

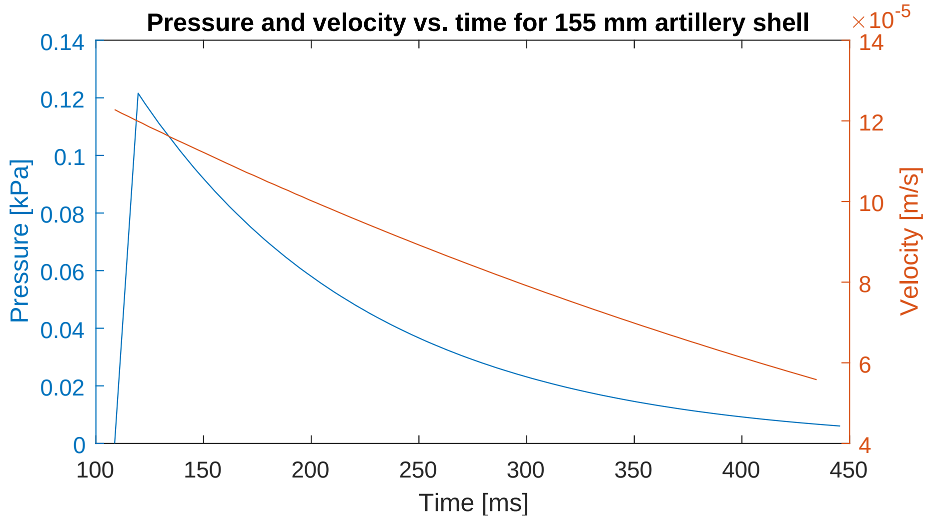

Figure 9.4: *Velocity and pressure vs. time at the measurement equipment for the 155 mm artillery shell at 53 m and 2 m depth.*

Similar ground shock parameters are obtained for the case using the DM51 grenade. Then, this will be the lower bound safety distance for protection of the measurement equipment, as it is unknown exactly what the harddrive etc. are capable of withstanding. The soil parameters are identical to the parameters in table 9.1. An approximation of the range to the measurement equipment is obtained using the Hopkinson-Cranz scaling law, eq. 2.3. The direct distance to the measurement equipment in the case of the artillery shell is $R = 53{,}04$ m, and the equivalent TNT is $W = 6{,}620$ kg.

$$Z = \frac{R}{W^{1/3}} = 28{,}25 \text{ m/kg}^{1/3} \tag{9.4}$$

which is used to calculate the equivalent distance for the DM51 hand grenade explosion of TNT equivalent weight 0,0979 kg

$$28{,}25 = \frac{R}{0{,}0979^{1/3}} \qquad\qquad R = 13{,}01 \text{ m} \tag{9.5}$$

Using this distance where the depth of 2 m is preserved, along with the explosive and soil input, and the following output is obtained, table 9.2.

DM51 hand grenade		
Explosive parameters		
Surface burst		
TNT equivalent	0,0979	kg
Distance parameters		
Horisontal	12,86	m
Vertical	2	m
Output		
Peak pressure	0,1217	kPa
Impulse	$0{,}3213 \cdot 10^{-2}$	kPa-s
Peak particle velocity	$0{,}1229 \cdot 10^{-3}$	m/s
Peak displacement	$0{,}1024 \cdot 10^{-4}$	m

Table 9.2: *Ground shock parameters for DM51 hand grenade calculations.*

It is seen, that the scaling law works as expected, as the peak pressure and velocity are near identical. The remaining parameters, impulse and displacement (tab. 9.1 and tab. 9.2 or fig. 9.4 and fig. 9.5), are smaller for the DM51 hand grenade case.

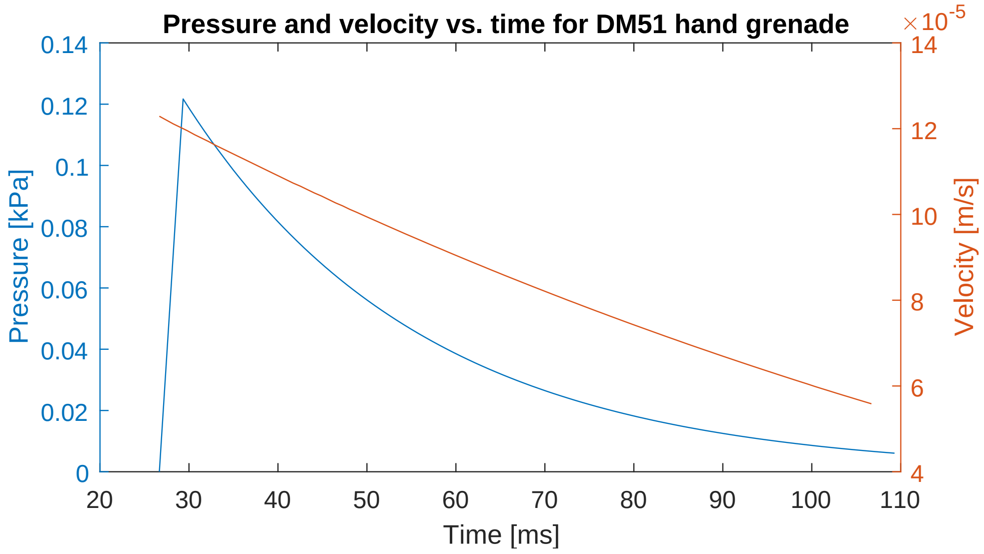

Figure 9.5: *Velocity and pressure vs. time at the measurement equipment for the DM51 hand grenade at 12,86 m and 2 m depth.*

It is noted, that the harddrive in the case of [Christensen and Olesen, 2007] still failed for these blast parameters, but is also assessed that the failure of the harddrive is due to an acceleration and displacement, which in the case of the displacement is more than four times smaller. Therefore, it is assessed that an additional safety distance of 5 m is sufficient based on the rapid decay in the blast parameters. A horisontal distance of 18 m is considered safe for the measurement equipment in testing the DM51 grenade. It should be noted, that in the case of [Christensen and Olesen, 2007], the equipment is suspended in rubber bands. This could also negatively influence the equipment as forced oscillation of these from external factors, e.g. the displacement, other than the ground shock could be to blame for the harddrive failure. This is however unconfirmed and guesswork.

For a description of the strain gauges and their location on the plate, see appendix I.

9.2.2 Results of the blast test

As the blast test has not been conducted, results specific for this study are unavailable. However, a noteworthy observation from the blast test conducted by [Christensen and Olesen, 2007] is the failure of the adhesive attaching the aluminium foam to the rest of the panel. They believe, it is due to the stress wave generated in the blast, or generated as fragments hit the front plate, that delaminates the glue. Furthermore, the protection of the measurement equipment, more specifically the mechanical hard drive in the laptop, was insufficient.

9.3 Test panel

The following section treats the considerations for manufacturing an assembly of a panel for testing, and shortly present the considerations regarding a final armour panel.

Test specimens of the micro-truss structure, and a structure using honeycombs are planned for manufacturing by 3D-printing. These specimens are to be used in the near-future experimental work in the terminal ballistics laboratory for validation and comparison of the results. The CAD-drawings are located in the annex.

9.3.1 Assembly of the different layers in the panel

As observed and stated in [Christensen and Olesen, 2007], the use of an adhesive bonding as coupling of the different layers of the armour panel has some limitations as a large magnitude of stress wave from the impinging blast load, or the resulting fragments, propagates through the panel, and failure might be experienced in form of delamination. This is not durable as e.g. separation of some of the components of the plate reduces the protective capabilities drastically, and alternative methods of bonding are used where possible.

Three different types of sacrificial layers are investigated in the project, the foam material, the micro-truss structure and the indentation sheets. All three of these are considered, until the experimental work has been conducted. The different methods of coupling these with the remainder of the armour panel are therefore needed.

Aluminium foam

When the foam is utilised as the sacrificial layer, it is inconvenient to e.g. use a bolt connection through the entire structure to keep it joined. Following some initial deformation of the sacrificial layer, i.e. the foam, it remains compacted and the assembly of the other layers might become inconveniently loose. Another problem may rise by using bolts through the entire structure, for huge pressures acting on the bolt tip, although its area is small, the resultant force may push the bolt into the structure. It is therefore necessary to couple the sacrificial layer to the rest of the panel by an adhesive or brazing of the foam sheet and the steel front plate/back plate, figure 9.6. The foam is bought from a manufacture, and is manufactured as stated in appendix C. The ARMOX steel plate is likewise bought from a manufacture, and is assumed manufactured as regular steel plates.

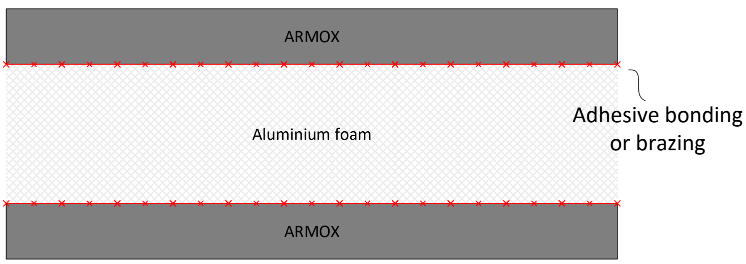

Figure 9.6: *A suggestion on an assembly of a panel consisting of front and back plate of ARMOX steel, and aluminium foam as core material.*

The weight of the steel plate and the foam core must be considered. During its life service, the plate undergoes vibrations and accelerations upwards or downwards which may cause a failure in the adhesive or brazing.

Micro-truss

For the micro-truss structure, the same problem regarding the permanent deformation and a resulting loose assembly exists. However, as the structure is either extruded and then wire electrical discharged, or punched, folded and then brazed, it has two face-sheets which permit bolt connections from opposite sides, figure 9.7. The unknown in this case is whether the front plate fall off after heavy deformation of the core structure as the beams might break. If this happens, the protection of the vehicle is greatly compromised. A concept of sort of a turnbuckle consisting of a wire to avoid the usual rod for being ejected into the cabin of the vehicle may be used in-between the armour panels. It both keeps the armour panels aligned, closing gaps between the panels, and it eliminates the possibility of the front plate of the panel falling off, figure 9.7.

As a rule of thumb in cases the bolt thread engages with the aluminium, the engagement length has to be two times the diameter of the bolt, to make sure the bolt, in case of failure, fails before the thread, [Norton, 2006]. For steel-steel, it is sufficient with one diameter length of engagement.

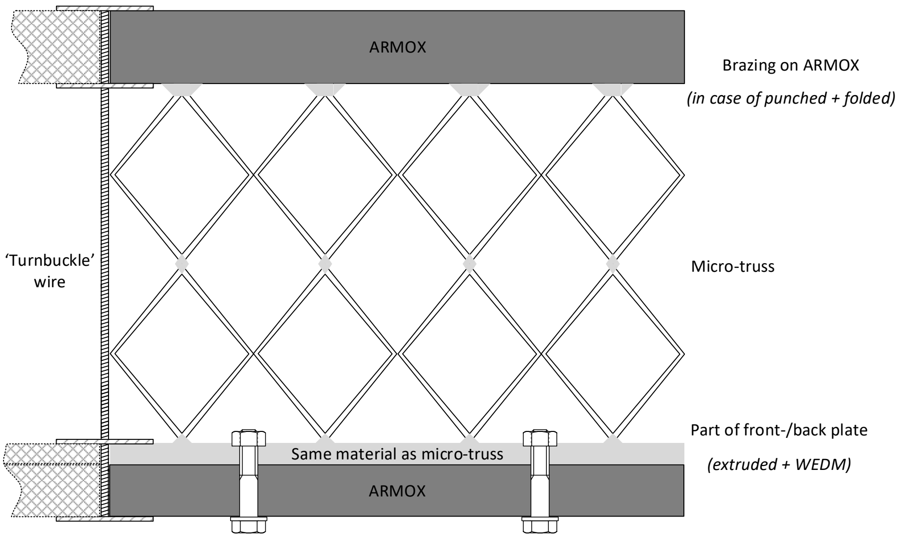

Figure 9.7: *A suggestion on an assembly of a panel consisting of the micro-truss structure. Dependent on whether the structure is punched from a plate, with additional folding, or whether the structure is extruded with additional wire electrical discharge machining (WEDM), the connection to the front and back plate is different. When possible, a bolt connection is used as these are very durable. A wire-turnbuckle concept may be used to keep the front plate of the panel attached after heavy deformation.*

Indentation sheet

The indentation sheet is similar to the micro-truss structure in permitting the use of bolt connections. As the indentation sheet solution consists of two sheets, it is possible to pull the sheets apart in tension, and this of course has to be opposed. This can be done with a small welding, or brazing, figure 9.8, and if this couplings breaks due to deformation, the wire-turnbuckle system might be implemented as well.

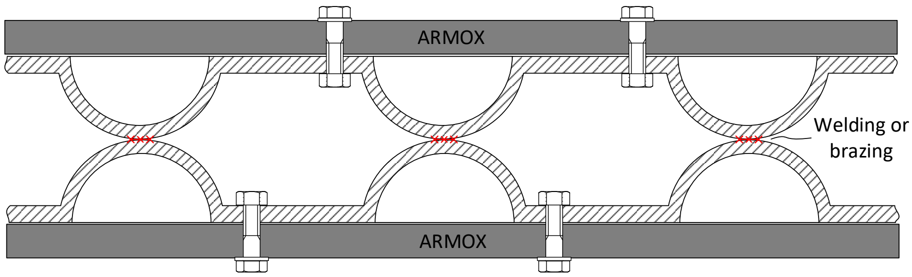

Figure 9.8: *A suggestion on the assembly of a panel consisting of the indentation sheet, and the disruptive layer of ARMOX as front plate, and a backing plate likewise of ARMOX. This structure permits the use of a bolt connection, which is very durable.*

9.3.2 The final panel

It is expected, that the test panel differs a bit from the final armour panel.

For the test panels, the backing plate is primarily there to provide a rigidity in the structure which ensures the deformation of the core structure as this is the primary test objective. A back plate may also increase the ballistic protection of the entire plate besides the possibility to incorporate mounting points so the panel can be attached to the chassis of the vehicle. The disadvantage of using a back plate is the increase in mass, without improving the blast protection, which as shown (chap. 6) is improved by increasing the mass of the buffer plate in front of the sacrificial layer. To reduce the mass of the back plate, a grid of ribs with thin face sheet can be used as a back plate. The ribs must have a cross section with high moment of inertia to provide the required stiffness.

Another change might be, as mentioned previously, that a steel front plate is insufficient ballistic protection, and Composhield might want to add a ballistic protection consisting of a fibre-ceramic composition. This can be added to the front of the amour panel, however the ground clearance will be reduced.

Additionally, the panel needs to be shaped to fit the underside of the vehicle, including the location of mounting points, improving wear resistance and avoid galvanic corrosion between the aluminium and steel. The corrosion can be avoided by an electrical insulator between the layers, e.g. a thin nylon sheet, and protection against water. However, aluminium and steel are not highly conductive towards each other but close contact such as the steel bolts into the aluminium may for good measure be galvanized.

A suggestion of a final assembly of a armour panel is made in figure 9.9.

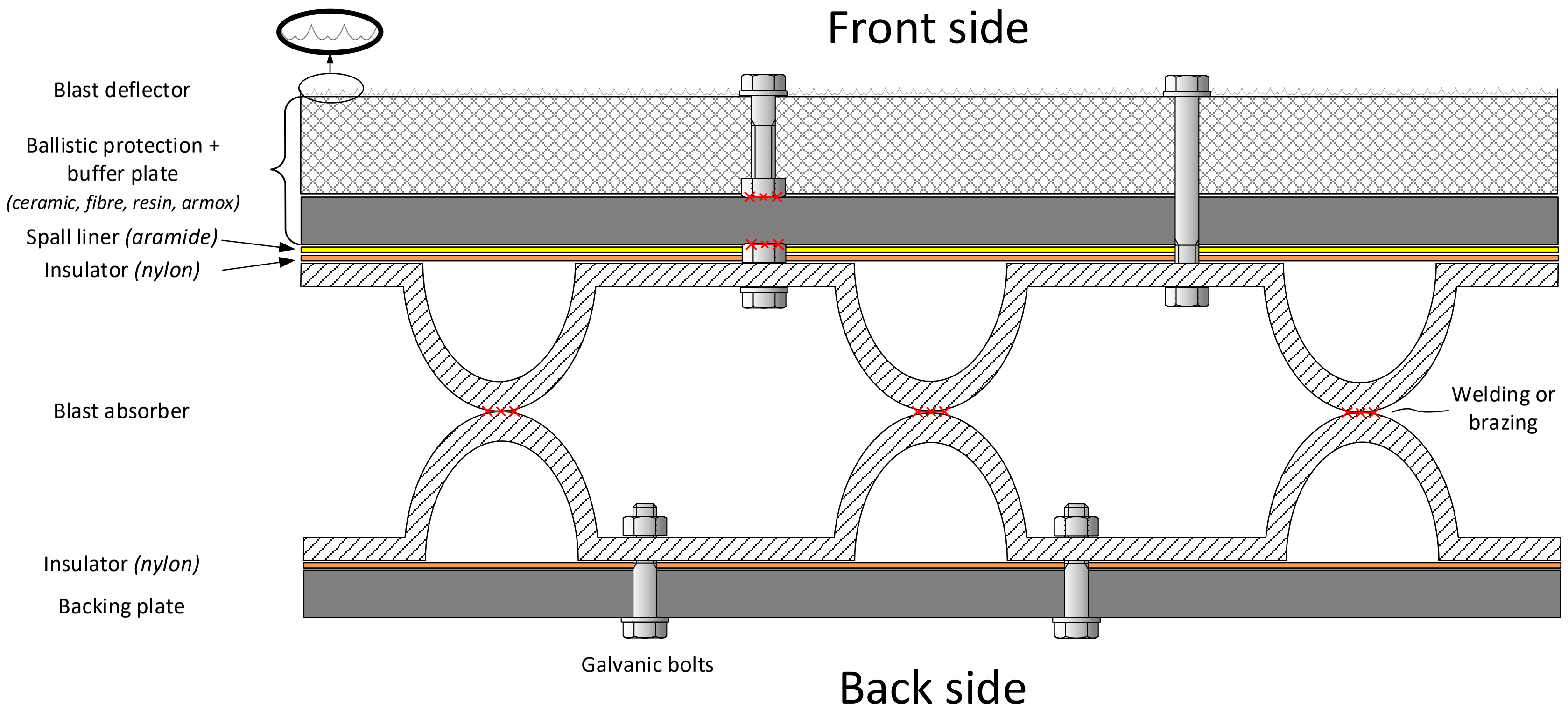

Figure 9.9: *A suggestion of the assembly of the final plate, including insulator, spall liner, blast absorber and deflector and possible bolt connections. A suggestion of a bolt connection is to weld a bushing on each side of the ARMOX plate, and then fasten the bolt into this one. This is if one wants to avoid drilling a hole in the ARMOX. A wire-turnbuckle concept may also be used to keep the front panel attached to the plate.*

10 Conclusion

The objective of this thesis was to develop an armour floor panel for protection against a blast threat. The floor panel was to be mounted on a HMMWV vehicle, and the blast threat came from a DM51 hand grenade. The project was proposed by Composhield A/S in an effort to enhance the blast protection of their armour solutions for the military industry. An aluminium foam and a suggestion of a sensible case load (DM51 grenade) were provided by Composhield with the desire of investigating the material properties of the aluminium foam before determining the possibility of using this material manufacturer in future products. This worked as a start for the project along with a study of the resulting blast loading following a detonation of the 0,0979 kg equivalent TNT in a DM51 hand grenade. By using a material such as this foam, it is possible to reduce the transmitted load through the floor onto the vehicle structure during a blast loading. This is achieved through energy absorption by the compaction of the foam. Analytical models describing deformation and affected parameters were developed and applied, along with numerical models. This yielded an in-depth understanding of the governing parameters. The material behaviour of the foam was inhomogeneous and at times disappointing why alternative concepts were studied. A variety of concepts were studied, and compared against the foam at all time. A promising concept better than the foam on multiple parameters was determined, but until the concepts have been experimentally validated, the final decision regarding the armour panel is not made. A proposal of the necessary experimental work was made and a part of this work is planned for the near future.

Thesis scope

Regarding the thesis scope, the following conclusions were achieved.

1) Determine the temporal and spatial distribution of the load in both the armour plate, and discrete fixation/mounting points.
A comprehensive understanding of blast parameters and their effects were obtained during this study. It was found, that a lot of the available literature are based on empirical data which are then scaled for specific cases using scaling laws. This means, that the blast data used in this thesis is based on similar equivalent data stored in the software ConWep. The pressure and impulse distribution and the effect of the different blast parameters investigated for the case, and an impulsive loading was assumed during the analytical study.

2) Investigate the metallic foam presently used in the composite armour plate for determining the energy absorbing properties and ability to withstand multiple blast waves.
Material tests were performed on the available closed-cell aluminium foam. The effect of variation in relative density was investigated and determined to be significant, see table 5.1. All parameters were obtained by the tests and it was noted that the foam has a relatively high plateau stress of 4,77 MPa. The ability of withstanding multiple hits can be achieved by controlling the foam thickness. However, it was concluded that better alternatives than the foam exists for a blast absorbing design, e.g. the micro-truss structure, figure 5.8(g).

3) Investigate the effect of geometry and/or composition of the armour plate for the Humvee floor on energy absorption, structural integrity etc.
Analytical models were developed and used for determining the deformation in the foam when exposed to the blast load. It was determined how the range and thereby the blast parameters govern the deformation profile; the buffer plate reduces the deformation and enhances the plate protection but increases the weight. Besides the pressure peak value, the eigenperiod of the plate and thereby the maximum deformation time must be accounted for in any design. Optimum design points were defined for minimum mass and minimum thickness.

4) Design the discrete energy absorption points for the assembly of the armour plate and the chassis.
This task has not been fulfilled fully, as it halfway through the project was decided to shift focus. However, the alternative structure, i.e. the micro-truss structure, is capable of acting as a mounting point between chassis and armour panel, as it can be modified for the specific needs. A parametric study conducted showed higher energy absorption capacity than the foam, and is seen from e.g. figure 5.8(g). The structure is suitable for additive manufacturing (3D-printing), and can thereby be shaped to avoid e.g. suspension arms etc. beneath the vehicle where e.g. a 4×4 micro-truss structure with less than half the foam thickness can sustain the same blast load.

5) Parametric study of the armour panel.
The design concept and the micro-truss structure were more or less determined by parametric studies. Investigating different designs and concepts showed a wide range of possibilities for developing and improving the design properties for blast protection, only the cost and manufacturing difficulties can be concerns of these designs. However, an improved and easily manufacturable design was achieved, see figure 8.14. The advantages are the ability to control the parameters, and the option of an optimization of the structure in future work. The final design was capable of reducing the transferred load to 40% of what is transferred by the aluminium foam of equivalent mass as shown in table 8.3.

6) Experimental validation.
The experimental work has unfortunately not been conducted in time. However, a plan for the near future experimental validation using the terminal ballistics laboratory was described in chapter 9. A plan for a live-blast tests was also described, but the prospect of these tests are very shallow. Until the experimental work has been conducted, all three of the concepts are maintained as it is desired to investigate all three of them experimentally.

Requirements

Regarding the requirements the indentation sheet concept achieved the following conclusions.

Blast threat. The concept is designed for protection of a blast load resulting from an explosion of a DM51 hand grenade. This means, the design has a classification of STANAG level 1 protection. This protection level can be higher by small modifications to the design such as; doubling the layers, optimization of parameters or using a different material.

Lightweight. The design concept is significantly lighter (only 52,8 kg/m^2 plus additional ballistic protection), than a concept using the aluminium foam and achieving the equivalent residual reaction force. Other armour floor panel solutions are unknown, why the only reference is the aluminium foam equivalent. For the same mass per unit area, the indentation sheet transfers a reaction force equal to only 40% of the reaction force transferred by the foam.

Ground clearance. The design is again significantly thinner than the equivalent foam design, why the indentation sheet performs better. An additional requirement is, that the armour panel can only reduce the ground clearance with 10% or 40 mm. As the blast absorbing layer is 26 mm, it leaves 14 mm room for additional ballistic or blast protection if this is needed.

Mountable. This requirement has not been treated very much, as the design of the fixation points, as stated earlier, was abandoned during the project. However, as stated in 9.3, the implementation of a rigid backplate permits the fitting of the mentioned fixation point, or any other mounting bracket one desire.

Environment. This requirement has likewise not been treated very much, but the methods of assembly suggested in sec. 9.3, consider the options for avoiding unnecessary gaps, resistant materials and galvanic corrosion.

It must be stated, that a greater blast load probably should have been chosen at an earlier stage, as the load from a hand grenade is exceedingly limited. However, the hand grenade was chosen as it produces a limited explosion and therefore controllable in a test-environment.

Suggested future work

The future work includes carrying out the experiments described in chapter 9. The live-blast test is not an option at the moment, but is, as stated, necessary to finally conclude which of the sacrificial layers and assembly methods are most capable of resisting the blast load.

The realisation of the armour panel, following the decision on the most suitable sacrificial layer, needs to be finished. This includes a correct method of assembly, integration of mounting brackets and securing the panel for wear resistant as it is in a very exposed location.

The panel needs to be designed for a greater STANAG certificate. A blast load from a hand grenade is nothing against modern IED's, and the scaling of the protective capabilities of the armour panel is unknown. Designing for STANAG level 2 certificate, tab. 3.2, is a possibility. This includes an anti-tank mine of 6 kg TNT exploding beneath the belly of the vehicle wheel. This is also comparable with the well-known IED's from Iraq consisting of old artillery shells, chapter 3.

A full solution including the ballistic part is also required as the buffer and back plates can be a part of the ballistic protection system.

"The bursting radius of a hand-grenade is always one foot greater than your jumping range."
— Unknown

Bibliography

Albertsson, H., S. Barrett, M. Dam, R. V. Christiansen, and A. Othman. 2015. Stress and Deformation Analysis of a Load Carrying Bracket. Technical report.

Alghamdi, A.. 2001. Collapsible impact energy absorbers: an overview. *Thin-Walled Structures 39*(2), 189 – 213.

AM General. 2017. http://www.amgeneral.com/. Accessed: 2017-02-07.

ANSYS Inc.. 2016. *ANSYS Release 17.2 Documentation*. www.ansys.com: ANSYS Inc.

Ashby, M. F., A. G. Evans, N. A. Fleck, L. J. Gibson, J. W. Hutchinson, and H. N. G. Wadley. 2000. *Metal Foams: A Design Guide*. ISBN: 978-0-750-67219-1. Butherworth-Heinemann.

Barrett, S., R. V. Christiansen, and A. Othman. 2016. Ballistic Properties of Projectile material. Technical report.

Bogoslovov, R. B. and C. M. Roland. 2007. Impact-induced glass transition in elastomeric coatings. *Applied Physics Letters 90*(22).

Brode, H. L.. 1977. Quick estimates of peak overpressure from two simultaneous blast waves. Technical report, DTIC Document.

Christensen, C. B. and E. L. Olesen. 2007. M.Sc.: Design of Lightweight HMMWV Door for Ballistic and Blast Protection. Technical report.

Davison, L.. 2008. *Fundamentals of Shock Wave Propagation in Solids*. ISBN: 978-3-540-74568-6. Springer.

Deshpande, V. and N. Fleck. 2001. Collapse of truss core sandwich beams in 3-point bending. *International Journal of Solids and Structures 38*(36–37), 6275 – 6305.

Gama, B. A., T. A. Bogetti, B. K. Fink, C.-J. Yu, T. D. Claar, H. H. Eifert, and J. W. G. Jr. 2001. Aluminum foam integral armor: a new dimension in armor design. *Composite Structures 52*(3–4), 381 – 395. Design and Manufacturing of Composite Structures.

Gibson, L. J. and M. F. Ashby. 1997. *Cellular solids: structure and properties* (2nd ed.). ISBN: 052-1-495-601. Cambridge University Press.

Global Security. 2017. http://www.globalsecurity.org/. Accessed: 2017-02-17.

Goel, M. D., V. A. Matsagar, S. Marburg, and A. K. Gupta. 2013. Comparative Performance of Stiffened Sandwich Foam Panels under Impulsive Loading. *Journal of Performance of Constructed Facilities 27*(5), 540–549.

Guruprasad, S. and A. Mukherjee. 2000. Layered sacrificial claddings under blast loading Part I — analytical studies. *International Journal of Impact Engineering 24*(9), 957 – 973.

Guzas, E. L. and C. J. Earls. 2010. Air blast load generation for simulating structural response. *Steel Compos. Struct 10*(5), 429–455.

Hanssen, A., L. Enstock, and M. Langseth. 2002. Close-range blast loading of aluminium foam panels. *International Journal of Impact Engineering 27*(6), 593 – 618.

HBM. 2017. https://www.hbm.com/. Accessed: 2017-05-19.

HBM-S8. 2017. http://www.hottinger.sk/Prospekty/Elektronika/IMT/Spider8/p_Spider8_e.pdf. Accessed: 2017-05-19.

Hoffmann, K.. 1989. *An Introduction to Measurement Using Strain Gages.* Hottinger Baldwin.

Jane's Information Group. 1996. *Jane's Ammunition Handbook* (5th ed.). ISBN: 978-0710613783. Jane's Information Group.

Johnson, G. R. and W. H. Cook. 1983. A constitutive model and data for metals subjected to large strains, high strain rates and high temperatures. *Proceedings of the 7th International Symposium on Ballistic*, 541 – 547.

Karagiozova, D. and N. Jones. 2000. Energy absorption of a layered cladding under blast loading. *Structures under Shock & Impact 6.*

Karlos, V. and G. Solomos. 2013. Calculation of Blast Loads for Application to Structural Components. Technical Report EUR 26456 EN.

Kingery, C. N. and G. Bulmash. 1984. Airblast parameters from TNT spherical air burst and hemispherical surface burst. Technical report, U.S. Army Ballistic Research Laboratory.

Kinney, G. and K. Graham. 1985. Explosive shocks in air. *Berlin and New York, Springer-Verlag, 1985, 282 p..*

Kranzlin, N. and M. Niederberger. 2015. Controlled fabrication of porous metals from the nanometer to the macroscopic scale. *Mater. Horiz. 2*, 359–377.

Kucherov, Y. R. and G. K. Hubler. 2014, 02. Patent: Blast wave effects reduction system. (US 8646373).

Needham, C. E.. 2010. *Blast Waves.* ISBN: 978-3-642-05287-3. Springer.

Nilsson, M.. 2003. Constitutive Model for Armox 500T and Armox 600T at Low and Medium Strain Rates. Technical Report FOI-R-1068-SE.

Norton, R. L.. 2006. *Machine Design An Integrated Approach.* 0-13-148190-8. Pearson.

NSA. 2012. STANAG 4569. NATO Standardization Agency.

Olurin, O. B., N. A. Fleck, and M. F. Ashby. 2000. Deformation and fracture of aluminium foams. *Materials Science and Engineering: A 291*(1–2), 136 – 146.

Queheillalt, D. T., Y. Murty, and H. N. Wadley. 2008. Mechanical properties of an extruded pyramidal latticetruss sandwich structure. *Scripta Materialia 58*, 76–79.

Randers-Pehrson, G. and K. Bannister. 1997. Airblast loading model for DYNA2D and DYNA3D. Technical Report ARL-TR-1310.

Roland, C. M., D. M. Fragiadakis, R. M. Gamache, C. B. Giller, and R. G. S. Barsoum. 2015, 06. Patent: Polymer Coatings with Embedded Hollow Spheres for Armor for Blast and Ballistic Mitigation. (US 20150377592 A1).

Smith, P. D. and J. G. Hetherington. 1994. *Blast and Ballistic Loading of Structures*. ISBN: 0-7506-2024-2. Redwood Books, Trowbridge.

Sriram, R., U. K. Vaidya, and J.-E. Kim. 2006. Blast impact response of aluminum foam sandwich composites. *Journal of Materials Science 41*(13), 4023.

SSAB Oxelösund AB. 2007, 10. *Data Sheet: ARMOX 500T*. www.ssabox.com: SSAB Oxelösund AB.

Stankiewicz, M., A. Popławski, P. Bogusz, R. Gieleta, and G. Sławiński. 2015. Experimental Evaluation of Energy Absorbing Properties of Selected Elastomer Materials. *KONES Powertrain and Transport 22*(3).

Szuladzinski, G.. 1940. *Formulas for mechanical and structural shock and impact*. ISBN: 978-1-4200-6556-5. Taylor and Francis Group, LLC.

Teeling-Smith, R. and G. Nurick. 1991. The deformation and tearing of thin circular plates subjected to impulsive loads. *International Journal of Impact Engineering 11*(1), 77 – 91.

Unified Facilities Criteria. 2008. *Structures to Resist the Effects of Accidental Explosions*. http://www.wbdg.org/ffc/dod: Unified Facilities Criteria.

Wagner, L. L., R. A. Ash, C. Arnett, A. Ashley, and A. Bruco. 2014, 01. Patent: Spall liners in combination with blast mitigation materials for vehicles. (WO 2014/007872 A2).

Yu, C. J., , T. Claar, H. H. Eifert, I. W. Hall, R. Franz, K. Leighton, and D. F. Hasson. 1999. Deformation energy absorption of metal foams at high strain rates. Proc Met Foam.

Yu, C. J., H. H. Eifert, I. W. Hall, R. Franz, and K. Leighton. 1998. Feasibility Study on Deformation Energy Absorption of Metal Foams at High Strain Rates. FC-DE Report No. DAAG55-98-K-0002.

Zhou, H., G. Ma, J. Li, and Z. Zhao. 2015. Design of Metal Foam Cladding Subjected to Close-Range Blast. *Journal of Performance of Constructed Facilities 29*(4).

Zukas, J. A. (Ed.). 2004. *Introduction to Hydrocodes*. ISBN-13: 978-0080443485. Elsevier Science.

A | Blast parameters following Kinney, Graham and Brode

The following appendix describe the methods of obtaining blast parameters using the methods of Kinney, Graham and Brode (KGB).

The air blast parameter equations presented in this section comprise a complete set of parameter equations from open literature sources. The equations are taken from [Kinney and Graham, 1985] and [Brode, 1977]. These equations are used in [Guzas and Earls, 2010] with some modifications where the equations used in this project are taken from [Guzas and Earls, 2010].

The duration time of the blast t_0 is given as

$$\frac{t_0}{W^{1/3}} = \frac{980\left[1+\left(\frac{Z}{0{,}54}\right)^{10}\right]}{\left[1+\left(\frac{Z}{0{,}02}\right)^{3}\right]\left[1+\left(\frac{Z}{0{,}74}\right)^{6}\right]\sqrt{1+\left(\frac{Z}{6{,}9}\right)^{2}}} \tag{A.1}$$

where t_0 in ms and Z is the scaled distance given in eq. 2.3.

Information about the peak overpressure in free air is also taken directly from [Kinney and Graham, 1985] and is defined as

$$p_{so} = 808\, p_{atm} \frac{\left[1+\left(\frac{Z}{4{,}5}\right)^{2}\right]}{\sqrt{\left[1+\left(\frac{Z}{0{,}048}\right)^{2}\right]\left[1+\left(\frac{Z}{0{,}32}\right)^{2}\right]\left[1+\left(\frac{Z}{1{,}35}\right)^{2}\right]}} \tag{A.2}$$

where p_{so} is the peak side-on overpressure in units of bars, and p_{atm} is the atmospheric pressure in bars (1 atm $\approx$ 1,013 bar).

Information regarding peak reflected overpressure, p_r, is much harder to find than for incident overpressure in the open literature. All sources that do include parameter information for reflected overpressure present data for the normally reflected case, with angle of incidence effects treated separately, if at all. In the far field limit for explosions of any size, or for small explosions, the air can be treated as an ideal gas in order to establish a relationship between the peak side-on overpressure and peak reflected overpressure at a surface. According to [Brode, 1977], this relationship is

$$p_r = p_{so}\left(2 + \frac{6\, p_{so}}{p_{so} + 7\, p_{atm}}\right) \qquad \text{for } p_{so} < 6{,}9 \text{ bar} \tag{A.3}$$

where p_r is the maximum overpressure for normal reflection, p_{so} is the peak side-on overpressure, and p_{atm} is the ambient air pressure and all pressures in bar. An implicit assumption in this equation is that $\gamma = 1{,}4$, where γ is the heat capacity ratio of the air medium. When overpressure values exceed 6,9 bar, molecules in the air start to interact with one another and the ideal gas assumption is no longer valid. For this regime, [Brode, 1977] defines the peak normally reflected overpressure as

$$p_r = p_{so}\left(\frac{38{,}51\,p_{so}}{1+25{,}1\,p_{so}\cdot 10^{-4}+4\cdot 10^{-7}\,{p_{so}}^2}+\frac{2}{10^3}\right.$$
$$\left.+\frac{4{,}218+701{,}1\,p_{so}+1{,}44\,{p_{so}}^2}{1+0{,}116\,p_{so}+8{,}1\cdot 10^{-4}\,{p_{so}}^2}\right)\cdot 10^3 \quad \text{(A.4)}$$

for $p_{so} \geq 6{,}9$ bar which is again the peak side-on overpressure in bars.

The following equations for arrival time and decay constant are developed in [Guzas and Earls, 2010] by fitting piecewise polynomials to data for a 1 kg TNT reference explosion in [Kinney and Graham, 1985]. The data include arrival times and decay coefficients over a range of scaled distances. The resulting expression for the arrival time is

$$\frac{t_A}{W^{1/3}} = \sum_{i=1}^{4} a_i\ Z^{i-1} \qquad \text{where } 0{,}3 \leq Z \leq 500 \text{ m/kg}^{1/3} \quad \text{(A.5)}$$

where t_A is the arrival time, in seconds, of the shock wave initiated by an air blast. Values for the fitted polynomial coefficients, a_i, are included in table A.1 for various ranges of Z.

Range $\left(\text{m/kg}^{1/3}\right)$	a_0	a_1	a_2	a_3
$0{,}3 \leq Z < 2{,}4$	$1{,}77\cdot 10^{-2}$	$-2{,}03\cdot 10^{-2}$	$5{,}39\cdot 10^{-1}$	$-3{,}01\cdot 10^{-2}$
$2{,}4 \leq Z < 12$	$-2{,}25\cdot 10^{0}$	$1{,}77\cdot 10^{0}$	$1{,}14\cdot 10^{-1}$	$-4{,}07\cdot 10^{-3}$
$12{,}4 \leq Z \leq 500$	$-6{,}85\cdot 10^{0}$	$2{,}91\cdot 10^{0}$	$9{,}47\cdot 10^{-5}$	$-9{,}34\cdot 10^{-8}$

Table A.1: *Fitted polynomial coefficients to define the arrival time [Guzas and Earls, 2010].*

A higher order of polynomial is required to produce an accurate fit for the decay constant over the range of scaled distances, especially for smaller scaled distances. The decay constant follows this relationship

$$b = \sum_{i=1}^{6} c_i\ Z^{i-1} \qquad \text{where } 0{,}3 \leq Z \leq 500 \text{ m/kg}^{1/3} \quad \text{(A.6)}$$

where b is the dimensionless decay constant for side-on air blast. Values for the fitted polynomial coefficients, c_i, are shown for different ranges of Z in table A.2.

The decay constant is determined from the positive phase impulse, or the area under the pressure time history curve, for either side-on or reflected blast. [Guzas and Earls, 2010] assume similarity between time histories of side-on overpressure and normally reflected overpressure, demonstrated by

$$\frac{i_r}{i_s} = \frac{p_r}{p_{so}} \quad \text{(A.7)}$$

which means that the decay constant can be used interchangeably for side-on and normally reflected cases.

Range $\left(\mathrm{m/kg}^{1/3}\right)$	c_0	c_1	c_2	c_3	c_4	c_5
$0{,}3 \leq Z < 0{,}95$	$3{,}08 \cdot 10^{2}$	$-2{,}15 \cdot 10^{3}$	$5{,}95 \cdot 10^{3}$	$-8{,}23 \cdot 10^{3}$	$5{,}69 \cdot 10^{3}$	$-1{,}57 \cdot 10^{3}$
$0{,}95 \leq Z < 2{,}4$	$1{,}76 \cdot 10^{1}$	$-2{,}68 \cdot 10^{1}$	$1{,}79 \cdot 10^{1}$	$-5{,}66 \cdot 10^{0}$	$6{,}94 \cdot 10^{-1}$	0
$2{,}4 \leq Z < 6{,}5$	$4{,}43 \cdot 10^{0}$	$-2{,}72 \cdot 10^{0}$	$7{,}42 \cdot 10^{-1}$	$-9{,}34 \cdot 10^{-2}$	$4{,}47 \cdot 10^{-3}$	0
$6{,}5 \leq Z < 40$	$7{,}12 \cdot 10^{-1}$	$-6{,}27 \cdot 10^{-2}$	$3{,}33 \cdot 10^{-3}$	$-8{,}24 \cdot 10^{-5}$	$7{,}62 \cdot 10^{-7}$	0
$40 \leq Z \leq 5000$	$2{,}52 \cdot 10^{-1}$	$-1{,}77 \cdot 10^{-3}$	$9{,}52 \cdot 10^{-6}$	$-2{,}20 \cdot 10^{-8}$	$1{,}79 \cdot 10^{-11}$	0

Table A.2: *Fitted polynomial coefficients to define the decay coefficient [Guzas and Earls, 2010].*

B | Procedure followed to obtain the blast parameters in ConWep

This appendix describes the steps to obtain the blast parameters and stress distribution for the studied case. All graphical data, references and plots used to obtain the results in chapter 4 are stated here.

Determine hemispherical blast wave parameters at any point of the target plate.

The case where a hand grenade explodes under a vehicle can be represented as a surface burst located on the ground surface with a target plate parallel to the ground and suspended in the air above the detonation point as can be seen in figure B.1.

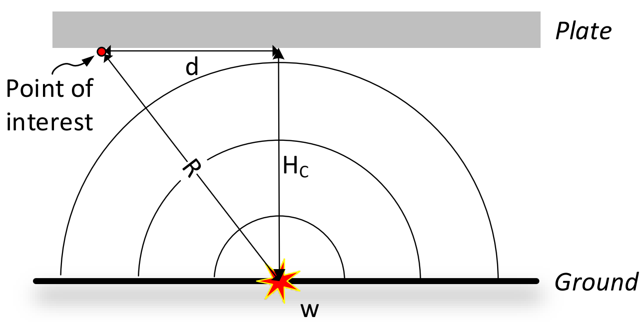

Figure B.1: *Load case set up, protective plate located horizontally to the ground above an explosive charge. Hemispherical air burst.*

To determine the blast parameters for a hemispherical burst (surface burst), the following steps from [Unified Facilities Criteria, 2008] are applied:

1. Determine the charge weight W, the distance R between the point of interest, the charge center, and H_c the normal distance between the charge center and the target plate.

2. Apply 20% safety factor to the charge weight.

3. Calculate the scaled distance Z and the angle of incidence α.

$$Z = \frac{R}{W^{1/3}} \tag{B.1}$$

$$\alpha = \tan^{-1}\left(\frac{d}{H_c}\right) \tag{B.2}$$

4. Use figure B.2 to obtain blast parameters for the point of interest based on the scaled distance Z.

5. Use figure B.3 with interpolation techniques to obtain the reflected pressure coefficient C_r at the angle of incidence α based on the side-on pressure p_{so} value which was determined in the previous step, where

$$C_r = \frac{p_{r\alpha}}{p_{so}} \tag{B.3}$$

6. Use figure B.4 with interpolation techniques to obtain the reflected scaled impulse associated with α.

7. Discretize the target plate to a sufficient number of points and calculate the blast parameters for all points to obtain the distribution of any parameter over the plate.

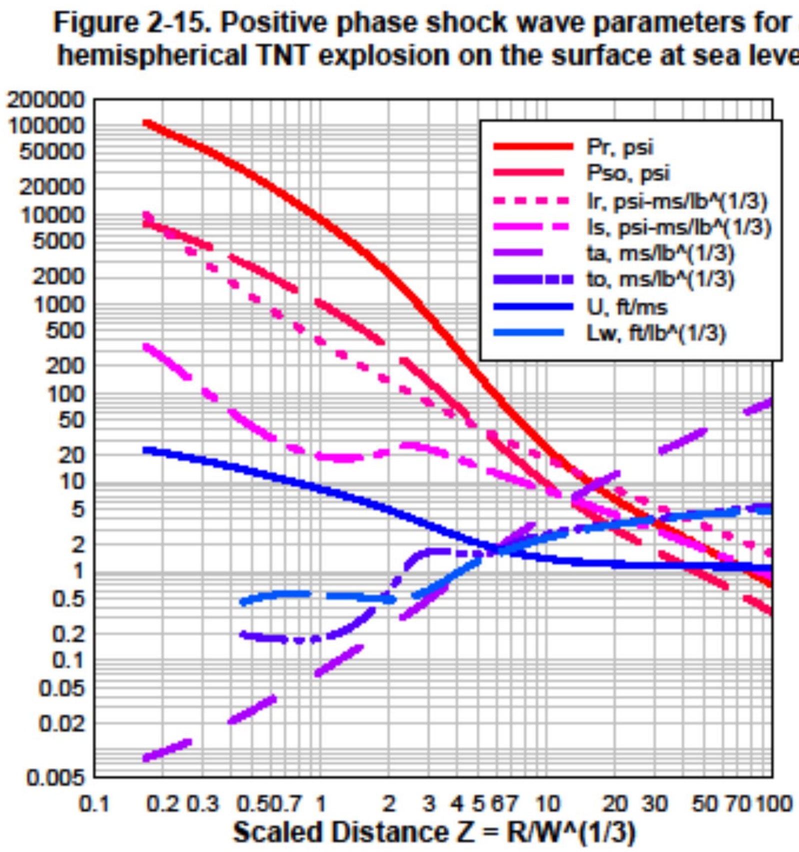

Figure B.2: *Positive phase shock wave parameters for a hemispherical TNT explosion on the surface at sea level. [Unified Facilities Criteria, 2008].*

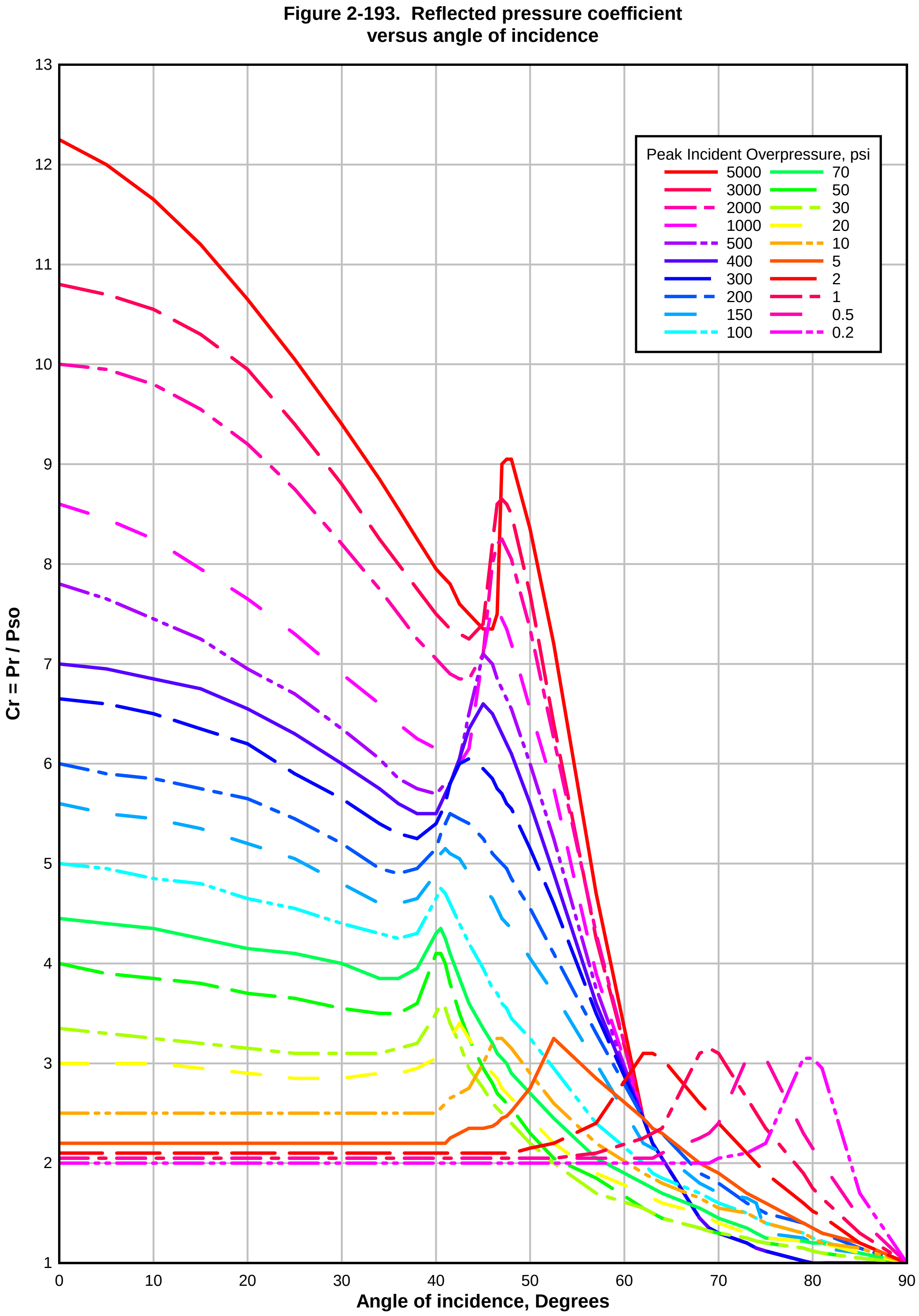

Figure B.3: *Reflected pressure coefficient versus angle of incidence. [Unified Facilities Criteria, 2008].*

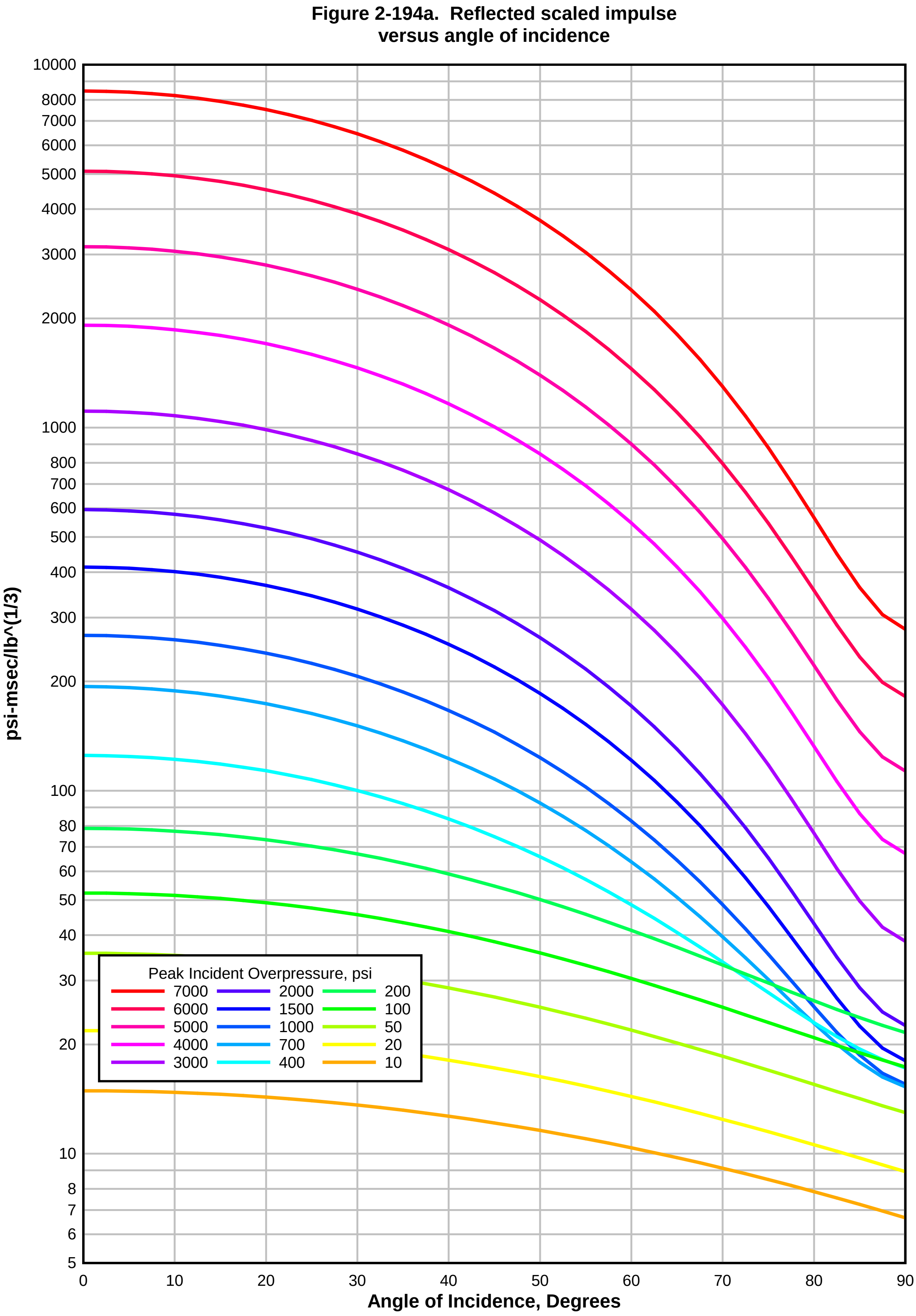

Figure B.4: *Reflected scaled impulse versus angle of incidence. [Unified Facilities Criteria, 2008].*

Blast Parameters distribution for the studied target

An application of the previous steps yields the results needed for all blast parameters and their distribution over all the plate. These results define the actual load case for the target plate and thereby lead to a proper design.

For (1 × 1) square plate where; $W = 1{,}2 \times 0{,}0979$ kg and $H_c = 0{,}5$ m, the blast parameters are obtained. Reflected pressure distribution is shown in figure B.5 and the reflected impulse distribution is shown in figure B.6.

Note that the technical manual [Unified Facilities Criteria, 2008] uses the US units system as can be seen in the figures. However all results obtained are transferred into SI units in this report.

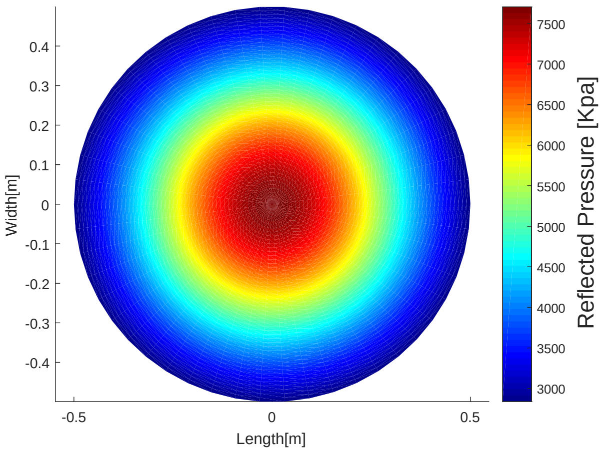

Figure B.5: *Reflected pressure distribution over the target plate.* $W = 0{,}1175$ kg, $R = 0{,}5$ m.

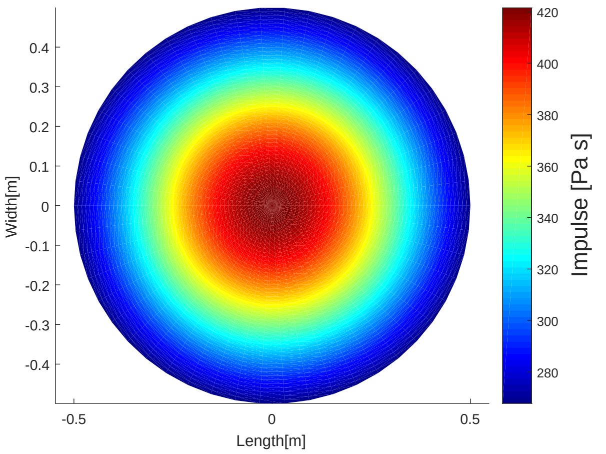

Figure B.6: *Reflected impulse distribution over the target plate.* $W = 0{,}1175$ kg, $R = 0{,}5$ m.

C | Aluminium foam material test

The following appendix describe the material test of the aluminium foam used in the project. The solid material of the foam is 5556 aluminium, and the plate has an average density of 458 kg/m^3, including the skin from the manufacturing process, and a poisson ratio of ≈ 0.

Purpose

To determine the mechanical properties of the aluminium foam, including:

- Compressive stress-stain curve
- Modulus of elasticity
- Densification strain/point
- Anisotropy

Procedure

Cylindrical test specimens are manufactured from a plate with a thickness of 30 mm. The cylinders are 30 mm long and have a diameter of 25 mm. The diameter is chosen to be less than the thickness as to avoid skin effects from the top and bottom in the specimens in the internal directions. The cylinders are cut a minimum distance of 20 mm from the edges of the plate to avoid skin effects, and in three orientations to investigate anisotropy, figure C.1.

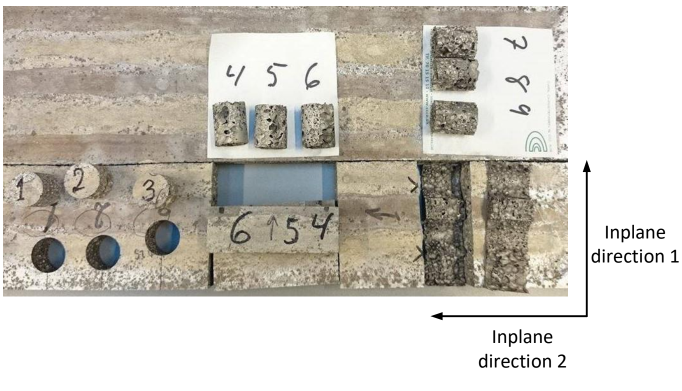

Figure C.1: *Aluminium foam plate, and the orientation of the cylindrical test specimens.*

Furthermore, slab specimens are manufactured as well. These vary in size and are beside the normal compression test used to test for variation in density and the effect from this, along with size effects and determination of the modulus of elasticity.

All specimens are manufactured by wire electrical discharge machining to avoid effects due to cutting tools.

The specimens are compressed in a standard test machine at quasi-static strain rate, usually defined as between $10^{-3} - 10^{-2}$ s^{-1}. Load and deformation are recorded. For the cylindrical specimens, each orientation is tested three times. The compression plates are coated with slip lacquer for reducing the friction.

The tests are terminated after a compression of 25 mm, or when the load of 85 kN is reached, for protection of the 100 kN load cell in the test machine. The instantaneous strain rate can be determined as

$$\dot{\varepsilon} = \frac{v}{l} \tag{C.1}$$

where v is the compression velocity and l is the instantaneous length. By reformulating eq. C.1 the velocity can be determined for the two extremes of the specimen length, 5 mm and 30 mm. Taking strain rate to 10^{-2} s^{-1} yields velocities of 3 and 18 mm/min. To reduce the time spent the velocity is set to 10 mm/min, this yields a maximum strain rate of $3{,}33 \cdot 10^{-2}$ s^{-1} which is considered quasi static.

Approach:

- Slab specimens are dried at 90° for two hours to remove any residual water from the machining from the cells.
- Specimen is placed in the test machine.
- Upper compression plate moves down with a velocity of 10 mm/min.
- When the test machine detects a load of 10 N/50 N, for the cylindrical and slab specimens respectively, the recording of deformation begins.
- When the compression plates are 5 mm apart (compression of 25 mm) or the load reaches 85 kN the test is terminated and the machine moves back to start position.
- Load-Deformation data is saved from the test machine.
- Data from the test machine are treated to determine stress and strain.

Results and discussion

Table C.1 shows the dimensions, weight and density of the slab specimens. The stress-strain curve for the slab specimens are shown in figure C.2.

The expected dependency on density is seen for the test specimens in figure C.2. Furthermore, the majority of the specimen show somewhat a plateau region with only a slight slope until the densification point/strain and a drastic change of slope. The densification strain is in an average determined as $\varepsilon_D = 0{,}48 \pm 0{,}0504$ by determining the point at which the slope of the curve in the end of region 2 is a third of the slope in region 1.

Test specimen no.	Weight		Dimensions		Density	
† 1	55,4	g	49,59 x 50,09	mm	743,4	kg/m^3
2	36,7	g	49,87 x 50,32	mm	487,5	kg/m^3
3	33,1	g	49,73 x 50,44	mm	439,9	kg/m^3
4	49,6	g	50,59 x 74,75	mm	437.2	kg/m^3
5	47,6	g	50,82 x 74,76	mm	419,5	kg/m^3
6	38,0	g	49,36 x 49,73	mm	516,0	kg/m^3
7	18,7	g	24,69 x 49,45	mm	510,5	kg/m^3
8	20,0	g	24,75 x 49,53	mm	543,8	kg/m^3
9	16,7	g	24,64 x 49,52	mm	456,2	kg/m^3
10	44,6	g	45,61 x 74,74	mm	436,1	kg/m^3
11	27,6	g	49,81 x 49,72	mm	371,5	kg/m^3
12	30,1	g	49,92 x 49,77	mm	403,8	kg/m^3
Avg. density for specimens:						
(with skin)					478,9±92,60	kg/m^3
(without skin)					456,5±49,98	kg/m^3
Density of plate:					458	kg/m^3

Table C.1: *Data on the slab specimen. Thickness: 30 mm. †: A single side was covered in skin from the manufacturing. A relative great variation in the density of the foam from different parts of the plate is observed.*

The modulus of elasticity is determined from the unloading curve, following a small plastic deformation of the order of 1%, following guidelines in [Olurin et al., 2000], as this is a more consistent representation of the elasticity due to cell collapses. An average of three measurements for both the loading and the unloading is given in eq. C.2 and shown in figure C.3(b).

$$E_{loading} = 183 \pm 88{,}3 \text{ MPa} \qquad E_{unloading} = 336 \pm 48{,}8 \text{ MPa} \tag{C.2}$$

The strain energy density and specific strain energy are determined for an average stress-strain curve. The energies are from zero to densification strain and given in eq. C.3.

$$u = 2{,}19 \pm 0{,}573\,\text{MJ/m}^3 \qquad e = 4737 \pm 1324\,\text{J/kg} \tag{C.3}$$

The average stress-strain curve is obtained by taking the average stress of all specimens, except specimen 1, at uniform strain intervals. This curve is used for representing the material in simulations. The average stress-strain curve is shown in figure C.3(a).

It is seen from figure C.3(a) that there are no clearly defined plateau stress. For analytical estimates and calculations an average value is used for simplicity, the average is taken from the end of the linear region onto the densification strain and is determined to $\sigma_{plateau} = 4{,}77 \pm 2{,}18$ MPa.

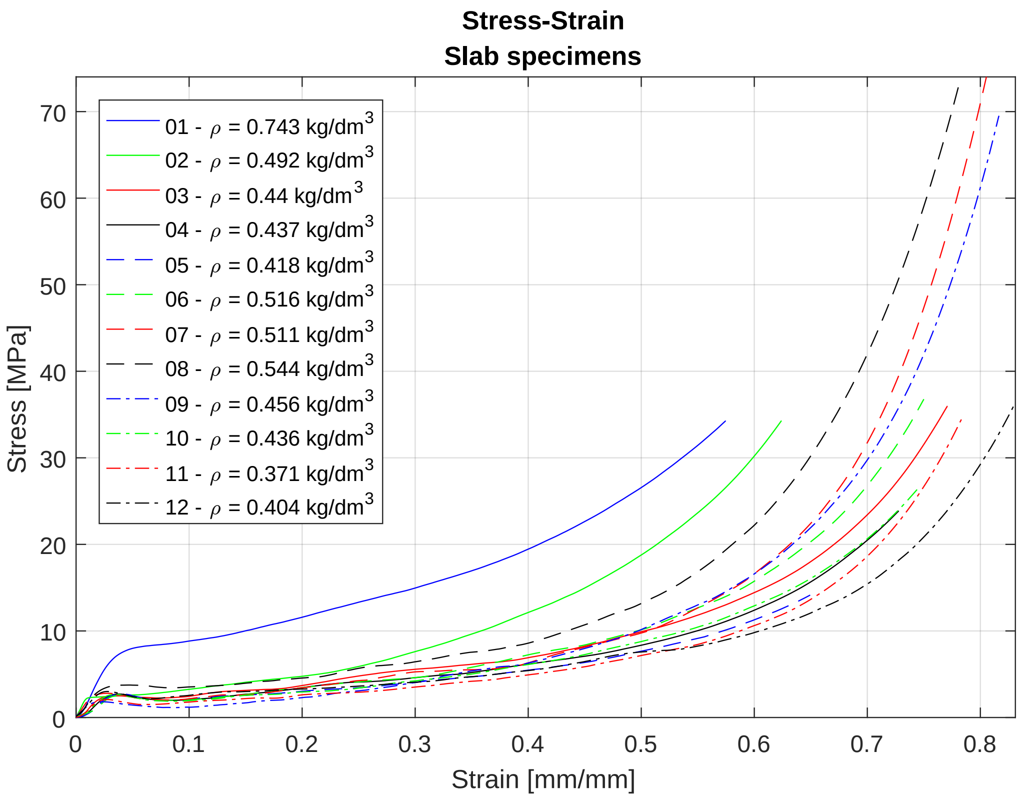

Figure C.2: *Stress-strain curve for the slab specimens as a function of density. Notice specimen 12, 4, 6 and 8 for general tendency of density effect (increasing density). Notice, specimen 1 has a single side with skin, hence the outlier.*

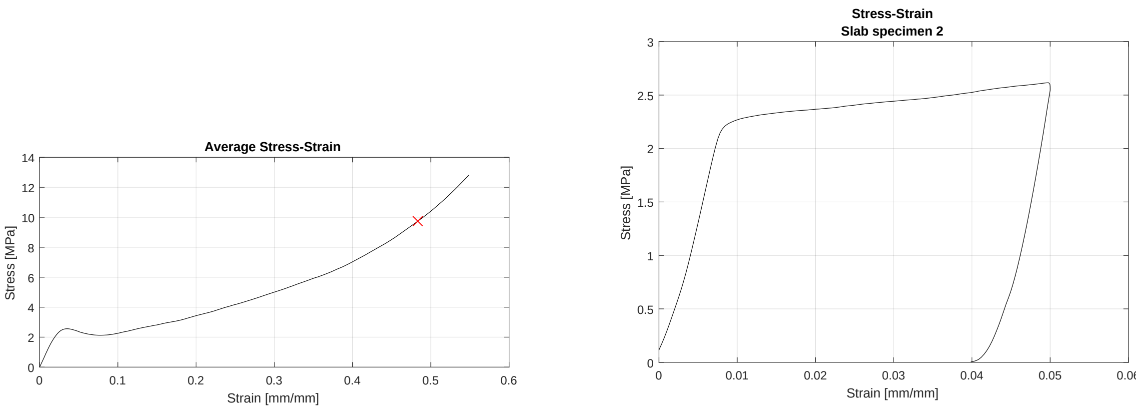

(a) The averaged stress-strain curve used for simulations. The red x marks the densification strain.

(b) A single cycle on slab specimen 2. There is a difference in the slope of the loading and unloading part of the test.

Figure C.3

As it is clear that the stress-strain relation and density varies from specimen to specimen it is attempted to determine a stress-strain-density relation. To determine whether such a relation exist it is investigated if there is a correlation between densification strain and density, and strain energy density and density. These are plotted in figure C.4.

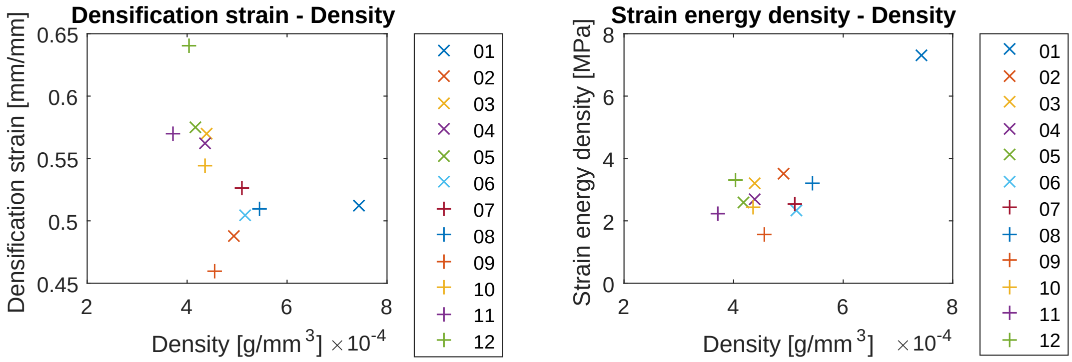

(a) Densification strain with respect to density.

(b) Strain energy density with respect to density.

Figure C.4

It can be observed from figure C.4 that there are no clear correlation between neither densification strain and density, or strain energy density and density. Figure C.4(a) may give the impression of a slight correlation but this is mainly due to specimen 1 and 12 which both had skin on one side. From this and additional attempts no expression between density and any other mechanical properties are found.

And, the stress-strain curve for the cylindrical specimens are shown in figure C.5.

As is seen from figure C.5 there are quite large differences between the test specimens. It is however difficult to conclude whether this is due to anisotropy as it is observed that there are large differences in the structure of the foam specimens, ranging from dense uniform cell structure to large voids, figure C.6. Furthermore, the specimens in the same orientation, except for the 'through-the-thickness (blue)', deviate significantly and the slight anisotropy which may exists is negligible compared to this density effect.
It is also observed that the specimens contain water from the machining process, the water is attempt removed by simple drying but the specimens still excrete water during the compression. The strain rate at which the test is performed should however permit a steady flow of water from the cell, without drastically increasing the internal pressure of the cell and thereby hamper the collapse of these. It is however rectified for the slab specimens for good measure.

The expected behaviour of the foam, including a plateau of near constant stress and a densification point, are observed in all the specimens.

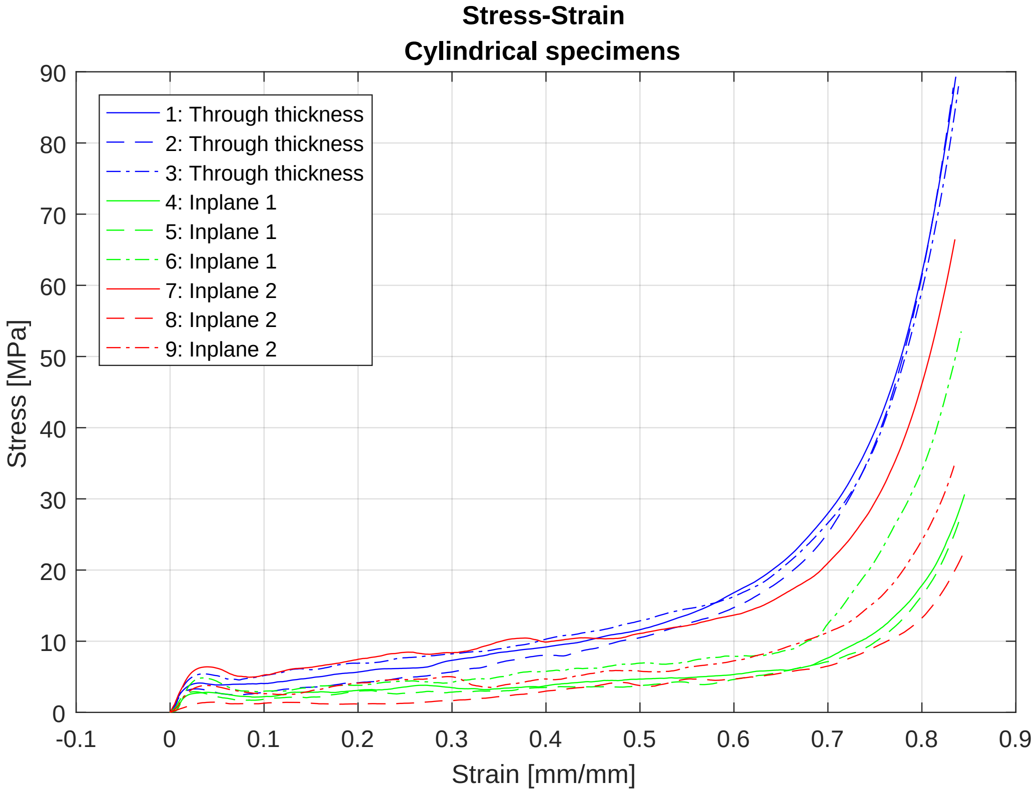

Figure C.5: *Stress-Strain curves from compression test of the cylindrical specimens. 1-3 are Ø25 mm through the thickness, 4-6 and 7-9 are Ø25 mm in internal directions.*

(a) Unevenness of cell sizes.

(b) An example of cavities.

(c) Another example of cavities.

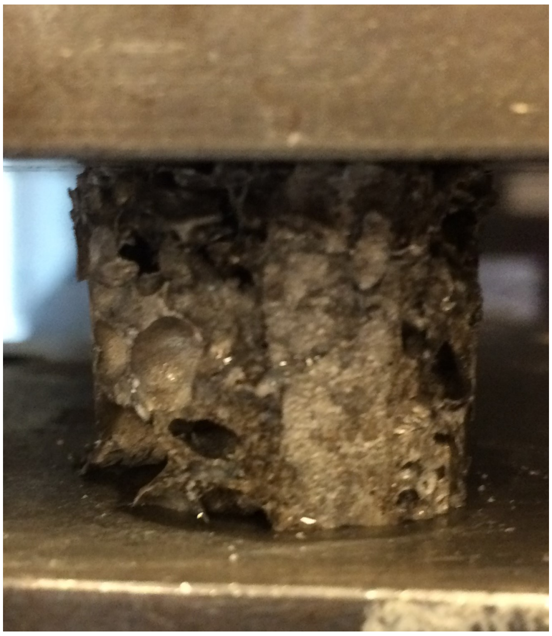

(d) Excreted water during compression.

Figure C.6

Manufacturing of aluminium foam

Five different methods of making metal foams are established commercially and can be divided into four classes: foam is formed from a vapour phase; foam is electro-deposited from an aqueous solution; from liguid-state processing; and when the foam is created from a solid state, [Ashby et al., 2000]. The main differences of the methods are whether the foam topology is open-cell or closed-cell, and the difference in quality and thereby cost.

The available Alulight is manufactured from consolidation of metal powder added a foaming agent, i.e. solid state. This agent is unknown, but is commonly titanium hydride (TiH_2) according to [Ashby et al., 2000], which releases the hydrogen when heated, and thereby creating the cells. Titanium hydride starts to decompose into Ti and H_2 when heated to 465 °C. The melting point of pure aluminium is 660 °C or thereabout for its alloys, [Ashby et al., 2000]. A foam is thereby created, by heating the powders to a temperature somewhere in-between to release the hydrogen and allow bubble growth in the partially melted/mushy aluminium (alloy). These voids have a high internal pressure, and disperse in the aluminium as it swells to fill the mold creating the foam. This is followed by a cooling procedure which stabilizes the shape of the foam. Usually, the diameter of the closed-cells following this procedure is Ø1 - 5 mm. [Ashby et al., 2000].

The foaming process using a powder metallurgy method creates a solid skin, which can be used for surface bonding to other materials, yields a high specific strength and a distinct non-linear behaviour in compression, [Gama et al., 2001].

D | Model for calculating foam thickness for blast loaded structure

The following appendix presents an analytical model developed by [Hanssen et al., 2002] of an aluminium foam bar in an effort to obtain a sound physical understanding of the mechanics governing the deformation of the stated foam and determine an expression for determining the necessary thickness of the foam for avoiding complete densification during an explosion and thereby direct transfer of the blast load into the structure.

The model is based on the work in [Hanssen et al., 2002] for determining the one-dimensional deformation in an aluminium foam bar under the assumption of a linearly decaying blast load.

The model is shown in figure D.1 and consists of a foam bar covered by a front panel of mass m_p and area A loaded by a blast loading $p(t)$ while it is fixed to a rigid wall in the distal end. Note, that $p(t)$ does not account for spatial distribution, i.e. a reduction in magnitude as the foam bar deforms and thereby increases the distance to the source of the blast is not accounted for, [Hanssen et al., 2002]. Furthermore, the model is of single-degree-of-freedom (SDOF), and hereby does not include bending, shear, and membrane effects of the front plate.

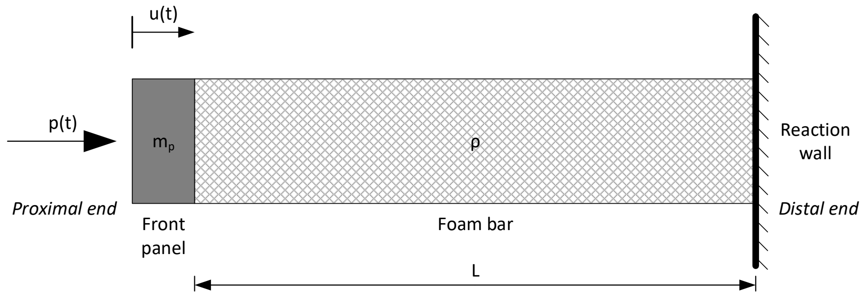

Figure D.1: *1D model system of foam bar with front panel undergoing a blast load. The bar is of length L, cross-sectional area A and mass $m_f = \rho\, A\, L$. The deformation of the bar is given by $u(t)$. [Hanssen et al., 2002].*

The front panel is considered as rigid, and the foam bar is considered as a r-p-p-l material (rigid-perfect-plastic-locking) of strength σ_{pl}, i.e. the plateau stress. The r-p-p-l model behave as a rigid perfect plastic material until the densification strain of ε_D is reached where the material 'locks' into a rigid solid and behaves as shown in figure D.2, [Hanssen et al., 2002].

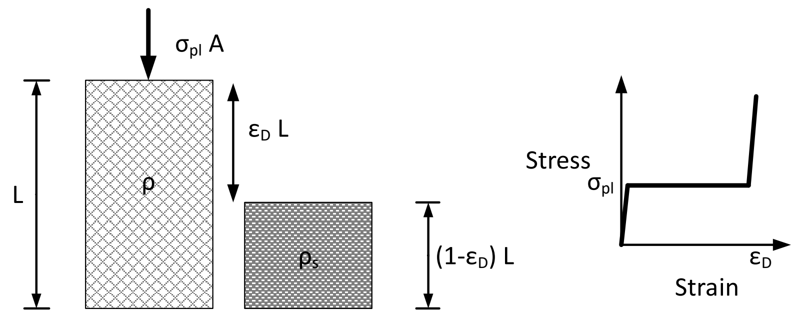

Figure D.2: *Definition of the r-p-p-l material model.* ρ_s *is the density of the solid material. [Hanssen et al., 2002].*

In figure D.3 the model system at time t and $t + dt$ is shown. The foam bar starts deforming in the loaded end/proximal end, and a densification front moves through the material resulting in the left part of the foam becoming completely densified achieving the same velocity as the rigid front panel, whereas the remaining right part is not affected by this deformation, [Hanssen et al., 2002]. However, due to the stiffness of the material, a near-instantaneous propagation of a stress wave (at time $t = 0$) from the proximal end to the distal end has increased the stress in this part to σ_{pl} yielding a reaction wall force of σ_{pl} A. The densification front keeps proceeding as long as the necessary energy is supplied, as the plastic compression of the foam consumes kinetic energy, increasing the size of the compacted region, [Hanssen et al., 2002].

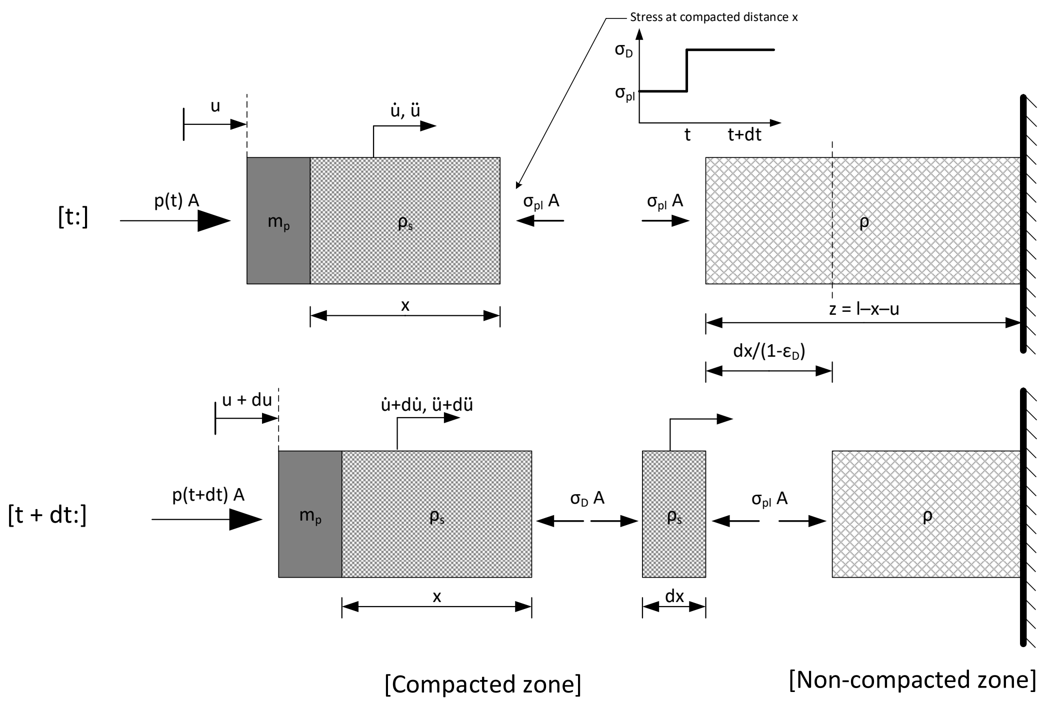

Figure D.3: *FBD at time t and $t + dt$. [Hanssen et al., 2002].*

Using conservation of mass, and the size of the compacted zone x and the displacement of the front panel u for time t is

$$u = \frac{\varepsilon_D}{1-\varepsilon_D}\, x \tag{D.1}$$

Using figure D.3, consider the element of length $dx/(1-\varepsilon_D)$ in the non-compacted zone directly in front of the compacted zone. At time t, the stress at both sides of the element is σ_{pl}. A time increment later, $t+dt$, the element has undergone a compression and has the velocity $\dot{u}+d\dot{u}$. To accelerate this element, the stress on the left side instantaneously increases to σ_D at time t. In the time interval of t to $t+dt$, the impulse from the forces has to equal the change in momentum of the element, [Hanssen et al., 2002].

$$\rho_s\, A\, dx\, (\dot{u}+d\dot{u}) = (\sigma_D - \sigma_{pl})\, A\, dt \tag{D.2}$$

Assuming that the second order term $dx\, d\dot{u}$ is negligible, then by dividing with dt and taking the limit $dt \to 0$

$$\sigma_D = \sigma_{pl} + \frac{\rho}{1-\varepsilon_D}\, \dot{x}\, \dot{u} \qquad\qquad \text{note } \rho_s = \frac{\rho}{1-\varepsilon_D} \tag{D.3}$$

where the relation of density between the solid/compacted part and the foam part is given in figure D.2.

Similarly, the conservation of momentum (Newton 2nd) for the front panel and compacted region (rigid body) to the left of the element dx gives

$$\left[m_p + \frac{\rho\, A}{1-\varepsilon_D}\, x\right] \ddot{u} + (\sigma_D - p(t))\; A = 0 \tag{D.4}$$

By combining eqs. D.1, D.3 and D.4, a single differential equation is obtained

$$\left[1 + \frac{\rho\, A}{m_p\, \varepsilon_D}\, u\right] \ddot{u} + \frac{\rho\, A}{m_p\, \varepsilon_D}\, \dot{u}^2 + (\sigma_{pl} - p(t))\, \frac{A}{m_p} = 0 \tag{D.5}$$

which states that the change in momentum for the bar has to equal the impulse from the external forces, i.e. blast load and reaction force, [Hanssen et al., 2002].

The pressure of the blast loading is defined as

$$p(t) = \begin{Bmatrix} p_0 \left(1 - \frac{t}{t_0'}\right), & t \leq t_0' \\ 0, & t > t_0' \end{Bmatrix} \tag{D.6}$$

where p_0 is the initial peak pressure and t_0' is the equivalent triangular duration of the blast loading.

The initial conditions are

$$u(0) = 0 \qquad\qquad \dot{u}(0) = 0$$

and the complete solution then becomes[1]

$$
\begin{aligned}
&\frac{u}{\varepsilon_D\, L} = 0 && t \leq 0 \text{ or } \frac{p_0}{\sigma_{pl}} \leq 1,\\
&\frac{u}{\varepsilon_D\, L} = -m + \sqrt{m^2 + 4\xi\left\{\left(1-\frac{\sigma_{pl}}{p_0}\right)\left[\frac{t}{t_0'}\right]^2 - \frac{1}{3}\left[\frac{t}{t_0'}\right]^3\right\}} && 0 < t \leq t'_0 \text{ and } \frac{p_0}{\sigma_{pl}} > 1,\\
&\frac{u}{\varepsilon_D\, L} = -m + \sqrt{m^2 + 4\xi\left\{-\frac{1}{3} + \left[\frac{t}{t_0'}\right] - \frac{\sigma_{pl}}{p_0}\left[\frac{t}{t_0'}\right]^2\right\}} && t_0' < t \leq \frac{1}{2}\frac{p_0}{\sigma_{pl}} t_0' \text{ and } \frac{p_0}{\sigma_{pl}} > 2\\
&\frac{u}{\varepsilon_D\, L} = -m + \sqrt{m^2 + \xi\left\{\frac{p_0}{\sigma_{pl}} - \frac{4}{3}\right\}} && t > \frac{1}{2}\frac{p_0}{\sigma_{pl}} t_0' \text{ and } \frac{p_0}{\sigma_{pl}} > 2
\end{aligned}
\tag{D.7}
$$

where the two dimensionless numbers are the mass ratio m between the front panel and foam bar, and the impact factor ξ

$$m = \frac{m_p}{m_f} \qquad\qquad \xi = \frac{I^2}{m_f\, F_0\, \varepsilon_D\, L}$$

with I being the total impulse exerted on the front panel by the blast as $I = \frac{1}{2}\, p_0\, t_0'\, A$ and F_0 is the blast loading force of $F_0 = p_0\, A$, [Hanssen et al., 2002].

As seen from the solution, if $\sigma_{pl} > p_0$ then no deformation of the foam takes place as the strength of the material is larger than the blast load. If the blast load is marginally larger than the strength of the material $\sigma_{pl} < p_0$, the deformation of the foam reaches its maximum and stops during the blast loading $(t < t_0')$ if

$$1 \leq \frac{p_0}{\sigma_{pl}} \leq 2$$

And finally, if the blast load is a lot larger than the strength of the foam, the deformation of the foam reaches its maximum value at time t_m given by

$$\frac{t_m}{t_0'} = \frac{1}{2}\frac{p_0}{\sigma_{pl}}, \qquad \frac{p_0}{\sigma_{pl}} > 2$$

The duration of the blast load t_0' compared to the time the pressure of σ_{pl} acts on the wall t_m is seen in figure D.4, and the impulse inflicting the reaction wall is $\sigma_{pl}\, A\, t_m = \frac{1}{2}\, p_0\, A\, t_0'$. This shows, that the impulse from the blast loading is exerted by the foam bar on the reaction wall, i.e. conservation of momentum, the force is reduced, but an increase in the duration induces the same impulse.

[1] using mathematical software

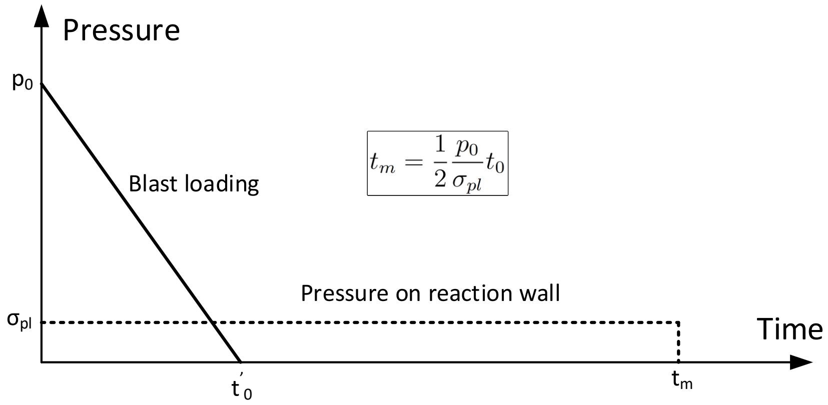

Figure D.4: *[Hanssen et al., 2002]*

Using the lock-strain/densification strain, the maximum deformation in the foam is

$$0 \leq \frac{u}{\varepsilon_D \; L} \leq 1$$

and using eq. D.7 the condition between the two dimensionless parameters m and ξ is

$$0 \leq \xi \leq \frac{1 + 2\,m}{\left[\frac{p_0}{\sigma_{pl}} - \frac{4}{3}\right]}, \qquad \frac{p_0}{\sigma_{pl}} > 2 \tag{D.8}$$

Following this, the minimum length of the foam bar to be able to fully absorb the blast load is

$$L \geq \frac{I^2}{(m_f + 2\,m_p)\,p_0\,A\,\varepsilon_D} \left(\frac{p_0}{\sigma_{pl}} - \frac{4}{3}\right), \qquad \frac{p_0}{\sigma_{pl}} > 2 \tag{D.9}$$

In cases where these conditions are not met, the foam bar becomes fully compacted before the blast has been damped, and the blast load is transferred undamped into the reaction wall increasing the stress from σ_{pl} to the value of the blast loading.

The necessary model parameters such as p_0 and t_0 can be estimated from the software ConWep, along with material tests to determine the strength σ_{pl} of the foam.

E | Basic hydrocode

The following appendix is an edited version of the "Numerical simulations" chapter in [Barrett et al., 2016]. Here included for completeness and reference.

Numerical simulations for impact and blast loads are usually conducted in hydrocodes. Hydrocodes are numeric programs specialised in solving impact problems. According to [Zukas, 2004] the name hydrocode stems from the earliest codes where hydrodynamic behaviour was assumed for high strain rate impact problems. Most hydrocodes solve transient problems by an explicit formulation as this is, usually, superior for small time steps. For a brief summary of the solving process see appendix F.

The commercial hydrocodes ANSYS Autodyn and ANSYS Explicit Dynamics are used to simulate the blast load effects. As the names suggest both programmes are part of ANSYS simulation suite, version 17.2. In fact, Explicit Dynamics is in reality only a pre- and post-processor, as it uses the Autodyn solver. Autodyn gives more possibilities and control to the user, while Explicit Dynamics is easier to use and gives the possibility of parametrising inputs and outputs. Parametrising is especially useful when conducting multiple similar studies, such as convergence study, and also gives the possibility of using optimisation on a simulation. The modelling methods, material models, etc. are described with regards to Autodyn as these options and possibilities are dependent on the solver. The accessibility through Explicit Dynamics is mentioned when relevant.
Both Autodyn and Explicit Dynamics are used during the project. Both also have access to a library of explicit material models, this is subsequently called the ANSYS material library. It is of course also possible to implement custom materials based on user defined data."

Methods

Autodyn contains multiple methods for solving problems of different characteristics, which can also be combined for highly complex problems. Some of them are:

- Finite element for structural dynamics (Lagrange)
- Finite volume for transient fluid dynamics (Euler)
- Adaptive mesh for structural dynamics with large deformation (ALE)
- Mesh-free particle for large deformation and fragmentation (SPH)

When using Explicit Dynamics only Lagrange and Euler are directly available. Systems can be pre-processed in Explicit Dynamics and then migrated to Autodyn and converted to or have SPH and ALE parts added. Post-processing the results back in Explicit Dynamics has not been found to be possible.

Lagrange

In Lagrange method the mesh follows the material as it deforms, the amound of material in an element is the same before and after deformation. This makes it easy to keep track of material and material flow during the simulation. Contact is also handled more easily as it can be determined as contact between meshes with distinct nodes and element edges. The downside is when large deformations occur the elements can distort and thereby lose accuracy and as the time step is determined from the smallest element length in the system the simulation can begin to use such a small time step that it effectively grinds to a halt. To counter this the method of erosion is often employed, this is different from the physical erosion and is simply the removal of elements that fulfil certain conditions, often related to the size of the time step. When employing erosion it is possible to retain the nodes from eroded elements, as the nodes contain the mass of the element, as well as displacement, velocity and acceleration. It is therefore possible to keep the kinetic energy in the system, the potential energy from stresses is however lost.

Euler

In the Euler method the mesh is fixed and material flows through the mesh from cell to cell. The downsides of Lagrange are therefore omitted as the cells do not distort and large deformations do not affect the time step of the simulation. As material boundaries are not defined by the mesh these, and contact, must be defined and tracked by different means. This adds extra complexity to the simulation and as the mesh is static it needs to be defined for the entire zone that material may move to. Euler is preferable for fluid material, such as air and water, as these materials usually undergo very large distortions. Autodyn contains two Euler solvers, multi-material and flux-corrected-transport. Multi-material can be used for all types of materials, fluids as well as solids, and contacts within the Euler domain. Flux-corrected-transport (FCT) is a shock-capturing scheme useful for discontinues problems and yields more precise results. In the user interface of Autodyn FCT is now called ideal-gas as only materials using an ideal-gas model are allowed. This typically restricts its used to blast waves and explosions.

ALE

Arbitrary Lagrange Euler is, as the name may suggest, a mixture of the Lagrange and the Euler method. It works as a Lagrange simulation, with deforming mesh, which at a set interval of iterations restructures the mesh so that highly skewed elements are avoided. The restructuring is usually conducted on internal nodes so that the boundary of the material is kept. During the restructuring, the deformations and stresses are transferred from former nodes and elements to new nodes and elements. This process is similar to deformation with Euler method, hence the name, and if the restructuring is done at each iteration ALE becomes, more or less, pure Euler. ALE gives the advantages of both Lagrange and Euler at the cost of higher computational demands, more complexity and loss of history of each node.

SPH

Smoothed-Particle Hydrodynamics, also known as mesh less simulation, is a method where the nodes are not connected by elements or cells and is thereby mesh less. By not connecting the nodes by elements the problem of large distortion and infinitesimal time steps are avoided. Break up and fracture of material are also handled more naturally. The SPH method is highly complex and have many tuning parameters. It is the most recent of the mentioned methods and is still under heavy development.

Interactions

Both SPH and ALE are in essence derived from Lagrange formulations and contacts between these three are handled in much the same way. Autodyn contains two types of contact detection, trajectory and proximity based. Trajectory based contact detection track nodes and faces, and activates contact when a node crosses a face during a cycle. Proximity base contact detection encapsulates external nodes and faces in a contact detection zone, and activates contact when a node enters this zone. Trajectory does not affect the size of the time step, but for proximity the time step must not be so large that a node can travel all the way through the detection zone. Proximity based contact require an initial gap between geometry parts. Trajectory based contact is not available for SPH and structured grids.
Lagrange and ALE parts can interact with Euler through an Euler-Lagrange coupling. This is achieved by regarding the Lagrange body as a moving boundary for the Euler domain. This results in stress in the Euler material and reactions forces that are applied to the Lagrange part in a feedback system. It is important for Euler-Lagrange coupling that the Lagrange elements are larger than the Euler cells as leakage of material in the Euler domain otherwise may happen. When using Lagrange shells an effective coupling thickness is employed.

Material models

The model for a material in dynamic simulations is build up of multiple parts. For each part there exist many different models depending on behaviour and application. From simple linear model identical to static behaviour to complex ones taking many factors into account, even lookup tables from extensive lab tests. Different parts can be mixed and matched to fit a specific use or available data. All materials are, as minimum, supplied with an reference density (ρ_0) and an Equation of State. Specific heat (at constant volume, C_v) and thermal conductivity are often specified but not necessarily.

Equation of State

Equation of State (EOS) is the relation between the pressure, or hydrostatic stress, the local density, and the local specific energy. The simplest EOS is Hooke's law, in hydrocode it is often formulated by means of the bulk modulus. The bulk modulus gives a linear relation between hydrostatic stress and change in volume, and does not take temperature into account. Hooke's law is valid for linear elastic materials and yields good results for relatively small volumetric change, around 2%.

$$\sigma_{hyd} = -p = 3\,K\,\epsilon_{hyd} \tag{E.1}$$

In ANSYS Autodyn this EOS is called: Linear EOS.

The aluminium models in ANSYS material library use a linear shock EOS. According to [ANSYS Inc., 2016] this EOS is based on Rankine-Hugoniot equations for the shock jump conditions and relates the pressure to the change in density (change in volume), specific energy and particle velocity. It is formulated in eq. E.2.

$$\begin{aligned} p &= p_H + \Gamma\,\rho(e - e_H) \\ p_H &= \frac{p_0\,C_0^2\,u(1+\mu)}{(1-(S-1)\mu)^2} \\ e_H &= \frac{1}{2}\frac{p_H}{p_0}\left(\frac{\mu}{1+\mu}\right) \\ \mu &= \frac{\rho}{\rho_0} - 1 \end{aligned} \tag{E.2}$$

where p is pressure, e is specific energy, u is particle velocity, ρ is density, C_0 is the bulk sound speed called C_1 in the library, S is the Hugoniot linear slope coefficient called S_1 in the library, and Γ is the Gruneisen coefficient and relates energy and volume to pressure. Both EOS are combined with a shear modulus for deviatoric distortion.

Strength

During large deformation the material often starts to yield and deform plastically. When and how this happens is often termed as strength of the material. One of the most used ones for ductile materials is Johnson-Cook's strength model, see [Johnson and Cook, 1983], which takes strain, strain rate and temperature effects into account, eq. E.3. This makes it highly applicable for transient problems where strain rate hardening and thermal softening can not be ignored. The model contains five constants, A is the yield strength, B is the strain hardening constant, n is the strain hardening exponent, C is the strain rate constant and m is the thermal exponent. ϵ_p is the effective plastic strain, $\dot{\epsilon_p}$ is the effective plastic strain rate, $\dot{\epsilon}_0$ is the reference strain rate, and T is temperature. A, B and n can be determined independently of C and m by testing at strain rate 1 s^{-1} at room temperature, the strain rate term and thermal term thereby equates to one. The remaining terms are typically determined by fitting to data at varying strain rates and temperatures.

$$\begin{aligned} Y &= \left[A + B\epsilon_p^n\right]\left[1 + C\,\ln(\dot{\epsilon_p}^*)\right]\left[1 - T^{*m}\right] \\ \dot{\epsilon_p}^* &= \frac{\dot{\epsilon_p}}{\dot{\epsilon}_0} \\ T^* &= \frac{T - T_{room}}{T_{melt} - T_{room}} \end{aligned} \tag{E.3}$$

The Steinberg-Guinan model is another strength model often used in hydrocode. It is the strength model used for most of the aluminium models in the ANSYS material library. Steinberg-Guinan takes the saturation of strain rate effects, compared to other factors, some materials exhibit at strain rates greater than 10^5 s^{-1}, into account. It also accounts for changing shear modulus due to pressure and temperature. It takes the form of eqs. E.4 and E.5.

$$G = G_0 \left\{ 1 + \left(\frac{G'_P}{G_0} \right) \frac{P}{\eta^{1/3}} + \left(\frac{G'_t}{G_0} \right) (T - 300) \right\} \tag{E.4}$$

$$Y = Y_0 \left\{ 1 + \left(\frac{Y'_P}{Y_0} \right) \frac{P}{\eta^{1/3}} + \left(\frac{G'_t}{G_0} \right) (T - 300) \right\} (1 + \beta\epsilon)^n \tag{E.5}$$

Where Y is the yield strength, G is the shear modulus, G_0 is the shear modulus at 300 kelvin, Y_0 is the yield strength at Hugoniot elastic limit, T is temperature in kelvin, ϵ is effective plastic strain, η is compression ratio, $\eta = V_0/V$, β is the strain hardening constant and n is the strain hardening exponent. Primed parameters subscripted with T and P are the derivatives of the parameter with respect to temperature and pressure respectively, at a reference state with T = 300 K, P = 0 and $\epsilon = 0$.
In ANSYS it has an built-in failure mechanism as the shear modulus and yield strength are set to zero if the temperature exceeds the specified melting temperature.

Failure

At a sufficiently high load, any material will fail. This is especially true in hydrocode where stresses can reach very high magnitudes. Breakup of structures are often an important factor in hydrocode studies. To model this in hydrocode, failure is divided into two parts, failure initiation and post failure response. *Failure initiation;* model when failure occurs in a given element. Several different criteria exist to determine failure initiation; plastic strain, principle stress failure, Johnson-Cook failure and more. *Post failure response;* model a given element's strength characteristics after failure. Two different models exist for post failure response, instantaneous failure and gradual failure. Gradual failure is also called damage. For instantaneous failure the deviatoric stresses are set to zero immediately upon failure and subsequently kept there. The element is additionally only able to support compressive pressure. For gradual failure, the stresses in the element are gradually limited. Failure can also be used as a criterion for element erosion.

F | Hydrocode cycle process

The following appendix describe the cycle process in solving numerical problems using hydrocode.

Hydrocodes makes use of an explicit formulation for solving high speed and/or high strain problems. The explicit formulation is solved by cycling through a series of sub-processes, advancing forward one time step with each cycle. The cycle process described in the following is based on the Lagrange method but the main idea is the same for all methods. The appendix chapter is based on [ANSYS Inc., 2016] and [Zukas, 2004].

Time step

The time step is the step taken in each cycle which advances the simulation. The step can vary for each cycle to ensure stability, and is usually defined by the smallest element size in the mesh

$$\delta t = f \left[\frac{h}{c} \right]_{min} \tag{F.1}$$

where δt is the time step, h is the characteristic height of an element, c is the speed of sound of the material in the element, and f is a stability factor. The stability factor is as default $f = 0{,}6666$ in Autodyn and $f = 0{,}9$ in Explicit Dynamics.

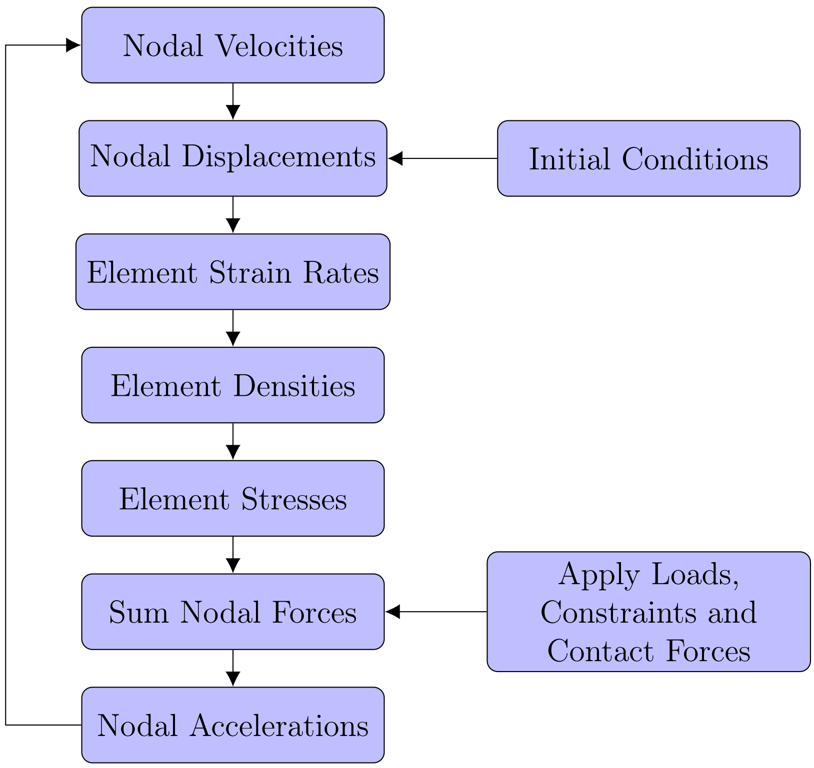

Figure F.1: *The cyclic solve process for hydrocode solvers.*

Figure F.1 illustrates the cyclic process used in hydrocode. The initial conditions are determined during preprocessing, velocities, pre-stress, materials, loads, boundary conditions. At this point time is, usually, set to $t = 0$.

- **Nodal Velocities** are determined explicitly from the accelerations, current velocities and the time step. The central difference method is used for the velocity, thus it is displaced by half a time step.

$$\dot{u}\left(t + \frac{\delta t}{2}\right) = \dot{u}\left(t - \frac{\delta t}{2}\right) + \ddot{u}(t)\delta t \tag{F.2}$$

- **Nodal Displacements** are calculated explicitly based on the velocity, current displacement and time.

$$u(t + \delta t) = u(t) + \dot{u}\left(t + \frac{\delta t}{2}\right)\delta t \tag{F.3}$$

- **Element Strain Rates** are calculated based on the velocity and element formulation. Element strains are based on strain rates and current strains.

$$\dot{\epsilon}(t + \delta t) = \frac{\partial \dot{u}(t + \delta t)}{\partial x_i} \tag{F.4}$$

$$\epsilon(t + \delta t) = \epsilon(t) + \dot{\epsilon}(t + \delta t)\delta t \tag{F.5}$$

- **Element Densities** are determined from the new element volumes determined from the new nodal locations.

- **Element Stresses** are calculated from the elements and the strain rates. These depend on the material model. Elastic stresses based on bulk and shear modulus.

$$\sigma_{Hyd}(t + \delta t) = \sigma_{Hyd}(t) + K\dot{\epsilon_v}(t + \delta t)\delta t \tag{F.6}$$

$$\sigma'_{ij}(t + \delta t) = \sigma'_{ij}(t) + 2G(\dot{\epsilon_{ij}}(t + \delta t) - \delta_{ij}\dot{\epsilon_v}(t + \delta t))\delta t \tag{F.7}$$

- **Summing Nodal Forces** from stresses in the elements by the use of the element formulation. External forces from loads constraints and contacts are added to the nodes.

$$F = \int \sigma \, dV + F_{external} \tag{F.8}$$

- **Nodal Accelerations** are calculated from the nodal forces and masses.

$$\ddot{u}(t + \delta t) = \frac{F}{m} \tag{F.9}$$

- **New Cycle** is then ready, the time is updated, $t = t + \delta t$. A new time step is determined based on the new densities (for the speed of sound) and element sizes. If the end time is reached the simulation is terminated. Result and restart files are written.

G | Additional materials for numeric simulations

The following appendix document the addition of two materials to the ANSYS material library, for use in simulations.

The ANSYS material library contains a wide variety of materials for use in explicit simulations. Two materials used in the simulations are added as these are not found in the library. These are ARMOX 500T armour steel and the Alulight foam material.

The ARMOX 500T material is modelled with the linear equations of state and the Johnson Cook strength model. Data for the material models are obtained from SSAB Oxelösund AB [2007] and Nilsson [2003]. The parameters are shown in table G.1.

Parameter	**Value**	**Unit**
Density	7,85	$\frac{\mathrm{g}}{\mathrm{cm}^3}$
Specific Heat	450	$\frac{\mathrm{J}}{\mathrm{kg\,K}}$
Bulk Modulus	175000	MPa
Shear Modulus	80000	MPa
Initial Yield Stress (A)	1470	MPa
Hardening Constant (B)	702	MPa
Hardening Exponent (n)	0,199	
Strain Rate Constant (C)	0,00549	
Thermal Softening Exponent (m)	0,811	
Melting Temperature (T_{melt})	1800	°C
Reference Strain Rate ($\dot{\epsilon}_0$)	1	s^{-1}

Table G.1: *Material parameters for ARMOX 500T.*

The Alulight material (foam) is also modelled with the Isotropic Elasticity model in ANSYS, which converts to the linear equations of state in Autodyn, and the Crushable Foam strength model. The data for the material models are obtained from the material test described in appendix C. The crushable foam strength model used table data for the stress-strain relation in the plastic domain. This is imputed from a file containing the data shown in figure C.3(a) page 124.

Parameter	**Value**	**Unit**
Density	0,458	$\frac{\mathrm{g}}{\mathrm{cm}^3}$
Bulk Modulus	112	MPa
Shear Modulus	168	MPa
Max Tensile Stress	2	MPa

Table G.2: *Material parameters for Alulight.*

Both material are supplied in the annex as .xml files that can be imported into ANSYS.

H | Design of test setup expansion

The following appendix document the design of an expansion for the test setup in the terminal ballistics laboratory, Fibigerstræde 14, Aalborg University. This expansion permits the use of a ballistic pendulum.

To determine the effectiveness of a material's energy absorbing properties under blast loads, a pendulum structure is often used. The energy taken by the pendulum can be determine from the swing of the pendulum. The swing is reduced by the energy absorbed by the target.
At the start of the project, the test setup is not setup for this type of measurements, even though it is originally designed for this a relocation has striped it of this capability. For that reason an extension is designed and built to facilitate this type of measurements.

Target end test setup

The test setup for the target end is constructed of a number of components.

- Bottom frame
- Top frame (New)
- Frame connection plates (New)
- Bullet catcher
- Hangers
- Hanger rails (New)

At the onset of the project only the bottom frame, the bullet catcher and the hangers exist.
Both top and bottom frame are constructed from 100x100x5 square steel tubes. The two frames are bolted together with the use of the frame connection plates. The top frame are built with a series of holes used for mounting the hanger rails at different heights. The frame connection plates are 20 mm thick steel plates with six threaded holes, they connect the two frames at each corner. The bullet catcher is a heavy steel pipe with a removable back lid of aluminium and two "ears" at the front for mounting impact dampers. The bullet catcher is at the onset of the project fixed to the bottom frame despite being designed to function as a pendulum. The hangers are constructed from square tube, c-bar and flat-bar, they are design to work with the bullet catcher as pendulum arms and are equipped with copper bearings. The hanger rails are made from 40x15 flat-iron and contains holes along the length for mounting the hangers. The complete assembly is shown on figure H.1, both CAD- and work-drawings are found in the annex.

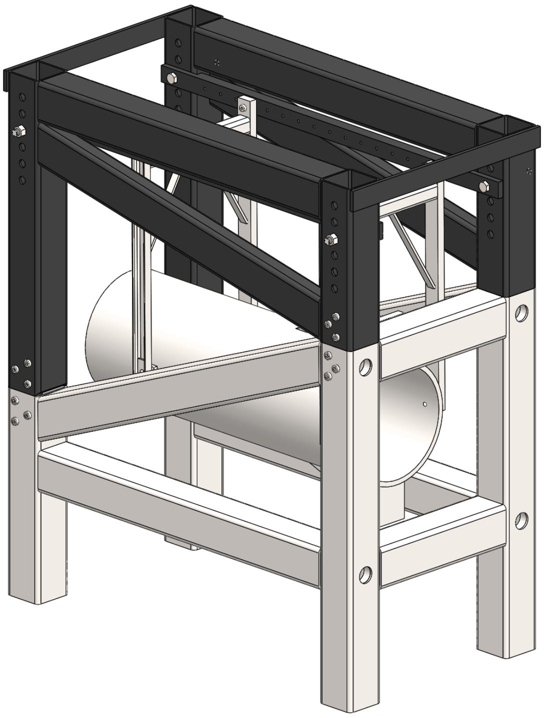

Figure H.1: *The new target end test setup. New additions are coloured dark grey.*

I Strain gauge measurements

The following appendix describes the basic strain gauge theory needed for conducting strain gauge measurements, along with necessary calibrations and sampling rates for problem free data collection.

The method of obtaining data from the panel during the blast loading is by measuring and record the strain response in different locations on the panel. A basic understanding on the use of strain gauges is therefore necessary, and described in the following section.

Strain gauges utilise that the electrical resistance of wires is directly reliant on the length of this wire, or in the cases of strain gauges, the change in resistance in the wire is proportional to the change in length pr. unit length, strain, of the wire. For the strain gauge applies

$$\varepsilon = \frac{\Delta L}{L} \tag{I.1}$$

where L is the original gauge length and ΔL is the elongation of the wire.

As the cross-sectional area of the wire is very small, the resistance in the wire is very sensitive to straining parallel to the ordered wire direction, shown in figure I.1. The strain gauge yields an average measure of strain, which is interpreted as the strain of the point in the center of the strain gauge.

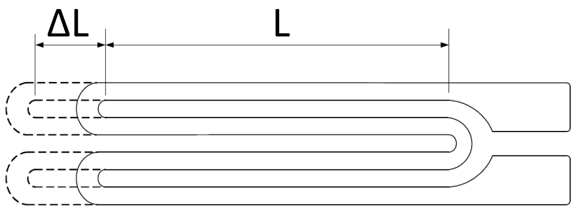

Figure I.1: *From [Christensen and Olesen, 2007].*

The relation between the measured strain and the change in resistance is

$$\frac{\Delta R}{R} = k_{SG}\,\varepsilon'_a \tag{I.2}$$

where $\Delta R/R$ is the relative change in resistance, ΔR is the change in resistance, R is the initial resistance, k_{SG} is the strain gauge factor and ε' is the measured strain.

Due to this strain sensitivity, a strain gauge also detects the transverse strain which is inconvenient as the two strain contributions, axial and transverse, is not measured separately. The transverse sensitivity, k_t, of the strain gauge has to be accounted for.
A very low transverse sensitivity for strain gauges is desired, as the measured strain ε' and the actual strain ε is taken as equal and the relation between resistance and strain is, using eq. I.2

$$\varepsilon_a = \frac{\Delta R}{R}\frac{1}{k_{SG}} \tag{I.3}$$

For cases where the transverse sensitivity is significant, one has to account for this using the strain gauge equation

$$\varepsilon_a = \frac{\Delta R}{R}\,\frac{1}{k_{SG}}\left(\frac{1 - k_t\,\nu_0}{1 + k_t\,\frac{\varepsilon_t}{\varepsilon_a}}\right) = \varepsilon_a'\left(\frac{1 - k_t\,\nu_0}{1 + k_t\,\frac{\varepsilon_t}{\varepsilon_a}}\right) \tag{I.4}$$

where ε_a and ε_t are the axial and transverse strain and $\nu_0 = 0{,}285$ is the Poisson's ratio of the strain gauge calibration material, [Hoffmann, 1989].

As the strain gauges are so strain sensitive, thermal effects of the material may be an issue when conducting measurements. The issue can be reduced by utilising strain gauges that fit the material they are mounted on, i.e. similar thermal expansion coefficient.

The Wheatstone Bridge

A Wheatstone bridge is an electrical circuit used in measuring electrical resistance extremely accurate. It is therefore suitable for use in combination with strain gauges. A schematic of the Wheatstone bridge is shown in figure I.2.

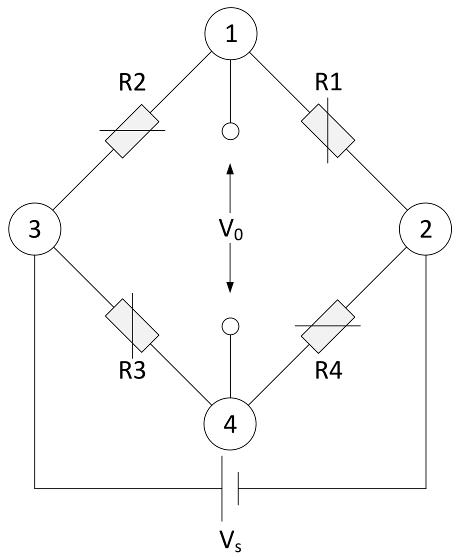

Figure I.2: *A schematic of the Wheatstone Bridge. A full bridge is shown if you consider all the resistors are connected as strain gauges. Other configurations are a half- or quarter bridge utilising two or one leg for strain gauge(s) respectively.*

The circuit is made up of four resistors of two serial connections in parallel. A supply voltage of V_s is applied and the output voltage of V_0 depends on the equivalent resistance of the four resistors as the following ratio shows, [Hoffmann, 1989]

$$\frac{V_0}{V_s} = \frac{R_1\,R_3 - R_2\,R_4}{(R_1 + R_2)(R_3 + R_4)} \tag{I.5}$$

Equation I.5 is nonlinear, and often the following linear approximation is used

$$\frac{V_0}{V_s} \approx \frac{1}{4}\left(\frac{\Delta R_1}{R_1} - \frac{\Delta R_2}{R_2} + \frac{\Delta R_3}{R_3} - \frac{\Delta R_4}{R_4}\right) \tag{I.6}$$

This approximation is usually sufficient.

A complete measurement system generally consists of a strain gauge amplifier in which the Wheatstone bridge is include. This amplifier processes the signal and supply the bridge and thereby gauges with the necessary voltage. The strain gauges act as variable resistors in the chosen bridge configuration, figure I.2. The reading from the amplifier is

$$\varepsilon_i = \frac{4}{k_{bridge}} \frac{V_0}{V_s} \tag{I.7}$$

where k_{bridge} is the bridge factor/amplification factor.

This can be rewritten in terms of relative resistance change using eq. I.6 and eq. I.2 and substituting into eq. I.7

$$\begin{aligned} \varepsilon_i &= \frac{1}{k_{bridge}} \left(\frac{\Delta R_1}{R_1} - \frac{\Delta R_2}{R_2} + \frac{\Delta R_3}{R_3} - \frac{\Delta R_4}{R_4} \right) && \text{(I.8)} \\ &= \frac{1}{k_{bridge}} \left(k_{SG1}\, \varepsilon'_1 - k_{SG2}\, \varepsilon'_2 + k_{SG3}\, \varepsilon'_3 - k_{SG4}\, \varepsilon'_4 \right) && \text{(I.9)} \end{aligned}$$

which is the equation for the full bridge configuration.

Influence of long cables

As the strain gauges are to be mounted on an armour panel for a live-blast test, a safety zone for both equipment and personnel is to be expected. A blast test of a former project group, [Christensen and Olesen, 2007], described a safety distance of 50 m when the equipment was suspended in rubber bands, and in the present case at least 18 m is necessary as determined in chapter 9. This requires the use of very long cables compared to laboratory experiments, and the effect of this on calibration and measurement errors has to be considered.

The effect of long cables, and how to counteract it is investigated in [Christensen and Olesen, 2007]. The test of long cables (50 m) is compared against a reference test using cables of 1,5 m on a beam in bending.
The investigation found, that the use of a quarter bridge and a long cable is infeasible, as calibration of the strain gauge could not be achieved due to the resistance in the long cable resulting in an unbalance, which the amplifier is unable to correct, in the Wheatstone circuit. Using just a quarter bridge configuration, it is impossible to cancel the resistance in the cable.
A half bridge configuration was also investigated. Using this configuration it is possible to cancel the resistance in the cable. This is achieved by mounting one of the strain gauges on an unloaded metal piece, i.e. a dummy strain gauge. By subtracting the two measurements from each other, one effectively removes the strain-error due to the resistance in the cables. Furthermore, by mounting the dummy strain gauges on a similar material and placing them in the same temperature, the temperature effect is likewise cancelled out. This is also seen by eq. I.8 considering only R_1 and R_2. [Christensen and Olesen, 2007] determined, that there still exists an error of approximately 6% from the reference measurement.

This error measurement can be eliminated by use of a correction formula, [Hoffmann, 1989]. The correction formula require a measurement of the resistance in the feeder cable, the return cable and the strain gauge. For the half bridge configuration (fig. I.3), the correction formula is [Hoffmann, 1989]

$$\varepsilon_1 - \varepsilon_2 = \varepsilon_i \frac{R_{C1,feed} + R_{SG1} + R_{C1,return} + R_{C2,feed} + R_{SG2} + R_{C2,return}}{R_{SG1} + R_{SG2}} \tag{I.10}$$

where $R_{CX,feed}$ and $R_{CX,return}$ are the cable out to (feeding) the strain gauge and returning from, respectively, and R_{SGX} is the resistance of the chosen strain gauge, e.g. 120 Ω. The validity of the correction formula was tested in [Christensen and Olesen, 2007].

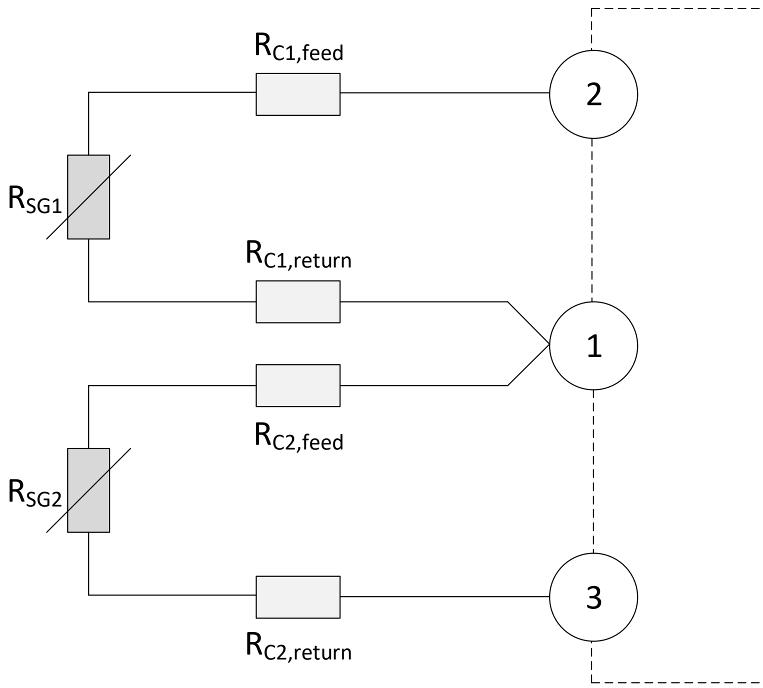

Figure I.3: *A half bridge configuration, and definition of parameters in eq. I.10. $R_{CX,feed}$ etc. represent the resistance in the long cables. [Hoffmann, 1989].*

Necessary sampling rate

The loading of the armour panel happens is a very short duration. The analyses show, that maximum deformation is achieved in approximately t_m = 1,3 ms by the numerical methods, and t_m = 0,67 ms for the analytical methods. The eigenperiod is also determined analytically for a linear SDOF system to T = 2,69 ms. As a precaution the sampling time is increased to 3 ms to not miss any interesting parts of the blast test. A high sampling rate is desired to create enough data points for detecting what happens during the loading, and compare results.

The available strain gauge amplifier, Spider8 from HBM [2017], has a maximum sampling rate of 9600 Hz, [HBM-S8, 2017]. With the maximum sampling rate, it is possible to record 28 data points in the 3 ms time range. As four strain gauges are used, the sampling is furthermore conducted on four channels. This limits the duration of the measurement period due to restrictions governed by the laptop, this has to be considered. The laptop can be set to run a loop, and first start recording the data after a set time, or at a set load, i.e. a pretrigger. In [Christensen and Olesen, 2007] with sampling on the same number of channels, a loop of 20 ms was possible.

Preparing the armour panel with strain gauges

The location of the strain gauges on the armour panel, the type of strain gauge used and the bridge configuration is described in the following.

Different type of strain gauges are available, and these are shown in figure I.4. The strain gauges can be used for;

- **Single gauge.** Used to measure the axial strain in one point in the direction of the gauge orientation.
- **Double gauge.** Used to measure biaxial strain in one point, in the individual direction of each gauge perpendicular to one another.
- **Rosette.** Used to measure all in-plane strains in a point, as shear strain is measured by the gauge in the 45° direction.
- **Chain gauge.** Used to measure strain and strain gradient in the length of the chain.

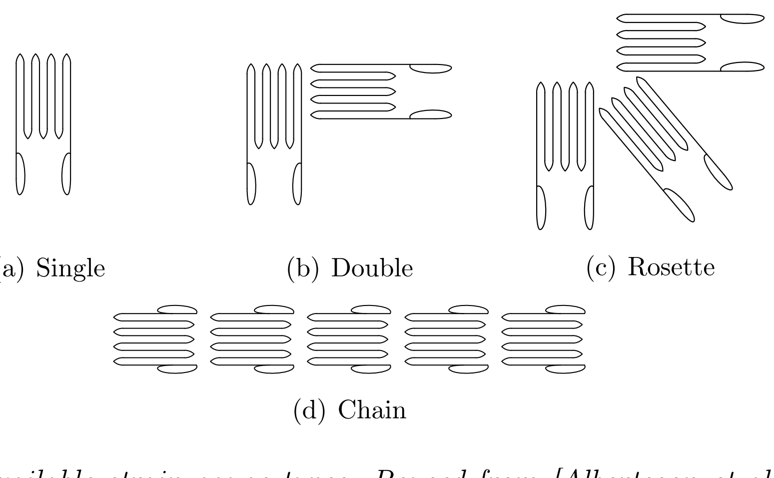

(a) Single (b) Double (c) Rosette (d) Chain

Figure I.4: *Available strain gauge types. Reused from [Albertsson et al., 2015].*

The strain gauges can also be combined, for detecting if a strain in the structure is from a tension/compression or a bending load. This is obtained by placing two single gauges opposite each other in a symmetrical cross-section about the bending axis. In case the rosette is used, one has to adjust the measured strains with the rotation equation for determining the transverse effect,

$$\varepsilon'(\alpha) = \varepsilon'_{xx} \cos^2(\alpha) + \varepsilon'_{yy} \sin^2(\alpha) + 2\,\varepsilon'_{xy} \cos(\alpha) \sin(\alpha) \tag{I.11}$$

and α is the angle of orientation on the strain gauge. Hereafter, the strain gauge equation, eq. I.4, is applied.

Placement and purpose of strain gauges

The strain gauges are glued onto the backside of the armour panel, i.e. the ARMOX backing plate, for immediate protection against the blast. They measure the elastic response during loading. An equal amount of dummy strain gauges are glued onto an unloaded ARMOX structure and placed in the same environment for use as cable and temperature calibration as discussed previously.

The strain gauges are strategically placed to determine the elastic bulge developing on the backside of the armour panel as the blast load impinges the target. Furthermore, a strain gauge is used for determining the residual load transferred to the fixture, i.e. the chassis of the vehicle.
It is only possible to place the strain gauges on the backside to protect them against the blast wave. It is thereby only possible to measure the transverse strain in the panel, and by this determine whether the deformation of the test, analytical and simulation are consistent. Strain gauge 1 and 2 are checking for double symmetry and should measure the same strain. Strain gauge no. 2 is placed directly in front of no. 3 for measuring the strain gradient to be used in determining the shape of the bulge. No. 4 is for determining the residual load transferred to the fixation structure.

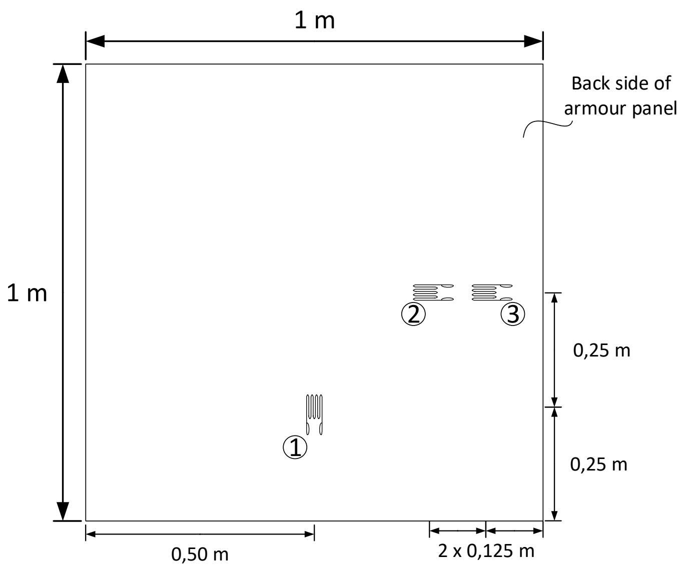

(a) Location of the strain gauges on the back side of the armour panel.

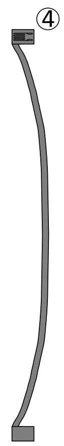

(b) Backplate deformation from simulation.

Figure I.5

In cooperation with

COMPOSHIELD